Chair of Physical Chemistry

Master Thesis

# Sodium ion storage in metal oxide electrodes for rechargeable sodium ion batteries

Lukas Szabados, BSc.

September 2020

# In cooperation

# with


# Department of Physical Chemistry

# University of Innsbruck

Advisors:
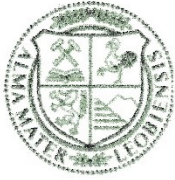
Assoz.Prof. DI Dr.mont. Edith Bucher

**Chair of Physical Chemistry, Montanuniversitaet Leoben**

Univ.-Prof. Dipl.-Chem. Dr. Julia Kunze-Liebhäuser
DI Dr. Engelbert Portenkirchner

**Department of Physical Chemistry, University of Innsbruck**

## EIDESSTATTLICHE ERKLÄRUNG

Ich erkläre an Eides statt, dass ich diese Arbeit selbständig verfasst, andere als die angegebenen Quellen und Hilfsmittel nicht benutzt, und mich auch sonst keiner unerlaubten Hilfsmittel bedient habe.

Ich erkläre, dass ich die Richtlinien des Senats der Montanuniversität Leoben zu "Gute wissenschaftliche Praxis" gelesen, verstanden und befolgt habe.

Weiters erkläre ich, dass die elektronische und gedruckte Version der eingereichten wissenschaftlichen Abschlussarbeit formal und inhaltlich identisch sind.

Datum  18.08.2020

Unterschrift Verfasser/in
Lukas Martin Alexander, Szabados

# Acknowledgments

# Abstract

Energy storage will become more important in the future, regarding the growing sector of electromobility and the increasing share of renewable energy from photovoltaics and wind in the electric grid. State of the art lithium-ion batteries (LIB) will not be able to meet the future demand for energy storage in the long term due to limited resources. Other technologies, such as sodium-ion batteries (SIB) can help to increase the diversification and replace LIB in certain areas, for example in the stationary energy storage.

In this thesis, three different electrode materials, titanium(IV)-oxide in the anatase and amorphous phase and molybdenum(IV)-oxide, are investigated for their suitability in SIB.

The synthesis and the corresponding material characterisation form the first part of this thesis. The titanium(IV)-oxide electrodes are synthesised by electrochemical oxidation and, for the anatase phase, by a phase transition upon thermal annealing in a tube furnace. The molybdenum(IV)-oxide electrode is prepared by physical vapour deposition (PVD) of molybdenum in an oxygen/argon gas mixture with a ratio of 1/100 on a copper substrate. The phase purity of the electrodes is subsequently characterized by Raman and X-ray photoelectron spectroscopy (XPS).

The electrodes are further characterized electrochemically in a SIB half-cell setup by potential dependent impedance spectroscopy, cyclovoltammetry (CV) and galvanostatic cycling with potential limitation (GCPL).

Finally, post mortem analysis using XPS and scanning electron microscopy (SEM) are employed to investigate the composition and morphology of the surface films formed during battery half-cell cycling.

The characterisation of the formed surface films adds important insights in the observed "self-improving" effect of oxide-based electrode materials in SIB. This "self-improving" characteristics are found to significantly influence the performance of the electrodes during long-term GCPL measurements in a Na containing electrolyte and are hence relevant to transition metal oxides, in general.

# Kurzfassung

Die Speicherung von Energie wird in Zukunft, hinsichtlich der wachsenden E-Mobilität und des steigenden Anteils von alternativer Energie aus Photovoltaik und Wind, immer mehr an Bedeutung gewinnen. Die Technologie der Lithium-Ionen-Batterien (LIB) wird diesen steigenden Bedarf an Energiespeichern auf Grund von begrenzten Ressourcen langfristig nicht vollständig decken können. Andere Technologien, wie Natrium-Ionen-Batterien (SIB) können dazu beitragen, die Diversifikation zu erhöhen und LIB in gewissen Bereichen, zum Beispiel auf dem Gebiet der stationären Speicher, zu ersetzten.

In dieser Arbeit werden drei verschiedene Elektrodenmaterialien auf ihre Eignung für den Einsatz in SIB getestet. Titan(IV)-oxid, in der Anatas Phase und im amorphen Zustand, sowie Molybdän(IV)-oxid. Zu Beginn findet die Synthese und die dazugehörige Materialcharakterisierung statt. Die Titan(IV)-oxid Elektroden werden mittels elektrochemischer Oxidation und zusätzlich für die Anatas Phase mittels anschließender, thermischer Phasenumwandlung im Röhrenofen hergestellt. Die Molybdän(IV)-oxid Elektroden werden durch Bedampfen mittels des Physical-vapour-deposition Verfahrens (PVD) hergestellt. Die anschließende Charakterisierung mittels Raman und Röntgenphotoelektronen-spektroskopie (XPS) stellt die Phasenreinheit der Proben sicher.

Die darauffolgende elektrochemische Charakterisierung in einer Batterie-Halbzelle umfasst potentialabhängige Impedanzspektroskopie, Cyclovoltammetrie (CV) und galvanostatisches Zyklieren mit Potentiallimitierung (GCPL).

Abschließend werden die zyklierten Elektroden durch eine "Post mortem" Analyse mittels XPS und Rasterelektronenmikroskop (SEM) untersucht. Dadurch werden Informationen über die Zusammensetzung und Morphologie der bei der elektrochemischen Charakterisierung entstehenden Oberflächenfilme gewonnen.

Diese Oberflächenfilme sind ein wichtiger Bestandteil im Verständnis eines beobachteten „Self-Improving"-Effektes in Na haltigen Batterieelektrolyten. Dieser „Self-Improving"-Effekt steigert die spezifische Speicherkapazität der untersuchten Elektroden bei GCPL Langzeitmessungen deutlich und ist dadurch, für verschiedene Metalloxid Elektroden, von allgemeinem Interesse.

# Contents

# 1. Introduction

## 1.1. Motivation

One of the main issues to moderate global warming in the future will be the long-term and short-term storage of energy. The reasons are manifold, one is the increasing energy generation by alternative energy sources such as wind and solar, which are not constantly accessible and often available at the wrong time.[1] Another reason is the continuously growing market of battery-operated devices and means of mobility.[2] A long-term storage approach could be the power to gas technology, which aims at transforming large amounts of surplus energy into well storable gases like methane.[3]

For short-term energy storage, another concept has already prevailed, the rechargeable battery technology. Conventional systems like lithium-ion batteries (LIB) or lead-acid batteries are not long-term solutions in all the different fields of applications. Especially the environmentally harmful mining and the limited availability of lithium drive efforts into alternative technologies. This is also the case with the equally needed rare, expensive and toxic cobalt for the widely used $LiCoO_2$ cathode material used in commercial LIB due to its high energy density.[4,5]

The sodium ion battery (SIB) could represent a technology that might replace the LIB in certain areas, for example in stationary storage facilities from home scale to large-scale. This is owed to the lower energy density and the associated greater dimensioning of SIB for the same power compared with LIB. The almost unlimited availability in combination with a lower environmental impact during mining and the hope that production will eventually be cheaper than that of LIB has increased the interest of the research community in recent years.[4]

## 1.2. Aims of this work

The main goal of this thesis is the electrochemical characterisation of three different electrode materials, being titanium dioxide anatase ($TiO_{2-x}$-A), titanium dioxide rutile ($TiO_{2-x}$-R), amorphous titanium oxide ($TiO_2$-M) and molybdenum dioxide ($MoO_{2+x}$) for their future use in SIBs.

To meet these aims different characterisation methods including scanning electrode microscopy (SEM) and X-ray photoelectron spectroscopy (XPS) were carried out. After the cells were assembled, electrochemical tests were performed. Finally, post mortem analysis was performed in order to

characterize the chemical and morphological changes following a potential self-improving effect for all electrodes, using XPS and SEM.

# 2. Theoretical Background

This chapter starts with a short comparison of lithium and sodium followed by an introduction of the basic characteristics of the three electrode materials investigated in this thesis. Subsequently, a description of the fundamentals of the various synthesis and characterisation techniques is given, starting with Raman spectroscopy and physical vapour deposition (PVD) followed by XPS and X-ray diffraction (XRD). Finally, the methods of the electrochemical characterisation are described. In addition to cyclic voltammetry (CV) and galvanostatic cycling with potential limitation (GCPL), special attention is paid to the potentio electrochemical impedance spectroscopy (PEIS).

## 2.1. Lithium (Li) vs. Sodium (Na)

Rechargeable batteries are becoming increasingly important in more and more areas including mobility, portable devices up to temporary storage of surplus alternative energy.[4,6] In the last decades, several battery types were invented and are still used today in different applications. One of the oldest is the lead acid battery mainly used as starting battery in cars. Even though it has a low energy efficiency and a limited energy density of about 30 to 40 Wh kg$^{-1}$, it has some advantages, like cost efficiency and robustness.[4]

There are many other types, like the Ni-Cd battery with a cell voltage of 1,2 V and an energy density about 60 Wh kg$^{-1}$ or the NiMH with an energy density of about 100 Wh kg$^{-1}$, respectively.[4] The most important and the most frequently used type with an energy density of around 250 Wh kg$^{-1}$ is still the LIB. The following chemical reactions are used to describe the energy storage in LIBs.[4]

Reaction at the negative electrode:

$$LiC_6(s) + n(solv) \rightleftharpoons Li^+(solv)_n + 6C(s) + e^- \qquad (2.1.1)$$
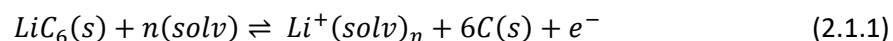
Reaction at the positive electrode:

$$2\,Li_{0.5}CoO_2(s) + Li^+(solv)_n + e^- \rightarrow 2\,LiCoO_2(s) + n\,solv \qquad (2.1.2)$$
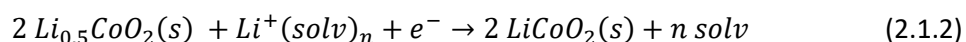
The major problem in the upcoming decades will be the enormously growing demand for electrochemical energy storage. Due to the environmental harmful extraction of lithium and other components like cobalt, the also environmentally harmful disposal currently practised in many countries and the question whether the lithium and cobalt reserves are sufficient to cover the future demand, other storage solutions have to be enhanced to become more independent.[4,5]
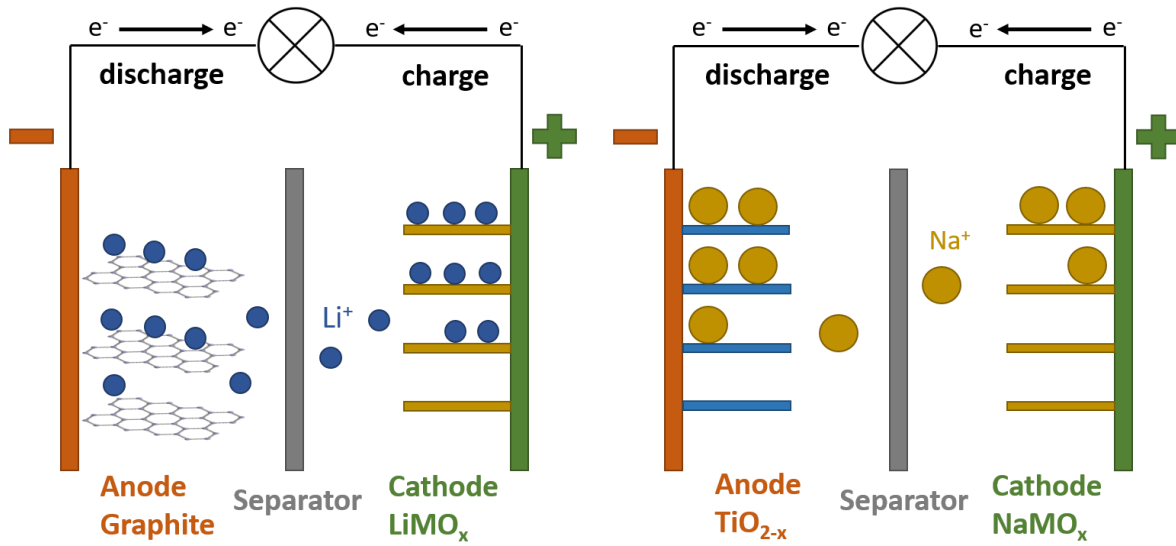


Figure 1.: Schematic visualisation of the working principle of a) lithium insertion/de-insertion of a common LIB with a graphite anode[7] in red and a LiMOx cathode in green, and b) sodium insertion/de-insertion of a SIB with a TiO2-x anode being one of the investigated materials in this work and a NaMOx cathode. For both batteries a separator (grey) is used, which ensures the ion transport with simultaneous isolation for electrons.

The fundamental working principle of LIB and SIB, shown in Figure 1 is quite similar, but the transition from LIB to SIB is not as trivial as one might suppose. One problem is that graphite, which is, by now used as anode in all LIB, can only be used as additive with less than 35 mAh g$^{-1}$ in SIB, since graphite does not intercalate sodium ions reversibly.[8,9] A reason for that is the higher radius of Na (r = 1.02 Å) compared to Li (r= 0.59 Å).[4]

This leads to the fact that the research focus in the field of SIB is on finding new, high capacity anode materials. TiO$_2$ could represent such an auspicious anode material for SIB. In the following equation a possible form of the sodiation reaction is shown:[8]

$$TiO_2 + x(Na^+ + e^-) \rightarrow Na_xTiO_2 \tag{2.1.3}$$
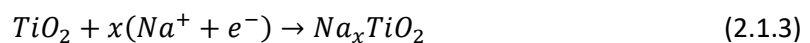
The less negative standard electrode potential against standard hydrogen electrode (E vs. N.H.E.) of sodium, which amounts to -2.71 V compared to the -3.05 V of lithium, also contributes to the fact that the basic conditions of SIB with regards to the required characteristics like power density, energy density and so on, are not as good as for the LIB .[4,10]

Table 1 summarizes the main characteristics of lithium and sodium.

Table 1.: Characteristics of sodium vs. lithium taken and adapted from reference [10].

| Category | Unit | lithium | sodium |
|---|---|---|---|
| Atomic weight | [g mol$^{-1}$] | 6.9 | 23 |
| Radius | [Å] | 0.59[4] | 1.02[4] |
| E° vs. N.H.E | [V] | -3.05[4] | -2.71[4] |
| Capacity (metal) | [mAh g$^{-1}$] | 3829 | 1165 |
| Cost (carbonates) | [$ ton$^{-1}$] | 5000 | 150 |
| Coordination preference | [-] | Octahedral and tetrahedral | Octahedral and prismatic |

## 2.2. Electrode materials

The basic properties and the most important characteristics of the different electrode materials investigated are briefly described in this chapter.

## 2.2.1. Molybdenum dioxide (MoO$_{2+x}$)

Molybdenum (Mo) occurs in oxidation states from +2 to +6, with the hexavalent $MoO_3$ and the tetravalent $MoO_2$ as the two main modifications. In this work, it is intended to synthesize $MoO_2$ due to the presence of delocalized electrons in the valence band, which enable metal-like electronic conductivity. $MoO_2$ has monoclinic structure with the lattice parameters a = 5.6109 Å, b = 4.8562 Å and c = 5.6285 Å.[11,12]

The second, orthorhombic structured $MoO_3$, with the lattice parameters a = 3.9628 Å, b = 13.855 Å and c = 3.6964 Å, also shows potential for use in SIB as for example Zhu et al. show in their investigations, but occurs in this work as an unintentional phase.[13,14]

Nevertheless, a two-phase mixture of the aforementioned oxides occurs in all our samples, because $MoO_2$ immediately oxidizes in air to $MoO_3$, which cannot be avoided in our synthesis setup.[15] Therefore, from now on the term $MoO_{2+x}$ will be used in this context.

Figure 2 shows the phase diagram of molybdenum in dependence of the oxygen partial pressure and temperatures.
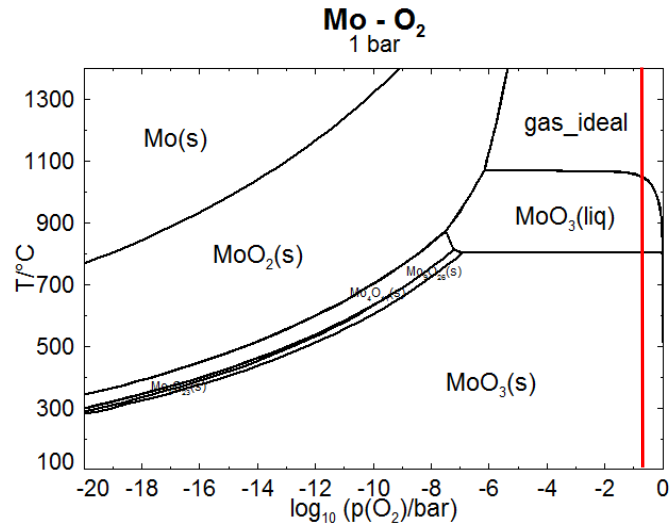


Figure 2.: Phase diagram of the system molybdenum-oxygen in dependence of oxygen partial pressure and temperatures taken from reference [16]. The red line indicates which phases can be achieved in ambient air.

$MoO_2$ is also interesting for rechargeable lithium ion battery anodes and potentially for solid oxide fuel cells as anode material, because of its metal-like electronic conductivity with 88 $\mu S$ $cm^{-1}$.[12,17]

## 2.2.2. Titanium dioxide

**Anatase ($TiO_{2-x}$)**

The second anode material investigated in this thesis is $TiO_2$, more precisely the modification anatase with its lattice parameters a = 3.784 Å and c = 9.515 Å. The crystal structure can be seen in Figure 3a.[18-20] Due to our temperature treatment described in chapter 3.2, the resulting anatase is oxygen deficient and is therefore termed $TiO_{2-x}$.

a)     b)
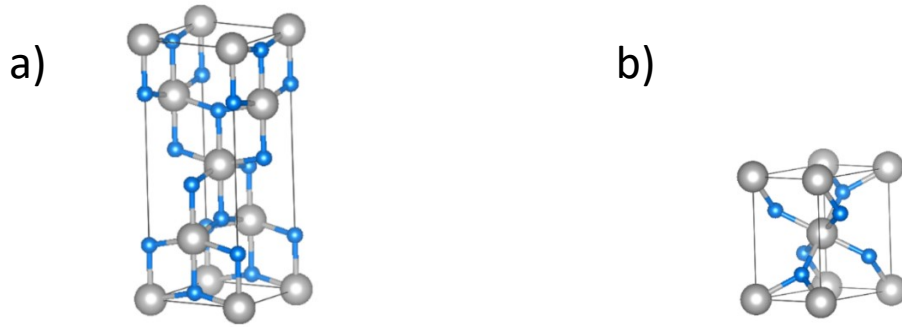
Figure 3.: Ball and stick model of the unit cells of $TiO_{2-x}$ a) anatase[19] and b) rutile[21] plotted with VESTA. Titanium atoms are grey and oxygen atoms are blue.

In Figure 3 also the unit cell of the $TiO_{2-x}$ modification rutile is depicted, which is, beside the anatase and the brookite phase, one of the three main phases of $TiO_{2-x}$.[18] The rutile phase was synthesised additionally to the anatase phase, which is described in chapter 10.3.

**Amorphous ($TiO_2$)**

The next anode material used for assembly of test cells is amorphous $TiO_{2-x}$. Since the amorphous phase is thermodynamically metastable, it is, in this thesis, used for the synthesis of the anatase and the rutile phase. Additionally, it is also investigated with regard to its electrochemical properties.

The atomic arrangement of amorphous $TiO_2$ can be seen as an order of short, stacked chains of edges and vertex chains of titanium and oxygen. It is widely used as component for photoelectrochemical applications due to its good adsorption ability to photosensitizers.[22,23]

## 2.3.  Sodium storage

One factor, which can affect the performance of the cell, is the surface film formation starting with the initial charge/discharge cycle. The cause of this formation is the instability of solvents and salts in the electrolyte, which can influence for example the accessible capacity or the rate capability.[24] In order to better understand the Na storage processes in the cell, it is necessary to investigate both, the storage mechanism of Na inside the oxide layer and the surface film, respectively.

**Titanium dioxide (TiO$_{2-x}$)**

The actual mechanism of the Na ion storage in the TiO$_{2-x}$ is barley investigated, nevertheless there are some studies.

Liming Wu et al. reported that the storage mechanism in TiO$_2$ nanoparticles can be separated in different parts.[9] At potentials higher than 1.0 V, only electrolyte decomposition and capacitive processes take place. Between 1.0 V and 0.3 V, the structure of the TiO$_2$ begins to change to the amorphous phase and accordingly the lattice is distorted. Upon this distortion some sodium ions are inserted into the lattice and TiO$_2$ is reduced to metallic titanium and oxygen between 0.3 V and 0.1 V. Finally, a surface film including sodium titanate, metallic titanium and sodium superoxide is formed containing a sodium content per formula unit of TiO$_2$ of about 0.25 Na.[9]

Also, Wei Li et al. investigated the storage mechanism of Na ions in TiO$_2$.[25] They describe, that the sodium insertion cause a conversion of the anatase structure accompanied by a long-range order loss. This is due to the strong cationic blending between the titanium and sodium slabs. After the de-intercalation, the structure can no longer be considered to assume a layered structure, as a transition to a disordered network with structures similar to anatase takes place.[25]

Portenkirchner et al. investigated amorphous TiO$_2$ nanotubes (NTs), oxygen deficient anatase TiO$_{2-x}$ NTs and carbon coated anatase TiO$_{2-x}$-C NTs  and  found out, that a reversible surface film is formed on the electrode during sodiation/desodiation battery half-cell cycling.[8,26] This surface film leads to a significant increase of the specific capacity during long-term GCPL measurements. It is assumed, that the storage of the Na takes place mainly in this surface film. The presumed procedure of this mechanism is shown in Figure 4.[26]
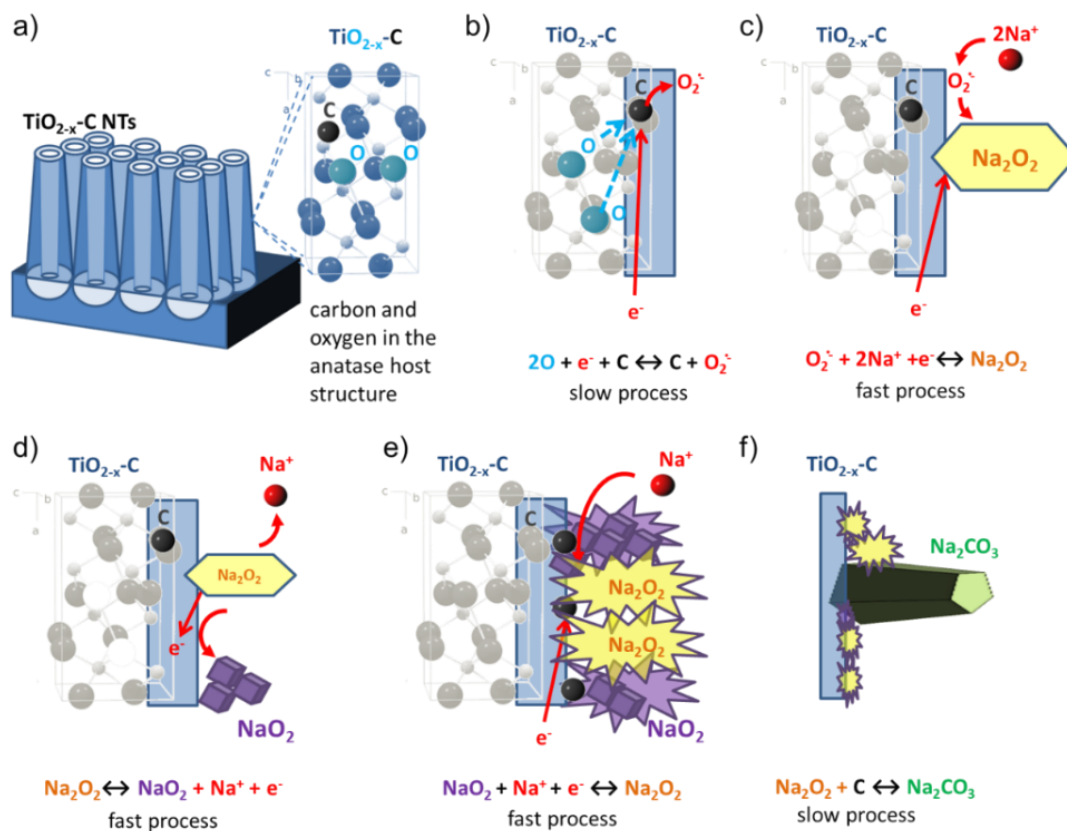
Figure 4.: Proposed mechanism of the Na storage in the surface film taken from reference [26].

The formation of the surface film starts with the reduction of oxygen (O) to oxygen radicals ($O_2^-$) characterized by a slow oxygen diffusion through the anatase lattice due to the strong binding of the oxygen in the anatase lattice. The oxygen radicals on the surface of the electrode subsequently form sodium peroxide ($Na_2O_2$) together with the $Na^+$ cations from the electrolyte. Upon desodiation, the $Na_2O_2$ is reversibly dissolved or transformed into sodium superoxide ($NaO_2$). As soon as sufficient $NaO_2$ is available, further Na ion storage occurs by conversion into $Na_2O_2$, consequently, leading to the formation of a proliferating film. Finally, energetically favourable sodium carbonate ($Na_2CO_3$) is formed from the metastable $Na_2O_2$ which supposedly is the final form of surface deposits when carbonate based electrolytes are used.[26]

**Molybdenum dioxide (MoO$_{2+x}$)**

The Na ion storage in MoO$_2$ electrodes is even less investigated compared to TiO$_2$. Xu Zhao et al. suggest, that the mechanism resembles the Li ion storage mechanism in MoO$_2$[27] and can be described with the following equations:[28]

$$xNa^+ + xe^- + MoO_2 \rightarrow Na_xMoO_2 \ (intercalation) \tag{2.3.1}$$

$$Na_xMoO_2 \rightarrow xNa^+ + xe^- + MoO_2 \ (extraction) \tag{2.3.2}$$
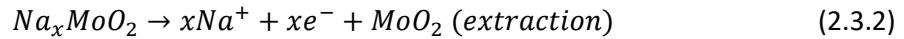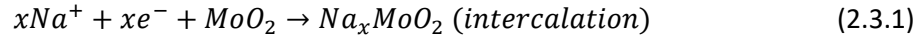
The easy diffusion of Na ions into pristine MoO$_2$ can be attributed to the fact that the Na is in a close-range order and infiltration via diffusion channels becomes possible.[28] Annealed samples allow sufficient space for the uptake of guest species during intercalation due to the open and longer range microstructures.[28]

Kai Zhu et al. also investigated the sodium insertion mechanisms in MoO$_2$, more specifically in Na$_{0.3}$MoO$_2$, and proposed the following equation[14]:

$$Na_{0.3}MoO_2 + xNa^+ + xe^- \rightarrow Na_{0.3+x}MoO_2 \tag{2.3.3}$$
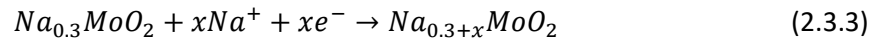
They suggest that multiphase reactions take place during insertion and deinsertion, because the XRD pattern of the fully discharged electrode does not show peaks of the molybdenum or Na-Mo alloys. They also suspect that the structural changes on the anode side are multistage phase transitions caused by reversible sodium insertion and extraction in the layered Na$_x$MnO$_2$ structure.[14]

However, both, the storage mechanism of Na and the formed surface film, require more investigations to further develop the SIB technology.

## 2.4. Raman Effect

The inelastic scattering on matter, also called Raman scattering, forms the foundation of the Raman spectroscopy.[29] In contrary to the elastic scattering (Rayleigh scattering), the frequency of the incident light is not the same as the frequency of the emitted light. This is based on the fact that part of the energy of the incident light is absorbed by, or some energy is added through the matter, which is expressed in the form of a frequency shift. More precisely, the energy exchange with light takes place

via the vibration and rotation energy of the molecules. Another contribution may originate from the exchange of energy quanta with the lattice vibration, so-called phonons.[30]

The different ways of energy exchange upon excitation are illustrated in Figure 5. The first process is the Rayleigh scattering. Here the energy hv, where h represents the Planck's constant and v the frequency, raises the energy level from the ground state to a virtual state by absorbing the incident photon. Then the level is lowered again to the ground state, releasing a photon with the same amount of energy. That is why it is also called elastic scattering, since no energy is dissipated. Rayleigh scattering is the most likely form of the three, demonstrating the highest intensity.[31]

The second possibility of energy exchange is Raman scattering, which can be divided into Stokes and Anti-Stokes scattering. The energy of the released photon is now no longer identical with that of the incident one, but is smaller or larger by the vibrational energy $hv_r$. This scattered photon and the resulting energy difference is caused by a transition from the virtual state to the excited state of molecular vibration. The Stokes scattering, where the energy of the emitted photon is lower than that of the incident one, is more likely than the Anti-Stokes scattering, because at room temperature the molecules are in the vibrational ground state rather than in an excited state. [31]



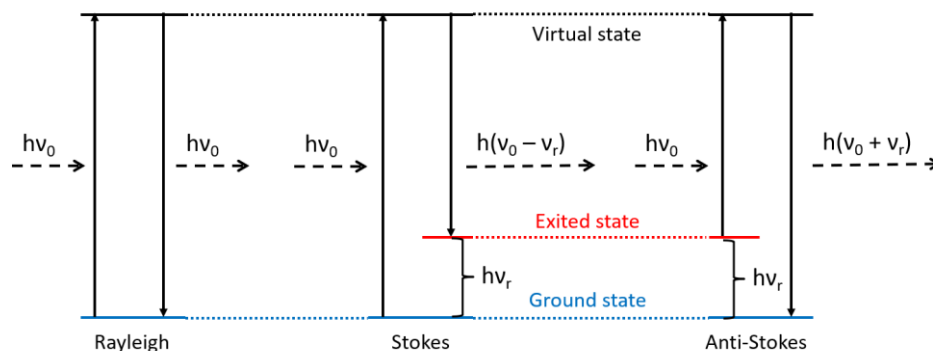Figure 5.: Illustration of Rayleigh, Stokes and Anti-Stokes scattering

The energy difference caused by the Raman effect results in a change of the wavelength of the scattered light compared to the incident light, which can be measured by Raman spectroscopy. This makes it possible to distinguish between different compounds and their different phases by means of the specific wavelength of the scattered light.

## 2.5. Physical Vapour Deposition (PVD)

Thin film deposition methods are becoming more and more important in various technical applications ranging from implementations of industrial process heat, over applications in the energy sector, for example thin-film solar cells to the manufacture of solid oxide fuel cells (SOFCs).[32–36] The Physical Vapour Deposition (PVD) is an efficient way to generate homogeneous films of various materials like metals and alloys up to a thickness to 5 µm.[37] This is done by vaporizing the coating material by means of heat, e.g.: pulsed laser deposition, or by an alternating magnet field.[38]

The method used in this work was a PVD with a pulsed magnetron. This magnetron generates an alternating magnetic field in which the argon (Ar) atoms react with electrons. An electron of the Ar atom is removed and subsequently, a positively charged Ar ion is formed, which is attracted to the cathode. The Ar ions release molybdenum atoms from the target, which interact with the oxygen in the deposition chamber and finally condensate on the about 40 °C cold support material as an oxide.

## 2.6. X-ray Photoelectron Spectroscopy (XPS)

**Working Principle**

The XPS is based on the interaction between X-rays and electrons of the material under investigation. If the energy of the incident X-ray is high enough, it detaches an electron from the surface of the material. Using the kinetic energy and the number of electrons released in this process, conclusions about the composition can be drawn. The binding energy, which is decisive for characterizing the material, can be described with the following equation[39]:

$$E_{kin} = h\nu - |E_{bind}| - \Phi_{sample} \tag{2.6.1}$$

Where $h\nu$ is the energy of the X-ray, $E_{bind}$ is the binding energy of the electron and $\Phi_{sample}$ is the work function of the material. Since every material has electrons with a certain binding energy and with a certain kinetic energy, respectively, one can draw precise conclusions about the composition of the investigated sample.[39]

## Background

In order to determine the relative amounts of the contained components, the area under the respective peaks of the several elements in the diagram is defined by fitting the individual components of the expected compounds under the curve. The course of the lower line, which defines the base of the peaks, also called background, plays an important role in the evaluation of the XPS spectra. There are three functions that are generally used to define the background. The first observed background signal shows, to the first approximation, a linear dependence with respect to the measured binding energy, which is obviously the least accurate one for more complex fittings and which therefore has not been used in this work. The second background, Tougaard, is the most accurate one, but assumes that the measurements are without instrumental influences of errors. However, XPS spectra are usually not refined well enough to apply the Tougaard background correctly, so this approach is rarely used. Thus Shirley was chosen for evaluation due to its easy handling and good performance.[39–41]

## Line Shape

To make a valid statement about the exact composition and the respective quantities of the several elements, some important fitting parameters have to be evaluated. The peak position depends on the oxidation state of the considered compound. Furthermore, the position varies with the orbital, from which the electron was released. The second important fitting parameter is the line shape, which is the geometric shape of the XPS signal of each component calculated by the program CasaXPS. The Laurentzian function and the Gaussian function are two functions which, when combined properly, are intended to provide the best possible approximation of the actual signal shape. In most cases, a ratio between them is chosen, which best describes the influences of the sample (Laurentzian) and the instrument (Gaussian). The half-width, also called full width at half maximum, which determines the maximum permissible width of the fitted peak, also has an effect in the evaluation of the XPS spectra.[39,42]

## 2.7.    X-ray Diffraction (XRD)

The three-dimensional unit cell structure of a crystalline substance can be well described by its lattice constants, which are characteristic for every crystalline structure. In X-ray diffraction, monochromatic X-rays are radiated at different angles onto the sample. If the X-ray radiation hits a lattice plane under the correct angle, a constructive interference is obtained. Such a constructive interference is given when the path difference of two or more waves are integral multiples of each other.
The relationship between the path difference and the wavelength is given by Bragg's law:

$$n \cdot \lambda = 2d \cdot \sin(\theta) \qquad (2.7.1)$$

Where n is the diffraction order, $\lambda$ is the wavelength of the X-ray, d is the distance between the lattice levels and $\theta$ is the angle between the lattice and the X-ray. If the Bragg conditions are fulfilled, the scattered X-rays add up and a signal in the diffractogram is detected. Since each crystal structure is characterized by the lattice distance, the measured diffractogram can be assigned to a certain crystallographic phase.[43]

## 2.8.    Impedance spectroscopy (PEIS/SPEIS)

To further investigate electrochemical processes within an electrochemical cell, fitting the resulting SPEIS data via an equivalent electrical circuits (EECs) using electrical elements is necessary. These idealized working elements like resistors and capacities and elements adapted to the real behaviour of electrical components like constant phase elements, are scaled in series and parallel, representing the electrical properties of the investigated electrochemical cell reproduced with an equivalent circuit diagram. In this work, the software EC-Lab V11.21 from Biologic was used to fit the curves resulting from the EEC with those of the measurements as accurately as possible. In this chapter, the most important electrical elements commonly employed in EECs are briefly discussed. The variables contained in the equations (2.8.1) to (2.8.5) are defined as follows: Z is the impedance, R the resistance, C the capacitance, f the frequency of the alternating current, j the imaginary unit, Q the variable for the constant phase element and $\alpha$ is the deviation of the angle between the function and the real axis.[44,45]

**Ideal circuit elements**

- **Resistor**: The first ideal element used for the evaluation is the resistor, defined as a passive component only owning a constant real impedance part, meaning that its value stays constant when the frequency varies and there is no phase shift between the current and the voltage.

$$Z(f) = R \qquad\qquad (2.8.1)$$

On the one hand, it describes how much ohmic resistance different parts of the electrochemical cell, for example the electrode and the electrolyte, own when an electric current pass through it. On the other hand, if it is connected in parallel with a capacitance, it can represent a faradaic resistance of an interface, governed by the reduction or oxidation of a chemical substance at an electrode.[44,45]

- **Capacitor**: The capacitor is, different to the resistor, frequency dependant. This behaviour leads to a decrease of the faradaic impedance when the frequency increases, building a vertical straight line in the imaginary positive part (-Im(Z) > 0). The phase shift between current and voltage totals -90°.

$$Z(f) = \frac{1}{Cj2\pi f} \qquad\qquad (2.8.2)$$

In electrochemical systems the capacitance is utilized to describe the charge distribution at the electrode-electrolyte interface.[44,45]

- **Inductor:** In contrast to the capacitor, the phase shift between current and voltage amounts +90° and in the Nyquist plot of an inductor shows a negative imaginary part (-Im(Z) < 0).

$$Z(f) = Lj2\pi f \qquad\qquad (2.8.3)$$

The inductor is generally not used for fitting, because it is very difficult to interpret within the EEC as it is difficult to include it in the electrode-electrolyte interface.[44–46]

**Non-ideal circuit elements**

- **Constant phase element (CPE):** This element behaves like a capacitor, it is frequency dependant and also corresponds to a straight line in the Nyquist plot, but in opposite to the ideal capacitor, the angle between the function and the real axis is not necessarily -90°, instead it is in a range of -απ/2.

$$Z(f) = \frac{1}{Q(j2\pi f)^{\alpha}}$$
(2.8.4)

- Such an element describes the often non-ideal behaviour of components in electrochemical cells caused by impurities, grain boundaries or surface heterogeneities usually better than the ideal elements mentioned above.[44,45]

- **Warburg element (W):** The phase angle between the function and the real axis is constant - π/4, meaning all absolute values of the imaginary and the real parts are equal at all frequencies, meaning the Warburg element is independent of the frequency.

$$Z(f) = \frac{\sqrt{2}\alpha}{\sqrt{j2\pi f}}$$
(2.8.5)

It is used to represent a semi-infinite linear diffusion which proceeds unrestricted to a large planar electrode.[45]

## 2.9.  Cyclic Voltammetry (CV)

The CV technique is particularly suitable for investigating oxidation and reduction processes in electrochemical cells.

An important parameter for CV measurements is the scan rate (v), which describes the change of the applied potential with time. The faster the scan rate, the smaller is the diffusion layer, which leads to higher currents. The Randles-Sevcik relation (see equation (2.9.1)) defines the relationship between the peak current and the scan rate:

$$i_P = 0.446nFAC^0 \left(\frac{NFvD_0}{RT}\right)^{\frac{1}{2}}$$

(2.9.1)

More precisely, for electrochemically reversible electron transfer processes, the relation between the linear increase of the peak current with the square root of the scan rate, with the surface area of the electrode (A), the analytical bulk concentration ($C^0$), the Faraday's constant (F), the number of electrons (n), the universal gas constant (R), the temperature (T) and the diffusion coefficient of the oxidized analyte ($D^0$).[47]

In electrochemical kinetics, one of the most fundamental equations is the Butler-Volmer equation:[48]

$$j_A = \frac{i}{nFA} = C_A \cdot k^0 \cdot e^{\left[-\alpha \cdot \frac{nF}{RT} \cdot (E-E^0)\right]} - C_B \cdot k^0 \cdot e^{\left[(1-\alpha) \cdot \frac{nF}{RT} \cdot (E-E^0)\right]}$$

(2.9.2)

Where $j_A$ is the electrode current density, A is the surface of the electrode, $C_A$ and $C_B$ are the surface concentrations of the included components, $k^0$ is the standard velocity constant, $\alpha$ is the charge transfer coefficient, E is the electrode potential and $E^0$ is the equilibrium potential.

The heterogeneous charge flow, i.e. the measurable current density, thus depends on the surface concentrations of the involved reactants, the electrode potential and the standard velocity constant. The potential-dependent surface concentrations lead to a diffusion controlled mass transport due to the concentration difference to the rest of the solution.[48]

The distribution of this concentration in the diffusion layer, which grows with the time, can be calculated from Fick's second law:[48]

$$\frac{\partial c_i}{\partial t} = D_i \frac{\partial^2 c_i}{\partial x^2}$$

(2.9.3)

This equation is only valid for linear, semi-infinite diffusion which is in the most cases very well fulfilled.[48]

# 3. Experimental

In this chapter, the experimental part of the work is described. First the synthesis of the three electrode materials is explained, more precisely the setup and the measurement parameters of the thermal oxidation, the PVD and the annealing process. Then the various characterisation methods beginning with Raman spectroscopy, X-ray diffraction and ending with X-ray photoelectron spectroscopy are described. Finally, the electrochemical characterisation with all the various methods is explained.

The following nomenclature is used for the three materials: $TiO_{2-x}$-A for the titanium(IV)-oxide anatase samples, $TiO_{2-x}$-R for the titanium(IV)-oxide rutile samples, $TiO_2$-M for the amorphous titanium oxide samples and $MoO_{2+x}$ for the mixed phase samples of molybdenum(IV)-oxide and molybdenum(VI)-oxide.

## 3.1.    Synthesis of MoO$_{2+x}$

The samples examined in the following chapters were all produced by the PVD process. The thermal oxidation of the samples was not successful. However, it is also briefly explained here as a supplement.

### 3.1.1. Thermal Oxidation

The first idea for all three different electrode materials was a unified synthesis method, using a thermal oxidation process in order to have the same prerequisites as far as possible. This should help to interpret and compare the electrochemical data of the three different electrodes later on.

The thermal oxidation of $MoO_{2+x}$ was realized in a quartz tube furnace (Carbolite HST 12/600). In the first step, a layer of $MoO_3$ should be synthesized. This was done by calcinating the sample at a temperature of 550 °C for 20 h in air, since the thermodynamically stable form at this temperature and at ambient pressure is the desired $MoO_3$ as illustrated in Figure 6. This interim step was necessary in order to reduce the $MoO_3$ to $MoO_2$ at 550 °C in a gas mixture of 30% $H_2$ and 70% Ar with a flowrate of 30 cm$^3$/min for 22h in the second step as depicted in Figure 6 b).[49]
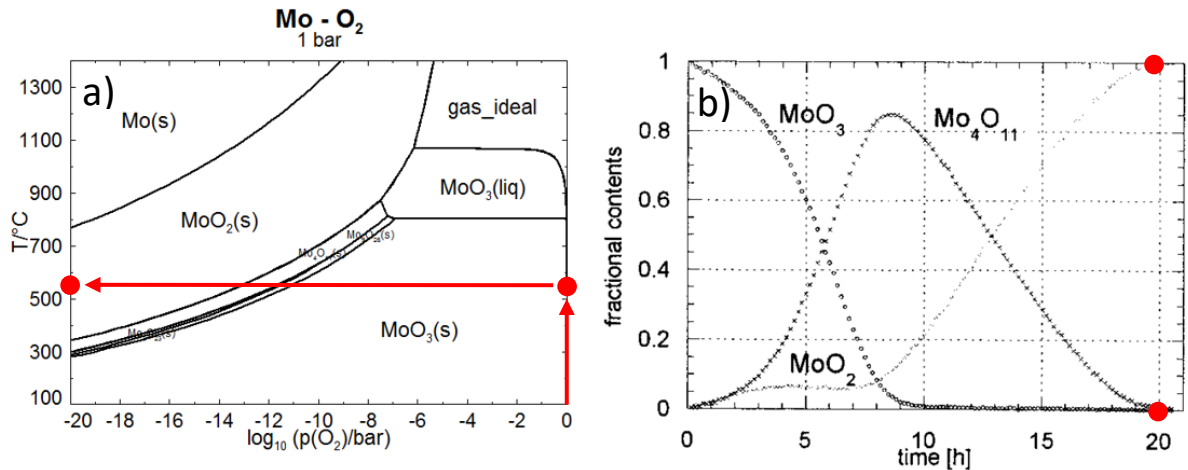
Figure 6.: a) Phase diagram of the molybdenum-oxygen system in dependence of the oxygen partial pressure and temperatures taken from reference [16], and b) Phase concentration vs. time of several molybdenum oxides during reduction in hydrogen.[49] The red arrows and points show the course of the synthesis in the diagram.

After the thermal treatment in air, a thin and uniform oxide layer, containing as few amounts of other oxides like $MoO_3$ and $Mo_4O_{11}$ as possible, should ideally be formed as it is illustrated in Figure 6 a). However, during our oxidation an apparently much too thick and inhomogeneous layer was formed, as it is shown in Figure 7. Thus, it was decided to switch to another synthesis method, because optimizing the oxide growth, which is hard to handle, would take too much time, as the required oxide layer should have a clearly definable surface in terms of thickness and uniformity. This is necessary in order to be able to relate the later results of the electrochemical investigations clearly to the surface and active mass.



Figure 7.: Sample after thermal oxidation in air at 550 °C for 22 h

## 3.1.2. PVD

The PVD was carried out with the setup shown in Figure 8, using a radio-frequency magnetron. Its principle of operation is described in more detail in chapter 2.5. The actual deposition took place on 0.1 mm thin copper plates. A vacuum-proof glass tube and the magnetron with its power supply (Figure 8 a)) form the core element of the apparatus, together with a substrate holder that can be heated to 1000 °C (Figure 8 c)). The vacuum chamber contains two pressure gauges and two yellow dosing valves by which different gases, in our case Ar and oxygen, can be injected into the chamber. Under the

magnetron, the sputter source and the mechanical shutter are situated. The lower part displayed in Figure 8 b) includes an additional yellow gas valve and a red valve for the roughing pump, also the turbo pump and a shutter can be found. A comprehensive review of the entire apparatus with its individual components was made by Götsch et.al.[38]

Several attempts were necessary to finally obtain an oxide layer not only containing $MoO_3$. The exact synthesis parameters can be found in the appendix (chapter 10.2). The synthesis of the electrodes,

which were finally used for the electrochemical characterisation, was performed as described in the following paragraph.

First the pressure in the vacuum chamber was reduced below $4 \cdot 10^{-6}$ mbar, using a roughing pump and a turbo pump (Turbo. Drive TD20 classic from Leybold vacuum). The sample holder was not heated up in order to avoid problems with sintering observed at the earlier attempts. The oxygen/Ar ratio of 1:100 was adjusted by opening the oxygen dosing valve until a pressure of $1.00 \pm 0.05 \cdot 10^{-4}$ mbar is reached. After the pressure remained constant, the oxygen shut-off valve was closed so that the currently set volume flow was available again afterwards and the same procedure was carried out with Ar, setting a pressure of $1.00 \pm 0.05 \cdot 10^{-2}$ mbar. After the pressure adjustments, the magnetron was slowly ramped up to a final output of 40 W. At the same time, the Ar and the oxygen valves



Figure 8.: Setup for physical vapour deposition containing a) upper part with vacuum chamber and oxygen-/ Ar valves b) lower part with roughing-/turbo pump and Ar valve c) finished sample

were opened completely to allow the plasma to build up at a power around 10 W. In order to prevent impurities on the surface of the target from affecting our synthesis, Ar sputtering was performed for one hour with the shutter closed before the actual deposition started. After 60 minutes the shutter

and the oxygen valves were closed again, all pumps were shut down and the Ar valve was opened slowly in order to flood the chamber.[11]

After the synthesis, it was important that the sample remained as short as possible in air, since the $MoO_{2+x}$ on the surface immediately oxidizes to $MoO_3$. Despite immediate transfer of the sample into the glove box by means of a self-made, Ar-filled container, a short contact with air was unavoidable forming a phase mixture of both $MoO_2$ and $MoO_3$ oxides, as can be seen in the XPS evaluation in Figure 16. The occurrence of this mixed phase on the surface is also noted by other working groups, for example by Wenguang Zhang et al. and Jianfeng Huang et al.[50,51]

## 3.2.  Synthesis of TiO$_{2-x}$-A

The synthesis of TiO$_{2-x}$-A is divided into three main steps, the preparation process, the electrochemical oxidation and the annealing. First of all, the metallic titanium disk (Advent, 99.6%) with a diameter of 18 mm and a thickness of 1 mm was polished with SiC grinding papers (P1200, P2500 and P4000 from Buehler) three times for five minutes each (Figure 9 a)). After every polishing step, the sample was cleaned in ethanol in an ultrasonic bath for 5 minutes.[52]
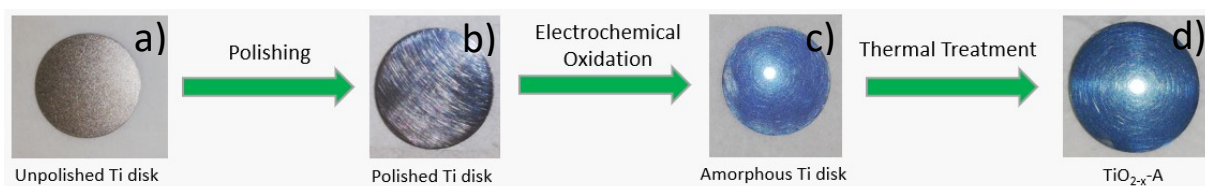


Figure 9.: All sequences of the synthesis, starting with polishing, followed by the electrochemical oxidation into amorphous TiO$_{2-x}$ and ending with the thermal annealing of the sample to TiO$_{2-x}$-A.

In the second step, the electrochemical oxidation, an amorphous $TiO_2$ layer is formed on the polished sample (Figure 9 b)). For the electrochemical oxidation, a two electrode setup (shown in Figure 10) with a copper plate as current collector, the titanium disc as working electrode and a platinum counter electrode was used. The electrolyte was 0.1 M $H_2SO_4$. A sealing ring between the titanium disk and the cell case prevents leakage of the electrolyte. After cell assembly, a constant potential of 20 V was applied for 60 minutes with an initial voltage ramp of 1 V sec$^{-1}$.[52,53]
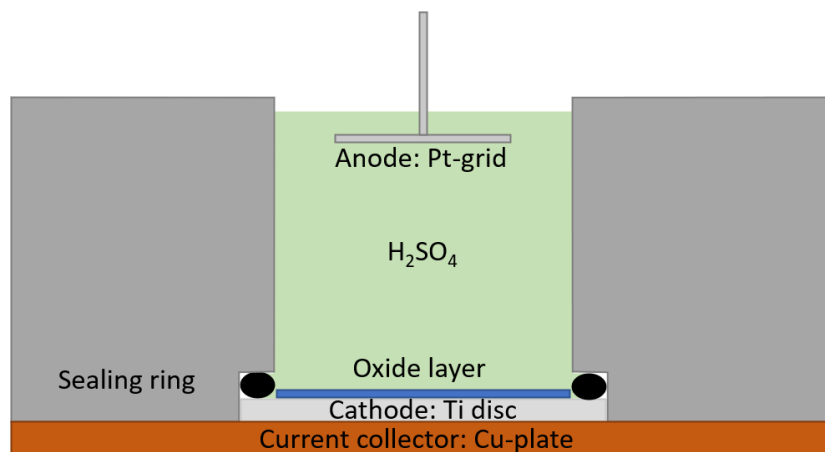
Figure 10.: Schematic cross section of the two electrode setup with a copper current collector, titanium WE, platinum CE and 0.1 M $H_2SO_4$ for electrochemical oxidation of amorphous $TiO_{2-x}$.

The third and last step of the $TiO_{2-x}$-A synthesis was the phase transition from the amorphous titanium into the anatase phase, taking place in a Carbolite furnace with quartz tube reactor depicted in Figure 11 b). Initially, the reactor was flushed for 90 minutes at room temperature with 600 sccm Ar to remove the ambient air inside. Then the Ar flow was decreased to 200 sccm, which remained constant until the end of the annealing process. The temperature was stepwise increased from room temperature up to 200 °C in 20 minutes, up to 300 °C in 20 minutes and up to 400 °C in 33 minutes. This should reduce thermal stresses inside the sample. The final temperature of 400 °C was kept constant for 300 minutes to ensure a complete phase transition. Subsequently, the furnace was cooled down to room temperature.[54]
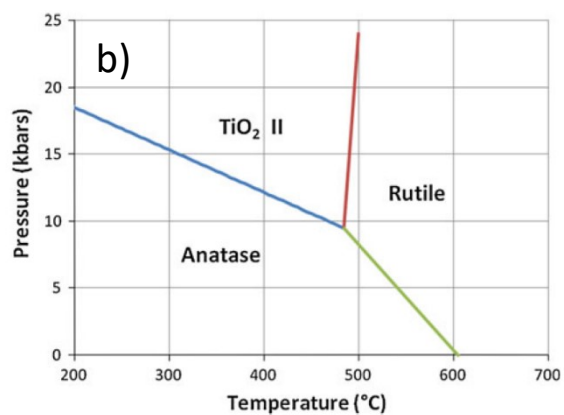


Figure 11.: a) Anneling furnace with the quartz boat inside the quartz tube, and b) Phase diagram of $TiO_2$ – temperature against pressure.[55]

Several attempts to synthesise the rutile phase of the titanium oxide were also made. Since no test cells were built with these samples because of synthesis failure, it is not explained here in detail, but in the appendix (chapter 10.3).

## 3.3. Raman Spectroscopy

The characterisation of the $TiO_{2-x}$-A samples was performed by Raman spectroscopy using a WiTec alpha 300 Raman microscope with an objective providing a 40x magnification including a confocal laser scanning microscope with a wavelength of 532 nm. The use of such a confocal microscope makes it possible to scan the sample sequentially producing a sharp 2D image by a pinhole aperture that only allows the beam path of the sharply imaged area to pass through. The integration time for each measurement was about three minutes and the applied grid had a mesh size of 1800 lines/mm. For the measurement control and data evaluation, the software WiTec Control 5.1 was used.

## 3.4. Assembling a Battery Half Cell

For all electrochemical measurements, an ECC-Ref-Cell as shown in Figure 12 was used.[56] The whole assembling process was carried out in a glove box filled with Ar, containing contents of $H_2O$ and $O_2$ below 0.1 ppm, due to the reactivity of the $MoO_{2+x}$ with oxygen and the hazardous reactivity of the used sodium with oxygen and humidity, respectively.
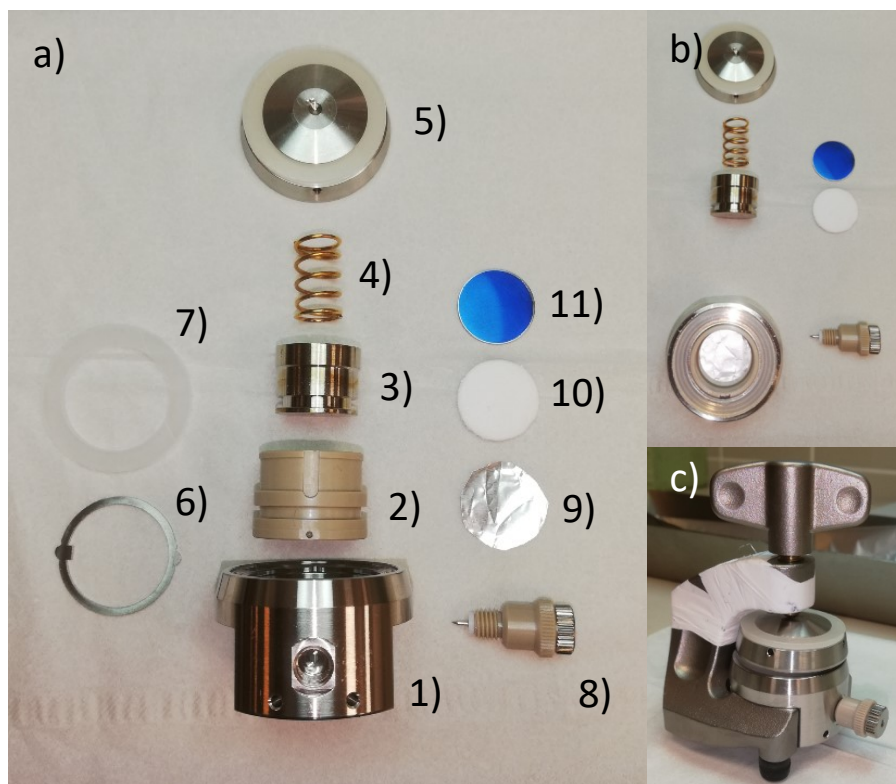
Figure 12.: Exploded view of the ECC-Ref Electrochemical Cell used for all EC measurements showing a) all cell parts: 1) cell base, 2) PEEK sleeve, 3) plunger, 4) gold spring, 5) lid, 6) centring ring, 7) sealing ring, 8) reference electrode pin, 9) symbolically represented sodium foil, 10) separator and 11) working electrode; b) semi-assembled cell and c) fully assembled cell.[56]

A 0.1 to 0.5 mm thick sodium metal foil (99.9%) counter electrode (CE) was prepared and mounted in the stainless-steel cell base, having a diameter of 16 mm. Subsequently, the PEEK sleeve, with the Na reference electrode (RE) was added, avoiding contact with the CE already inside the cell base. The glass fibre separator (EL-Cell, 18x1.55 mm) was placed into the PEEK sleeve and 500 µl of the 99.9 % pure electrolyte, containing 1M Na FSI (Bis(fluorosulfonyl)imide) in 1:1 V/V ethylene carbonate:dimethyl carbonate from Solvionic, was piped onto it.[57] Afterwards, the working electrode (WE) and the plunger were put in the sleeve, fixing the cell stack. As last step, the RE pin was assembled and gold spring and the lid were put onto the plunger and the cell was positioned in the bracket and was fixed with the wing nut shown in Figure 12 c).[56,44]

**Cells for post mortem analysis**

For additional ex-situ emersion analysis (see chapter 4.8 and chapter 4.9), the electrochemical test cells were prepared as shown in Figure 13 b).
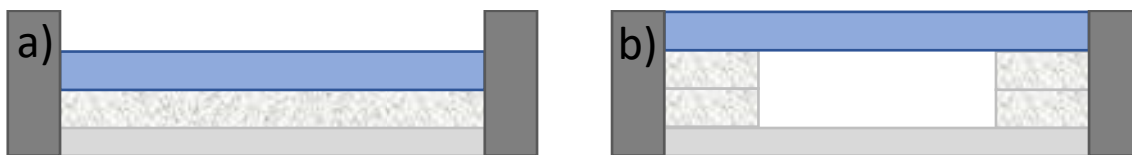


Figure 13.: Schematic cross-section of the electrochemical test cell ECC-Ref for a) standard electrochemical characterization, and b) ex-situ emersion analysis with a punched, double spaced separator. The lower part in grey is the sodium on which the white structured separator lies. On top, the blue working electrode and the indicated cell (black) can be seen.

To investigate any potentially formed surface film after the electrochemical characterisation, it was necessary to avoid contact with the separator so that it did not impede the growth of the film. Another reason was, that the $MoO_{2+x}$ film was partly removed together with the separator when the cells were disassembled, which made ex-situ surface analysis impossible. To prevent a short circuit of the WE and the CE, two separators were placed on top of each other in order to increase the distance between the electrodes. To avoid that Ar in the cell distorts the measurements, 1200 μl of the electrolyte instead of 500 μl were used in the $TiO_{2-x}$-A cell and 1300 μl instead of 500 μl were used in the $MoO_{2+x}$ cell, respectively. The diameter of the hole in the separator was 7 mm, but this does not correspond to the finally exposed area in the cell, because during assembly, the separators are compressed and thus the hole becomes smaller.

## 3.5. C-Rates

This chapter briefly describes how the C-rates were calculated. The C-rate defines the charge or discharge current related to the nominal capacity. With a C-rate of one, the respective battery needs exactly one hour to be fully discharged or recharged. To compare all cells among each other, the C-rates of the $TiO_{2-x}$-A were taken for all of them, even though the calculated currents of the various materials were different.

Table 2 shows all values required for the calculation.

Table 2.: All parameters for the $cap_{max}$ calculation for $TiO_{2-x}$-A, $TiO_2$-M and $MoO_2$.

| Parameter | Unit | $TiO_{2-x}$-A | $TiO_2$-M | $MoO_2$ |
|---|---|---|---|---|
| $h_1$ | [nm] | 40[58–60] | 40[58–60] | 50 |
| $h_{2,min}$ | [nm] | 220 | 220 | 199 |
| $h_{2,max}$ | [nm] | 276 | 276 | 219 |
| d | [mm] | 17.0±0.05 | 17.0±0.05 | 17±0.05 |
| ρ | [g/cm³] | 3.84[61,62] | 2.9[62] | 6.44-6.51[63]‡ |
| $M_{total}\,h_1$ | [g] | $3.486 \cdot 10^{-5}$ | $2.633 \cdot 10^{-5}$ | $7.263 \cdot 10^{-5}$ |
| $M_{total}\,h_{2,min}$ | [g] | $1.917 \cdot 10^{-4}$ | $1.448 \cdot 10^{-4}$ | $2.891 \cdot 10^{-4}$ |
| $M_{total}\,h_{2,max}$ | [g] | $2.406 \cdot 10^{-4}$ | $1.817 \cdot 10^{-4}$ | $3.181 \cdot 10^{-4}$ |
| MM | [g/mol] | 79.865 | 79.865 | 127.958 |
| $cap_{theory}$ | [mAh/g] | 335.58† | 335.58† | 209.45† |
| $Cap_{max}\,h_1$ | [mAh] | $1.170 \cdot 10^{-2}$ | $8.836 \cdot 10^{-3}$ | $1.521 \cdot 10^{-2}$ |
| $Cap_{max}\,h_{2,min}$ | [mAh] | $6.464 \cdot 10^{-2}$ | $4.860 \cdot 10^{-2}$ | $6.055 \cdot 10^{-2}$ |
| $Cap_{max}\,h_{2,max}$ | [mAh] | $8.102 \cdot 10^{-2}$ | $6.097 \cdot 10^{-2}$ | $6.663 \cdot 10^{-2}$ |
| $Cap_{max}\,h_{2,middle}$ | [mAh] | $7.283 \cdot 10^{-2}$ | $5.479 \cdot 10^{-2}$ | $6.359 \cdot 10^{-2}$ |

† See equation (3.5.1) and (3.5.2), ‡ calculated with 6.4

The layer thicknesses $h_1$, $h_{2,min}$ and $h_{2,max}$ for $MoO_{2+x}$ and $TiO_{2-x}$-A were determined directly from Figure 18 and Figure 19, respectively. The diameters for the titanium electrodes in Table 2 are diameters of the active area and not the entire diameter, which is 18 mm, since the sealing ring covered a part of the WE disc during electrochemical oxidation.

The total mass was then calculated with following equation:

$$M_{total} = \frac{d^2 \pi}{4} \cdot \frac{h}{10^6} \cdot \frac{\rho}{1000}$$

(3.5.1)

The next step was the determination of the theoretical capacity dividing the Faraday constant through the molar mass of $TiO_2$ and $MoO_2$, respectively, assuming that $NaTiO_2$ and $NaMoO_2$ is the compound with the highest sodium content: [9,28]

$$cap_{theory,TiO_2} = \frac{F}{MM_{TiO_2}} = \frac{96485 \frac{As}{mol}}{79.865 \frac{g}{mol}} = 1208.10 \frac{As}{g} = 335.58 \frac{mAh}{g}$$

(3.5.2)

$$cap_{theory,MoO_2} = \frac{F}{MM_{MoO_2}} = \frac{96485 \frac{As}{mol}}{127.958 \frac{g}{mol}} = 754.04 \frac{As}{g} = 209.45 \frac{mAh}{g} \tag{3.5.3}$$

As a final step, the applied currents displayed in Table 3, column 4, were calculated by multiplying the theoretical capacity with the mass, using the estimated layer thickness of the $TiO_{2-x}$ and $MoO_{2+x}$ from SEM analysis. The C-rates of $TiO_{2-x}$ and $MoO_{2+x}$ are determined by dividing the target current through the actual current ($Cap_{max}$ $h_{2,middle}$ for one hour).

Table 3.: C-rates and applied currents of $TiO_{2-x}$-A, $TiO_2$-M and $MoO_{2+x}$.

| C-rates $TiO_{2-x}$-A | C-rates $TiO_2$-M | C-rates $MoO_{2+x}$ | Applied Current |
|:---:|:---:|:---:|:---:|
| [µA] | [µA] | [µA] | [µA] |
| 0.016 C | 0.016 C | 0.018 C | 1.2 |
| 0.032 C | 0.032 C | 0.037 C | 2.5 |
| 0.080 C | 0.081 C | 0.092 C | 6 |
| 0.161 C | 0.161 C | 0.184 C | 12 |
| 0.321 C | 0.323 C | 0.368 C | 24 |
| 0.803 C | 0.806 C | 0.920 C | 59 |
| 1.606 C | 1.613 C | 1.840 C | 117 |

# 4. Results and Discussion

## 4.1. Raman Spectroscopy of TiO$_{2-x}$-A

In Table 4, the characteristic Raman scattering maxima of various TiO$_2$ isotopes representing the TiO$_{2-x}$-A Raman spectrum are shown. It should be noted that the wavenumbers of the characteristic modes are subject to variations, since the measurement and the resulting positions of the peaks depend on several factors such as temperature, isotope state, sample shape and state of aggregation, respectively.

Table 4.: Raman shifts of the Ti$^{18}$O$_2$, Ti$^{17}$O$_2$ and Ti$^{16}$O$_2$ anatase at 295 K.

| Mode/cm$^{-1}$ | Ti$^{16}$O$_2$ | Ti$^{17}$O$_2$ | Ti$^{18}$O$_2$ | Reference |
|---|---|---|---|---|
| E$_g$(1) | 144 | 146 | 143 | [64] |
| E$_g$(2) | 196 | 193 | 186 | [64] |
| B$_{1g}$(1) | 394 | 397 | 395 | [64] |
| B$_{1g}$(2)+A$_{1g}$ | 516 | 505 | 492 | [64] |
| E$_g$(3) | 638 | 623 | 604 | [64] |
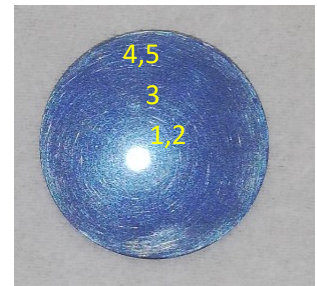


Figure 14.: Measurement points

The TiO$_{2-x}$-A measurement shown in Figure 15 contains 5 spectra measured at different positions (Figure 14) on the TiO$_{2-x}$-A electrode. The vertical, black lines in Figure 15 indicate the mean wavenumber of the peak maxima in the 5 spectra.
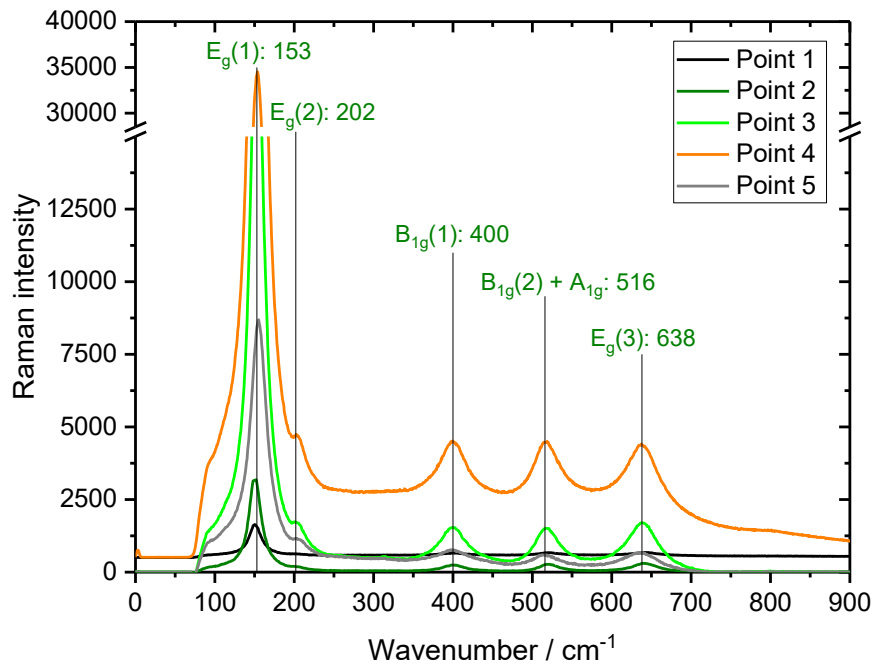
Figure 15.: Measured Raman spectra of $TiO_{2-x}$-A at various measurement points shown in Figure 14.

All $E_g(1)$ peaks in the spectra show maxima around 153 cm$^{-1}$, whereas the theoretical peak maximum is between 143 and 146 cm$^{-1}$ (Table 4). Also, the $E_g(2)$ peak maxima are not in the theoretical peak range of 186-196 cm$^{-1}$, but slightly shifted to higher wavenumbers of 202 cm$^{-1}$. Thus, both peaks show a positive shift of about 7-10 cm$^{-1}$ and 6-16 cm$^{-1}$, respectively, compared to the literature values (Table 4). This indicates a possible inaccuracy during the measurement, possibly caused by a slightly misaligned focus. The three other peaks at 400 cm$^{-1}$, 516 cm$^{-1}$ and 638 cm$^{-1}$ are in agreement with the theoretical values for $Ti^{16}O_2$. Additionally, the Raman intensity is high, indicating a thick oxide layer, which leads to a conclusive result. However, even if deviations can be detected, the evaluation clearly proofs that the synthesis was successful, because only the peaks from the anatase phase can be seen and no peaks at other positions, which might indicate a mixed phase of additional rutile or other phases.

## 4.2. XPS analysis

The XPS analysis before the electrochemical characterisations was made for the $MoO_{2+x}$ and $TiO_{2-x}$-A samples. For the $MoO_{2+x}$, on the one hand the exact ratio of Mo(IV)-oxide and Mo(VI)-oxide had to be determined, and on the other hand the sample had to remain in air as short as possible. Therefore, XPS seems the most suitable and available method. The evaluation was done by CasaXPS, using a Shirley background setting and GL(30) as the line shape (see chapter 2.6).

During the emission process, photoelectrons are lost, which leads to a steadily increasing positive charge on the sample. Consequently, the kinetic energy of the emitted photoelectrons decreases, which in turn leads to a shift of the peaks to a higher binding energy. So, the C1 peak was shifted to 285 eV, thus shifting the entire spectrum to compensate this effect.[65] All shifted peak positions and widths of $MoO_{2+x}$ and $TiO_{2-x}$-A are given in Table 5.

Table 5.: Peak positions and half-widths of $TiO_{2-x}$-A and $MoO_{2+x}$ used for XPS evaluation.

| $TiO_{2-x}$-A | Ti $2p_{3/2}$ [eV] | FWHM [eV] | Ti $2p_{1/2}$ [eV] | FWHM [eV] | Reference |
|---|---|---|---|---|---|
| Ti(IV)-oxide | 458.59 ± 0.00 | 1.04 | + 5.72 | 1.98 | [66] |
| Ti(III)-oxide | 457.30 ± 0.70 | | +5.20 | | [67] |
| Ti(II)-oxide | 455.50 ± 0.60 | | +5.60 | | [67] |
| Ti(0) | 453.74 ± 0.02 | 0.69 | +6.05 | 0.83 | [66] |
| O1s Lattice | 529.87± 0.00 | 1.10 | | | [66] |
| O1s Hydroxide | 531.00 ± 0.04 | 2.11 | | | [66] |
| O1s $TiO_2$ | 529.87 ± 0.00 | | | | [66] |

| $MoO_2$ | Mo $3d_{5/2}$ [eV] | FWHM [eV] | Mo $3d_{3/2}$ [eV] | FWHM [eV] | Reference |
|---|---|---|---|---|---|
| Mo(IV)-oxide | 229.70 ± 0.9 | | +3.15 | | [67] |
| Mo(VI)-oxide | 233.15 ± 0.20 | 0.86 | +3.15 | 0.9 | [67]* |
| Mo(V)-oxide | 231.75 ± 0.15 | | | | [68] |
| O1s Lattice IV | 530.50 ± 0.50 | | | | [67] |
| O1s Lattice VI | 530.60 ± 0.40 | | | | [67] |
| O1s $H_2O$ | 534.40 ± 1.80 | | | | [69] |

*shift C1 to 284.8

### 4.2.1. $MoO_{2+x}$

Figure 16 shows the high-resolution Mo 3d XPS spectra of $MoO_{2+x}$. As expected, the $MoO_{2+x}$ sample consists of a phase mixture of Mo(IV)-oxide and Mo(VI)-oxide, which may originate from the instability of the Mo(IV)-oxide in air. The Mo(IV)$_{5/2}$ peak maximum (Figure 15, dark green) is located at 229.4 eV,

the Mo(IV)$_{3/2}$ peak maximum (Figure 15, dark green) at 232.5 eV, respectively. Since the spectra are shifted with respect to the C1 peak, the molybdenum peaks are not exactly at the theoretical positions, however, the deviation is small with 0.3 ± 0.9 eV for Mo(IV)$_{5/2}$ and also for Mo(IV)$_{3/2}$, compared to the literature values given in Table 5. The Mo(VI)$_{5/2}$ peak maximum (Figure 15, dark red) at 232.5 eV and the Mo(VI)$_{3/2}$ peak maximum (Figure 15, light red) at 235.6 eV also show a deviation, which amounts to 0.65 ± 0.2 eV compared to the theoretical peak position at 233.15 eV. Other oxides, such as Mo(V)-oxide, were not considered in this evaluation, as it is not expected that such oxides are present in our sample.
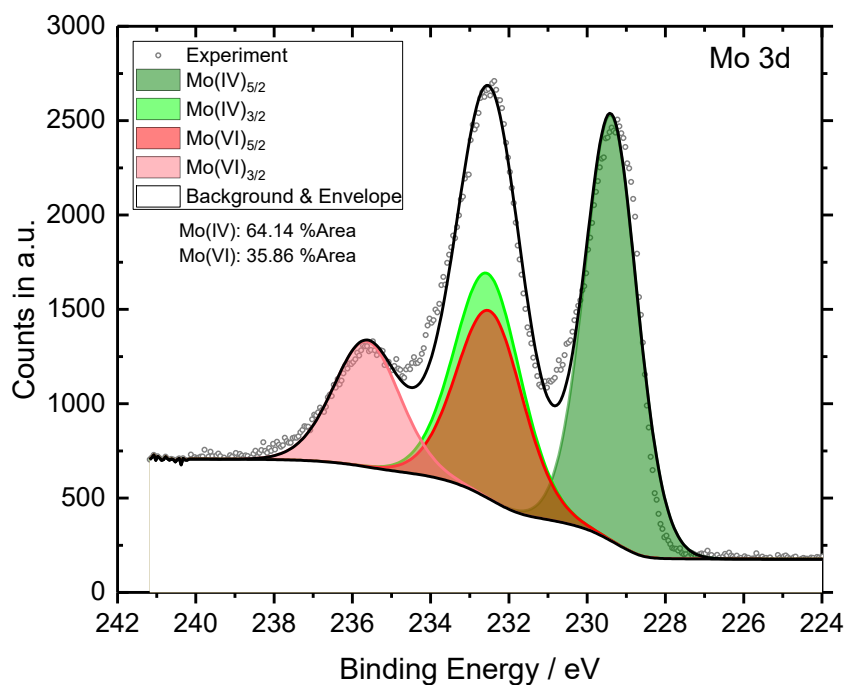


Figure 16.: Mo 3d spectra of MoO$_{2+x}$ including relative mass distribution.

In addition, if they were taken into account, the evaluation would be even less distinct, since the peaks overlap each other (peak position see Table 5), making it more inaccurate. A value of 2 was chosen for the maximum half-value width, since higher values give better results, but do not represent the true characteristics of the several fitted peaks. The distance between the two corresponding peaks is for both 3.15 eV.

In conclusion, it can be said that the synthesis of MoO$_{2+x}$ was successful.

## 4.2.2. TiO$_{2-x}$-A

The O 1s spectrum and the Ti 2p spectrum of the TiO$_{2-x}$-A electrode before the electrochemical characterisation are given in Figure 17 a) and b), respectively.
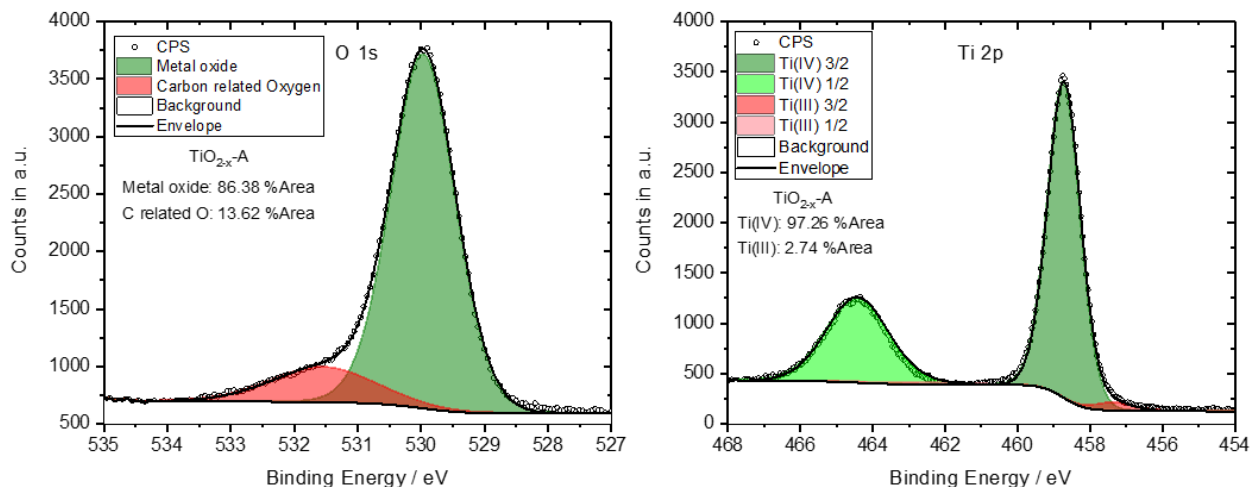


Figure 17.: a) O 1s spectrum and b) Ti 2p spectrum of TiO$_{2-x}$-A including relative mass distribution.

To check if the phase transition to TiO$_{2-x}$ was successful, XPS was performed in addition to Raman spectroscopy. Since the sample did not get in contact with the electrolyte, the surface only contains Ti, O and C species (see Figure 55). The total ratio of Ti/O/C amounts 25.77%/59.92%/14.31%. In Figure 17 a), the O 1s spectrum with the two fitting components metal oxide and carbon related oxygen is depicted. The area of the O 1s spectrum related to metal oxide (TiO$_2$) amounts 86.38% and the area related to carbon compounds amounts 13.62%. Figure 17 b) shows the Ti 2p spectrum with the two fitting components Ti(IV) and Ti(III). The presence of Ti(III) is caused by oxygen defects and totals 2.74%. Since all carbon compounds on the sample surface are created unintentionally by contact with air, they are not treated further and are declared as adventitious carbon. The corresponding C 1s spectrum is shown in Figure 54.

The ratio between Ti and O can be calculated as follows:

$$Ti/O \rightarrow 25.77/(59.92 \cdot 0.8638) \rightarrow 25.77/51.76 \rightarrow 1/2.01 \qquad (4.2.2.1)$$

This Ti/O ratio of 1/2.01 proves that the synthesis by means of electrochemical oxidation described in chapter 3.2 was successful.

## 4.3. Scanning electron microscopy (SEM)

**Previous analysis**

To calculate the active mass and thereupon the C-rates, respectively, the exact thickness of the PVD made $MoO_{2+x}$ layer and the amorphous $TiO_2$ layers had to be determined. Therefore, cross sections are investigated with SEM. For that, the $MoO_{2+x}$ layer was sputtered onto a 0.1 mm thick copper sheet. The electrochemical oxidation of the $TiO_{2-x}$-A was realized with a 0.125 thick titanium foil instead of the 1 mm thick titanium disc. Then, both were cut with a focused helium ion beam. Advantage of the fib-cut is the clean cutting edge, which is indispensable to determine the thickness correctly.
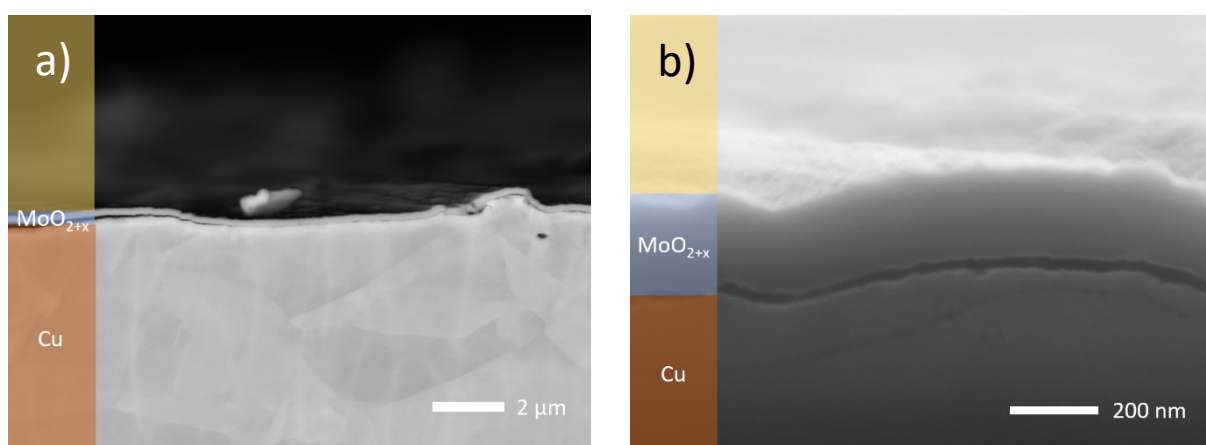


Figure 18.: Cross-section SEM images of $MoO_{2+x}$ a) overview and b) zoom.

In the lower part of Figure 18 a) the copper bulk can clearly be seen, on top of which the uniformly sputtered $MoO_{2+x}$ can be observed. This layer is not only advantageous for electrochemical analysis because of the very uniform surface, it also makes it easy to determine the average layer thickness precisely. Therefore, five thicknesses were measured from each of the two images in Figure 18 a) and b) at different positions and the average value was calculated. For $MoO_{2+x}$ the average layer thickness is 209 ± 10 nm.
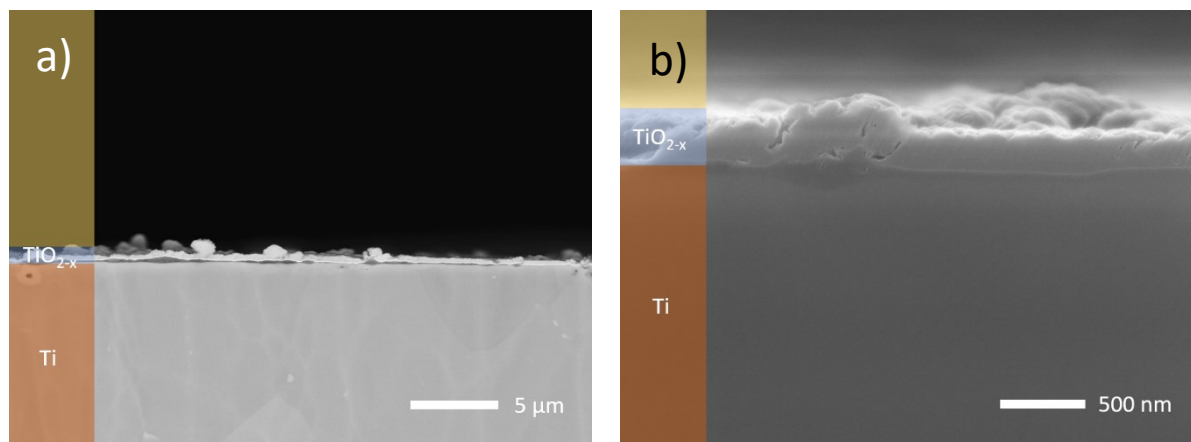
Figure 19.: Cross-section SEM images of $TiO_{2-x}$-A a) overview and b) zoom.

Also for the $TiO_{2-x}$-A electrodes SEM measurements were performed and the resulting images can be seen in Figure 19. The $TiO_{2-x}$-A layer isn't as uniformly as the $MoO_{2+x}$ laxer is, since the electrochemical oxidation does not produce such a uniform oxide layer as is the case with the PVD. This can be seen in Figure 19 a), where several grains and elevations can be located on the surface. Such an elevation is also seen in Figure 19 b). However, the layer is sufficiently uniform to determine an average layer thickness, as was done with $MoO_{2+x}$, which is, in the case of $TiO_{2-x}$-A, 248 ± 28 nm.

The calculation of the active mass, which was enabled with these images, can be found in chapter 3.5.

## 4.4. Electrochemical impedance spectroscopy

To understand the electrochemical processes within the $TiO_{2-x}$-A battery cell, potential dependent electrochemical impedance spectroscopy (PEIS) was performed. Measurements at open cell voltage (OCV) were carried out before and after the CV and the GCPL measurements to investigate the impedance characteristics of the battery half-cells after long-term cycling.

### 4.4.1. $TiO_{2-x}$-A

Figure 20 compares the different PEIS graphs before and after the CV measurements (see Figure 22), and before and after 310 GCPL cycles (see Figure 29). Therefore, the respective Nyquist plot of every measurement is shown in Figure 20 a) and a magnification of the region up to 2 kΩ is shown in Figure 20 b).
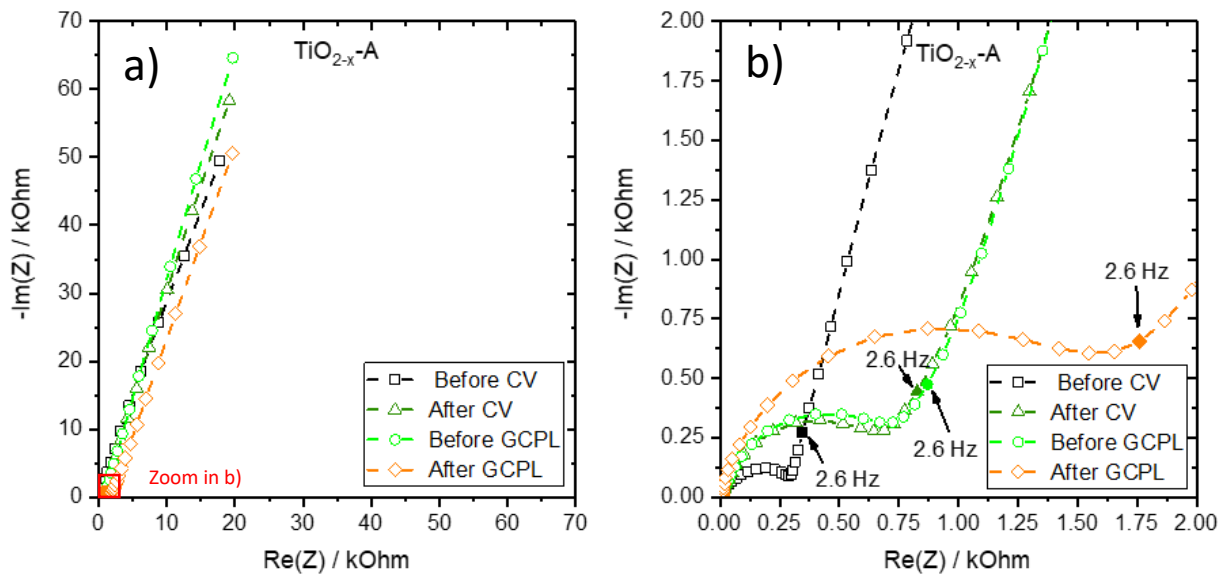
Figure 20.: Nyquist plots of TiO$_{2-x}$-A electrodes from 10 kHz to 5 mHz before CV, after CV, before GCPL (after 310 cycles) and after GCPL measurements.

The distance on the real axis between the origin of the graph and the measuring point with the highest frequency represents the ohmic resistance, more precisely the resistance of the electrolyte and the contact resistance of the cell.[70] The semicircle formed in the frequency region until 8 Hz for the spectra before the GCPL and until 4 Hz for the spectra after the GCPL is related to charge transfer processes, which take place at the electrode interface. This charge transfer process represents the solid/electrolyte interface including the electrolyte double-layer capacitance and the corresponding Na ion transfer parameters. The increasing radius of the semicircle after long-term galvanostatic cycling is attributed to the formation of the surface film causing the increasing impedance and charge transfer resistance.[8,70] The straight line at low frequencies (below 2.6 Hz) is related to the diffusion of Na ions in electroactive particles, either within the formed surface film, or in the subjacent anatase bulk structure.[70]

## 4.4.2. MoO$_{2+x}$

The different PEIS graphs before and after the CV measurements shown in Figure 27, and before and after 300 GCPL cycles (see Figure 31) of MoO$_{2+x}$ are shown in Figure 21. The respective Nyquist plot of every measurement is depicted in Figure 21 a). For a better comparison, the impedance values up to 4 kΩ, 400 Ω and 80 Ω are shown in Figure 21 b), c) and d), respectively.

The detailed explanation of the semicircle at middle frequencies and the straight slope at low frequencies have been previously declared in chapter 4.4.1.[8,70]
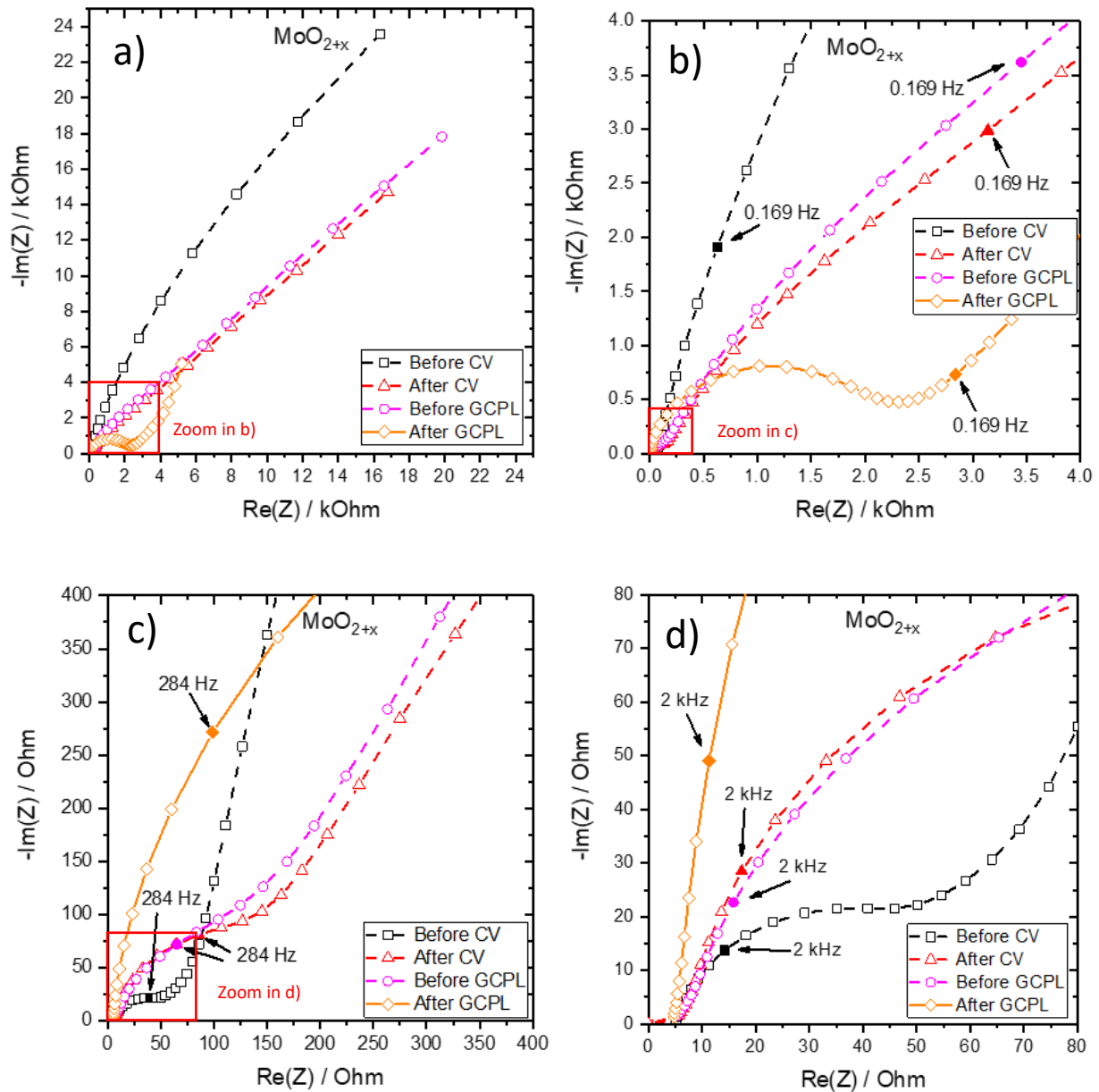


Figure 21.: Nyquist plots of $MoO_{2+x}$ from 10 kHz to 5 mHz a) before CV, b) after CV, c) before GCPL, and d) after GCPL measurements (300 cycles).

The radius of the semicircle before the CV measurement amounts about 25 Ω and is increasing to a value of 1 kΩ for the semicircle after the GCPL measurement. Compared to the semicircles of the $TiO_{2-x}$-A shown in Figure 20 b), the semicircles of the $MoO_{2+x}$ depicted in Figure 21 b) and c) have

approximately the same radius, which suggests that the surface film should have the same thickness. However, the SEM measurements shown in chapter 4.9 do not confirm this.

## 4.5.    Cyclic Voltammetry

In this chapter, the CVs of $TiO_{2-x}$-A, $TiO_2$-M and $MoO_{2+x}$, are discussed. All measurements were carried out between 0.1 V and 3 V vs. $Na/Na^+$. The capacities were normalized, on the one hand to the surface area, and on the other hand to the active mass. The surface area totals 0.227 $cm^{-2}$ and the active mass 2.17 $\cdot 10^{-4}$ g. The equations used for the calculation of the active mass and the active surface area are given in chapter 10.6.

### 4.5.1. $TiO_{2-x}$-A

Figure 22 depicts the CV of the initial $TiO_{2-x}$-A sample, meaning before the GCPL measurements, at different scan rates from 200 mV $s^{-1}$ to 0.1 mV $s^{-1}$.
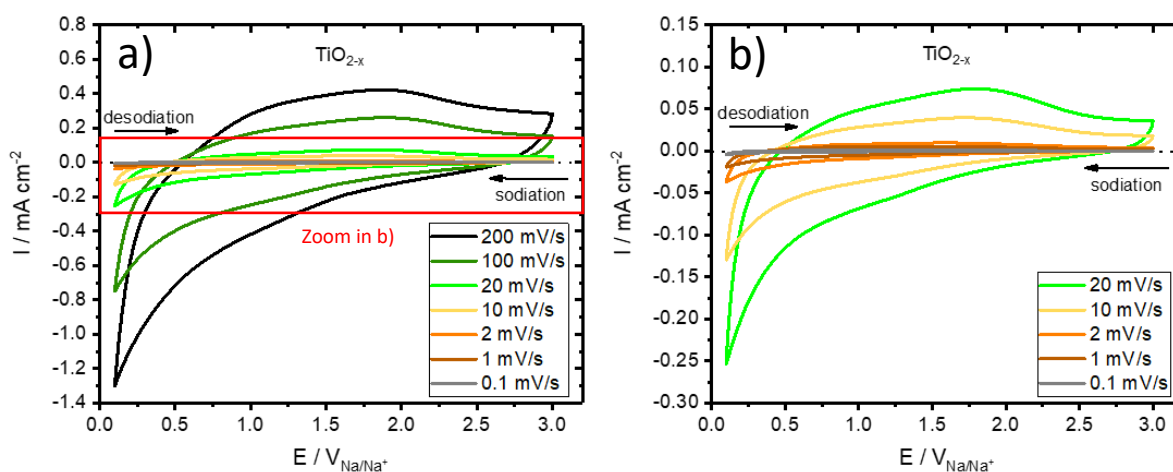


Figure 22.: CV of initial $TiO_{2-x}$-A at different scan rates from a) 200 mV $s^{-1}$ down to 0.1 mV $s^{-1}$ and zoomed from b) 10 mV $s^{-1}$ down to 0.1 mV $s^{-1}$.

The progression of the curves obtained at different scan rates are all characterized by a similar behaviour. The cathodic current that starts already at 2.6 V, increases continuously to the vertex potential of 0.1 V. The observed reductive current is attributed to electrolyte decomposition together with surface film formation. This formation of a surface film may be explained by the reduction of solvent molecules and anions present in the electrolyte, which generate reduction products that are deposited on the surface of the active material, as reported by Portenkirchner et al., among others.[8,71] Otherwise, no distinct cathodic or anodic peaks can be seen.

The comparison of the initial sample (black) and the aged sample (green), which has gone through 310 GCPL cycles of various sodiation rates (see Figure 29), can be seen in Figure 23 a) and b). The initial line in both graphs shows only one distinctive cathodic peak and no anodic peak as described in the previous paragraph. The aged samples exhibit a prominent anodic peak located at 1.69 V at a scan rate of 200 mV s$^{-1}$ and 0.85 V at a scan rate of 1 mV s$^{-1}$, respectively. In addition, a cathodic peak is formed with a maximum at 0.34 V at a scan rate of 200 mV s$^{-1}$ and a maximum at 0.73 V at a scan rate of 1 mV s$^{-1}$. The voltage offset between the cathodic and the anodic peak, also called hysteresis, amounts 1.35 V (200 mV s$^{-1}$) and 0.12 V (1 mV s$^{-1}$). This hysteresis can be attributed to the kinetic limitation of the reversible storage of sodium ions in the structure of the active material in combination with a $Ti^{4+}$ reduction in the case of sodiation and a $Ti^{3+}$ oxidation in the case of desodiation.[8,71,72]
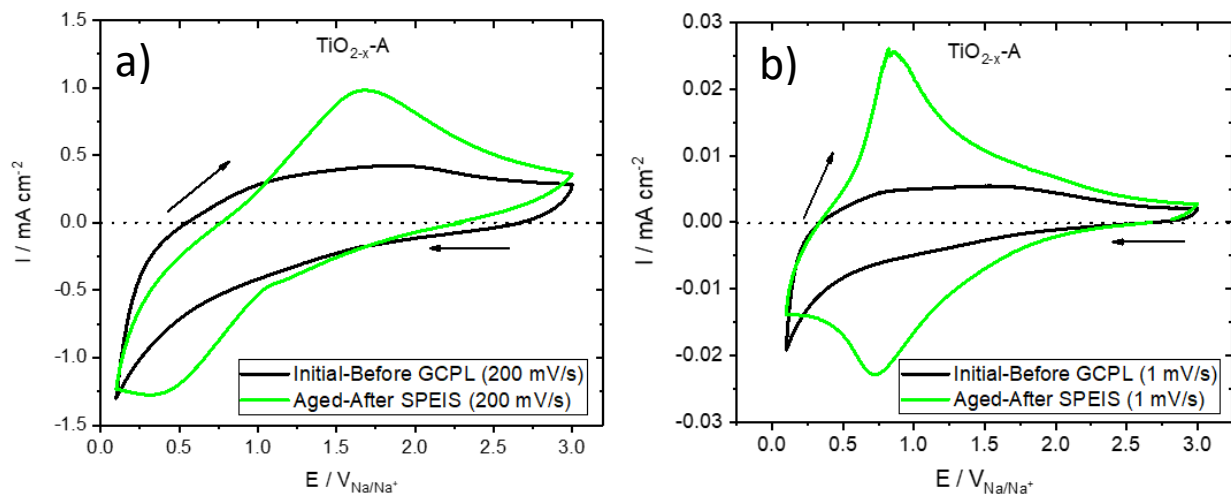


Figure 23.: CVs of TiO$_{2-x}$-A for the initial and aged (after 310 GCPL cycles) sample between 3.0 and 0.1 V for a scan rate of a) 200 mV s$^{-1}$ and b) 1 mV s$^{-1}$.

The current improvement at voltages below 0.5 V results most probably from the formation of a surface film or solid electrolyte interface (SEI) due to electrolyte decomposition as already mentioned in the description to Figure 22 and can be supported by impedance analysis and XPS following in the chapters 4.7 and 4.8.[8]

In general, the measurement results agree well with the publication of Engelbert Portenkirchner et al. and previous results of Sebastian Rommel, who also investigated titanium-based anodes, more precisely TiO$_2$ amorphous, anatase and carbon coated nanotube electrodes for SIB.[8,73]

The last evaluation is the comparison of the CVs of the aged samples at different scan rates, illustrated in Figure 24. The peak current density is decreasing with decreasing scan rates, starting at -1.29/0.93 mA cm$^{-2}$ for the anodic/cathodic peak at 200 mV s$^{-1}$ resulting at -0.02/0.03 mA cm$^{-2}$ at 1 mV s$^{-1}$ (Figure 25 a)).

The peaks for the high scan rates can be located at 1.68 V and 0.34 V for a scan rate of 200 mV s$^{-1}$ and 1.51 V and 0.45 V for a scan rate of 100 mV s$^{-1}$ (Figure 25 b)). Especially the cathodic peaks show a mixed influence of electrolyte decomposition and formation of a surface film, due to the relatively broad shape of the peaks.[74] Differently, the anodic peaks are quite well defined related to the reversible Na release.[74]

However, the peaks for the slower scan rates are all showing a pair of sharp anodic and cathodic peaks at 1.17/0.66 V for 20 mV s$^{-1}$, 1.05/0.71 V for 10 mV s$^{-1}$, 0.91/0.75 V for 2 mV s$^{-1}$ and 0.87/0.73 V for 1 mV s$^{-1}$, respectively, relating to the reversible sodiation and desodiation.[8]
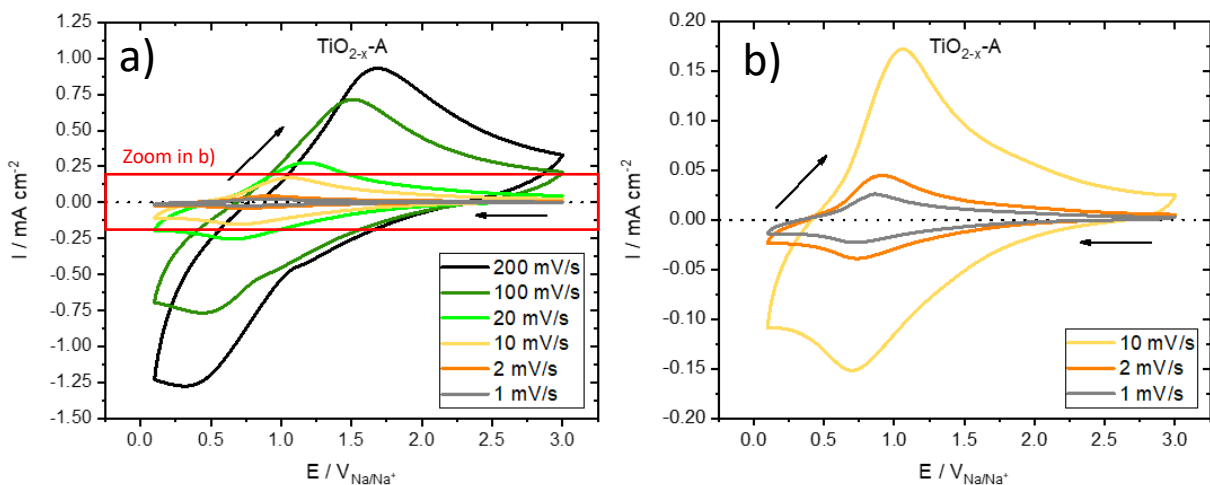


Figure 24.: CV of TiO$_{2-x}$-A for the aged sample between 3.0 and 0.1 V for the scan rate of a) 200 mV s$^{-1}$ to 1 mV s$^{-1}$, and b) detailed view of CVs with slow scan rate from 10 mV s$^{-1}$ to 1 mV s$^{-1}$.

The potential difference between the related anodic and cathodic peaks is an indicator for the kinetic characteristics of the sodiation/desodiation reaction. It decreases with decreasing scan rates, beginning with 1.34 V at 200 mV s$^{-1}$ ending with 0.14 V at 1 mV s$^{-1}$. This decreasing potential difference indicates that the sodium storage process is kinetically limited and it shows accordingly that the reversibility of the sodium storage process increases with decreasing scan rates.[75]
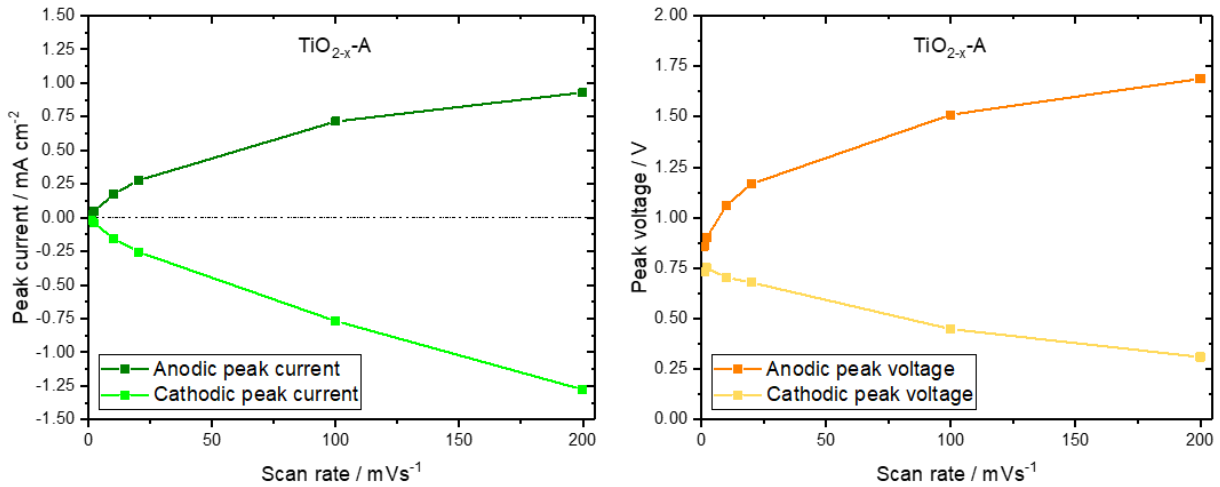
Figure 25.: Peak currents with respect to the scan rate between 200 mV s$^{-1}$ to 1 mV s$^{-1}$ of TiO$_{2-x}$-A for the aged sample, and b) Peak voltage with respect to the scan rate between 200 mV s$^{-1}$ to 1 mV s$^{-1}$ of TiO$_{2-x}$-A for the aged sample.

### 4.5.2. TiO$_2$-M

CVs with different scan rates from 200 mV s$^{-1}$ to 0.1 mV s$^{-1}$ were also carried out on the TiO$_2$-M electrodes and the initial CVs were compared in one graph to see the difference in the shape of the curve with changing scan rates, depicted in Figure 26.
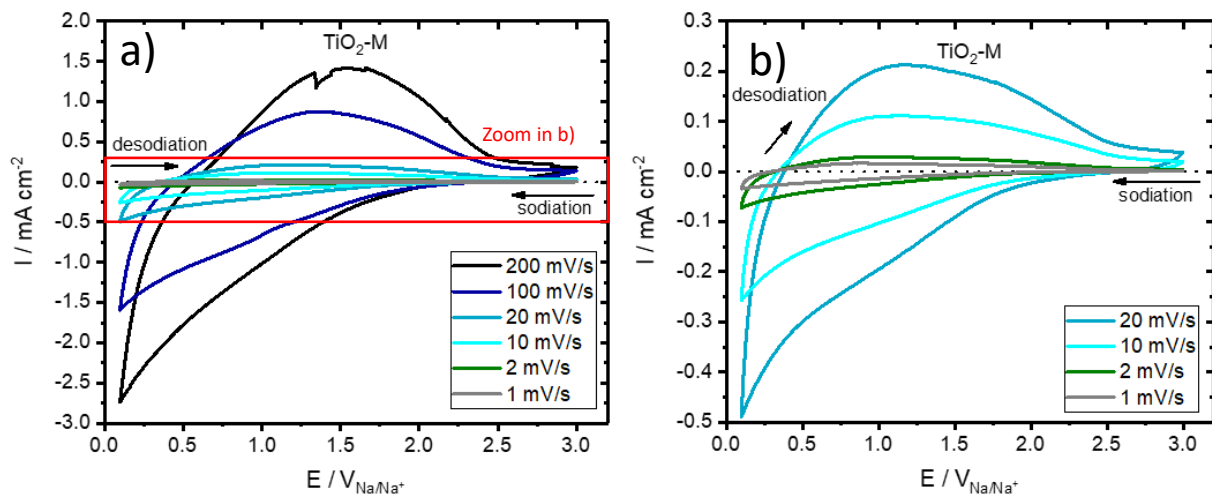


Figure 26.: CV of initial TiO$_2$-M at different scan rates from a) 200 mV s$^{-1}$ down to 1 mV s$^{-1}$ and zoomed from b) 20 mV s$^{-1}$ down to 1 mV s$^{-1}$.

The prominent peak at 0.1 V is again attributed to electrolyte decomposition together with the formation of a surface film.[8,71] The peak currents of the 200 mV s$^{-1}$ scan for example amount 1.54 V and -2.74 V, which is significantly bigger compared to the peak currents of the 200 mV s$^{-1}$ scans of TiO$_{2-x}$-A (0.93 V/-1.27 V) and MoO$_{2+x}$ (0.51 V/-0.91 V).

### 4.5.3. MoO$_{2+x}$

CVs with different scan rates from 200 mV s$^{-1}$ to 0.1 mV s$^{-1}$ were carried out on the MoO$_{2+x}$ electrodes and the initial CVs were compared in one graph to see the difference in the shape of the curve with changing scan rates, depicted in Figure 27.
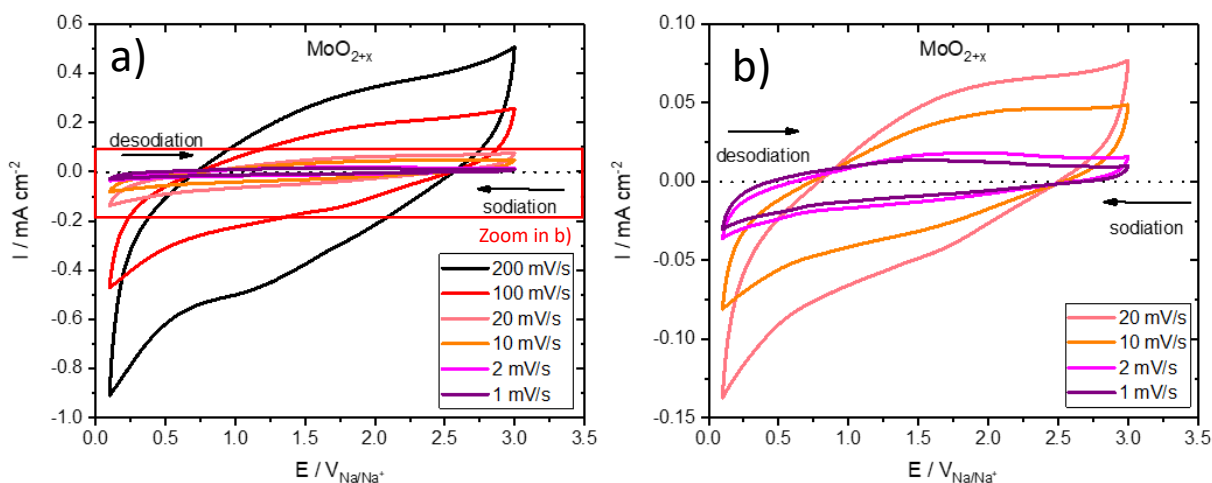


Figure 27.: CV of initial MoO$_{2+x}$ at different scan rates from a) 200 mV s$^{-1}$ to 1 mV s$^{-1}$, and b) detailed view of CVs with slow scan rate from 20 mV s$^{-1}$ to 1 mV s$^{-1}$.

As observed with the TiO$_{2-x}$-A initial CVs, also all initial CVs of the MoO$_{2+x}$ show a similar behaviour. The cathodic current starts decreasing at 2.5 V until 1.0 V. From this point on, the slope becomes steeper until a vertex potential of 0.1 V is reached. The observed reductive current is attributed to electrolyte decomposition together with surface film formation. As already mentioned in the description of the CVs of the TiO$_{2-x}$-A, this formation of a surface film may be explained by the reduction of solvent molecules and anions present in the electrolyte.

Otherwise, no distinct cathodic or anodic peaks can be seen.
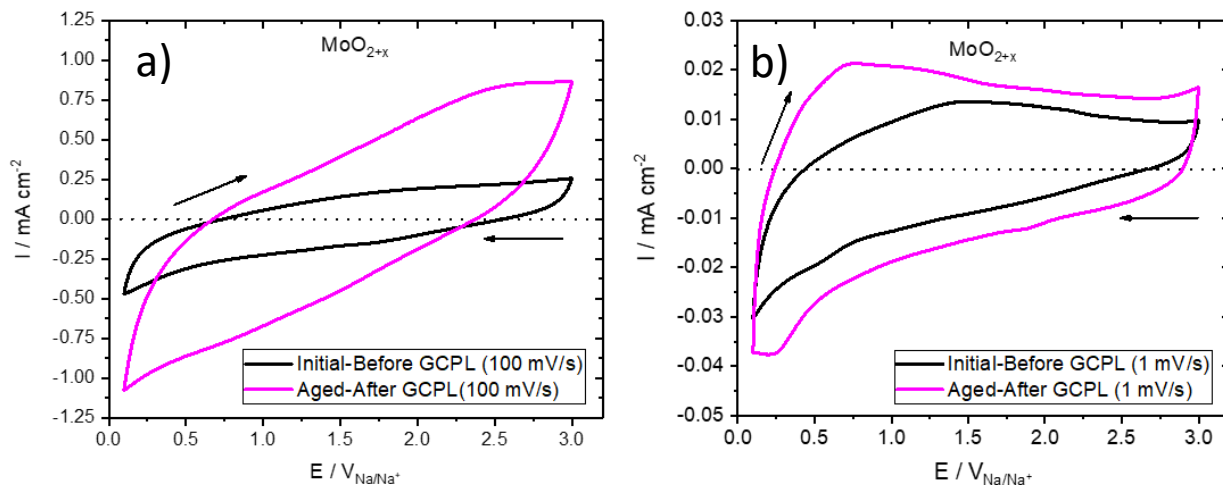
Figure 28.: CV of MoO$_{2+x}$ for the initial and aged sample between 3.0 and 0.1 V for the scan rate of a) 100 mV s$^{-1}$ and b) 1 mV s$^{-1}$.

The comparison between the initial CV before the GCPL measurements and the aged CV after the GCPL measurements, for 100 mV s$^{-1}$ and 1 mV s$^{-1}$, can be seen in Figure 28.

Between 2.0 V and 0.5 V the storage of the sodium in the MoO$_2$ layer could take place as described in the following equation:[76]

$$MoO_2 + xNa^+ + xe^- \rightleftharpoons Na_xMoO_2 \qquad (4.5.3.1)$$
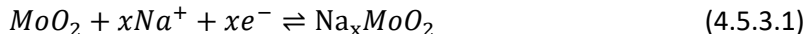
When the voltage approaches a value of 0.1, it could be expected, that Na$_x$MoO$_2$ and residual MoO$_2$ convert into metallic Mo and Na$_2$O, as described in the equations (4.5.3.2) and (4.5.3.3):[76]

$$Na_xMoO_2 \rightleftharpoons Mo^0 + \frac{x}{2}Na_2O \qquad (4.5.3.2)$$

$$MoO_2 + 4Na^+ + 4e^- \rightleftharpoons Mo^0 + 2Na_2O \qquad (4.5.3.3)$$
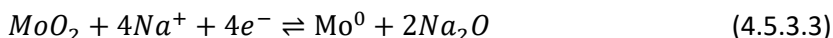
The reverse reaction of the Na$_2$O and the metallic Mo back to the Na$_x$MoO$_2$ takes place between 0.1 V and 1.5 V, which could cause the formation of an anodic peak. Thus, the redox pair located at around 0.2 V and 0.72 V could be attributed to the reversible Na ion storage in MoO$_2$.[76] The formation of the anodic peak could also be caused by the deposition of the sodium in the surface film, as already described in chapter 2.3. However, the post mortem XPS analysis of the aged MoO$_{2+x}$ shown in 4.9.2

will provide further information about the mechanism of sodium storage by looking at the composition of the surface film.

The CVs at higher scan rate (100 mV s$^{-1}$) show a different behaviour compared to those with lower scan rate as illustrated in Figure 28 a). No definite cathodic or anodic peak can be identified. This behaviour relates to the pseudocapacitive performance of the MoO$_{2-x}$, which in contrast to the diffusion-controlled reaction, the charged molecule does not bond in the bulk but adsorbs on the surface. Investigations of Jiang et al. show that the compulsory reversible reaction between MoO$_2$ and metallic Mo below 0.5 V only takes place at scan rates below 0.5 mV s$^{-1}$. At higher rates the reaction is too slow to follow the voltage change and the peaks vanish as can be seen in Figure 28 a) between 1.5 V and 0.1 V.[76]

The comparison of the aged CVs, as it was made for the TiO$_{2-x}$-A depicted in Figure 24, was not carried out here, since both the anodic and the cathodic peaks are not sufficiently pronounced to determine a clear course of the distance between the both peaks.

## 4.6.    Galvanostatic cycling with potential limitation

Since long-term stability is one of the essential criteria of a battery, galvanostatic cycling with potential limitation (GCPL) was performed in the voltage range of 0.1 to 3 V at seven different C-rates, starting with 1.606 C (117 mA), down to 0.016 C (1.2 mA). For all samples, $TiO_{2-x}$-A, $MoO_{2+x}$ and $TiO_2$-M, the same C-rates were used (see chapter 3.5) for a better comparison. These measurements are particularly important, because of the long-term stability characterization, which is significantly affected due to the supposedly slower intercalation of Na ions into the host material compared to the smaller Li ions. Additionally, the often associated side reactions between electrolyte and active material that often occur during the insertion process, influence the long-term stability.[8] The specific capacities in the figures in the chapters 4.6.1 to 4.6.3 are related to the area of the electrode. The analogous graphs with respect to the active mass are shown in the appendix in chapter 10.8. The closed squares in the following Figures of the specific capacity with respect to the cycle number are mostly located behind the open squares which makes them difficult to see.

### 4.6.1. $TiO_{2-x}$-A

Figure 29 displays the different charge-discharge curves of $TiO_{2-x}$-A where the respective voltage is plotted against the specific capacitance (Figure 29 a)), and the specific capacitance is plotted against the cycle numbers (Figure 29 b)), respectively.

It can be seen in Figure 29 a) that the capacity increases with decreasing current, from 3.5 µAh cm$^{-2}$ (37 µAh g$^{-1}$) at a constant current of 117 µA to about 10 µAh cm$^{-2}$ (107 µAh g$^{-1}$) at a constant current of 1.2 µA. What all curves have in common, independent of the chosen current, is the steady slope between 1.5 V and 0.1 V, where the largest increase of the specific capacity occurs.[8]

An indication of high reversibility is the intersection of the related sodiation/desodiation curve. Here, the average centre is located at 1 V at a current of 117 µA and drops to a value of 0.9 V at a current of 1.2 µA.[8]
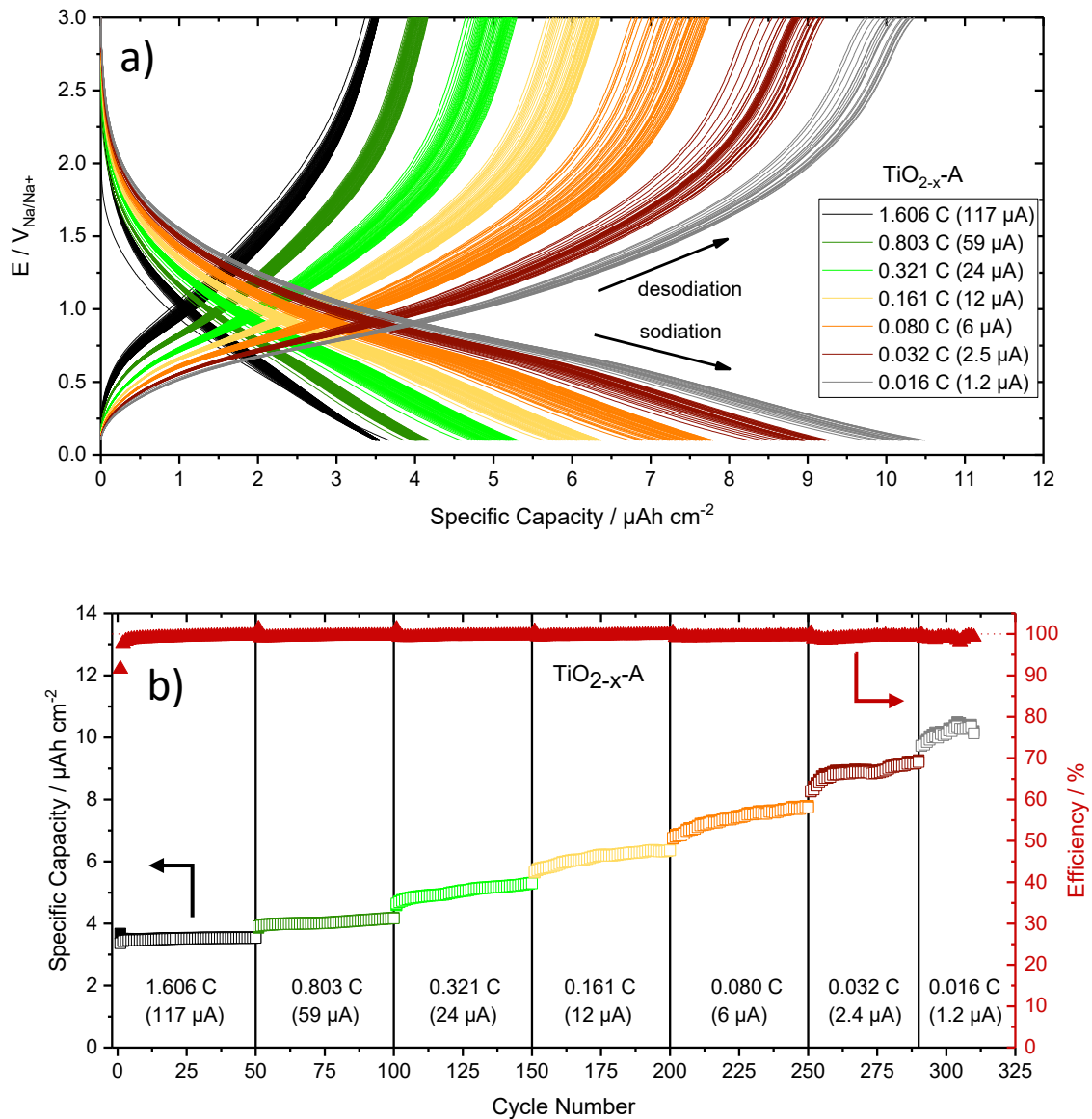
Figure 29.: GCPL curves of TiO$_{2-x}$-A normalized to the surface area a), and b) the specific capacity with respect to the cycle number and corresponding Coulombic efficiencies (red triangles). Closed squares relate to discharge (sodiation) and open squares to charge (desodiation) capacities.

Interestingly, an increase of the specific capacity is not only observed at decreasing C-rates, common to almost all battery electrode materials, but also within a given C-rate. It is remarkable that the specific capacity, especially at low C-rates below 0.321 C, improves continuously with the cycle number, as it can be seen in Figure 29 b). This phenomenon of an self-improvement effect was already detected in earlier investigations of our group by Portenkirchner et al.[8] Three regions demonstrate

different curve progressions. At high currents of 117 µA (1.606 C) and 59 µA (0.803 C), the self-improvement can be detected, since the increase of the capacity totals 0.19 µAh cm$^{-2}$ (1.96 mAh g$^{-1}$) over 50 cycles at 1.606 C and 0.26 µAh cm$^{-2}$ (2.67 mAh g$^{-1}$) over 50 cycles at 0.803 C. Between 0.321 C and 0.080 C, the strongest increase can be detected, with a capacity increase of 0.65 µAh cm$^{-2}$ (6.83 mAh g$^{-1}$) over 50 cycles at a current of 24 µA, 0.68 µAh cm$^{-2}$ (7.15 mAh g$^{-1}$) over 50 cycles at a current of 12 µA, and 0.98 µAh cm$^{-2}$ (10.28 mAh g$^{-1}$) over 50 cycles at a current of 6 µA, respectively. The improvement between 24 µA and 6 µA takes place in an approximately linear form, which is unlike the third region, in which a flattening after a first progressive increase occurs. The total improvement equals 0.94 µAh cm$^{-2}$ (9.84 mAh g$^{-1}$) over 40 cycles at a current of 2.4 µA, and 0.40 µAh cm$^{-2}$ (6.54 mAh g$^{-1}$) over 20 cycles at a current of 1.2 µA. The specific capacitance finally flattens out to 10.3 µAh cm$^{-2}$ (108.30 mAh g$^{-1}$) after 310 cycles at a C-rate of 1.2 mA. Since the cycle number was only 40 cycles at 2.4 µA and 20 cycles at 1.2 µA, the long-term development of the specific capacity at these low C-rates may not be fully resolved. None the less, a distinctive self-improvement effect, as reported by Portenkirchner et al. can be seen for TiO$_{2-x}$-A.[8]

The Coulombic efficiency amounts 91.56 % for the first cycle, increasing to 99.01 % for the 13$^{th}$ cycle and stays above this value for the rest of the GCPL measurements. Exceptions are the measurements at lower speeds, namely 2.4 µA and 1.2 µA, with unstable efficiencies between 98.5 and 99.5 %.

## 4.6.2. TiO$_2$-M

Several sodiation/desodiation curves of TiO$_2$-M at different applied currents ranging from 117 µA to 2.4 µA are displayed in Figure 30 a). Additionally, the specific areal capacitance is plotted over the cycle number (Figure 30 b)). Due to time issues, only nine cycles at a current of 2.4 µA and no cycles at 1.2 µA were recorded.

An increasing capacity with decreasing applied current can be observed for the TiO$_2$-M electrode, as was also the case with TiO$_{2-x}$-A. The capacity increases from 5.8 µAh cm$^{-2}$ (61 mAh g$^{-1}$, based solely on the mass fraction of the TiO$_2$-layer), at a constant current of 117 µA, to about 16.8 µAh cm$^{-2}$ (177 mAh g$^{-1}$) at a constant current of 2.4 µA. The sodiation/desodiation characteristics of TiO$_{2-x}$-M are characterized by a sloping voltage response upon applied current between 0.5 V and 1.7 V, where the largest increase of the specific capacity occurs. For the TiO$_2$-M, the intersection point of the sodiation and the desodiation curve is located at 1.25 V at a current of 117 µA and slightly drops to a value of 1.2 V at a current of 1.2 µA.[8]
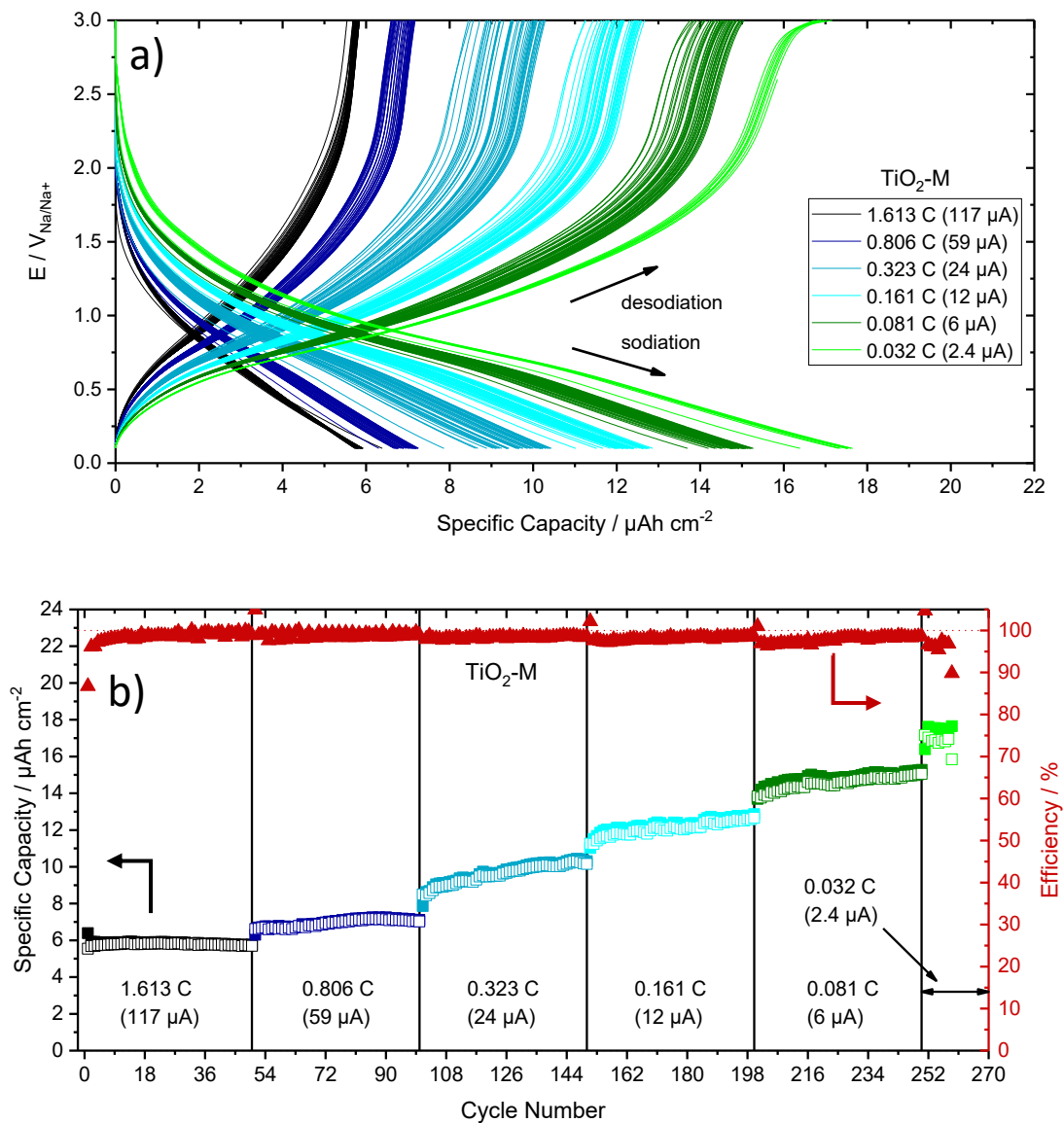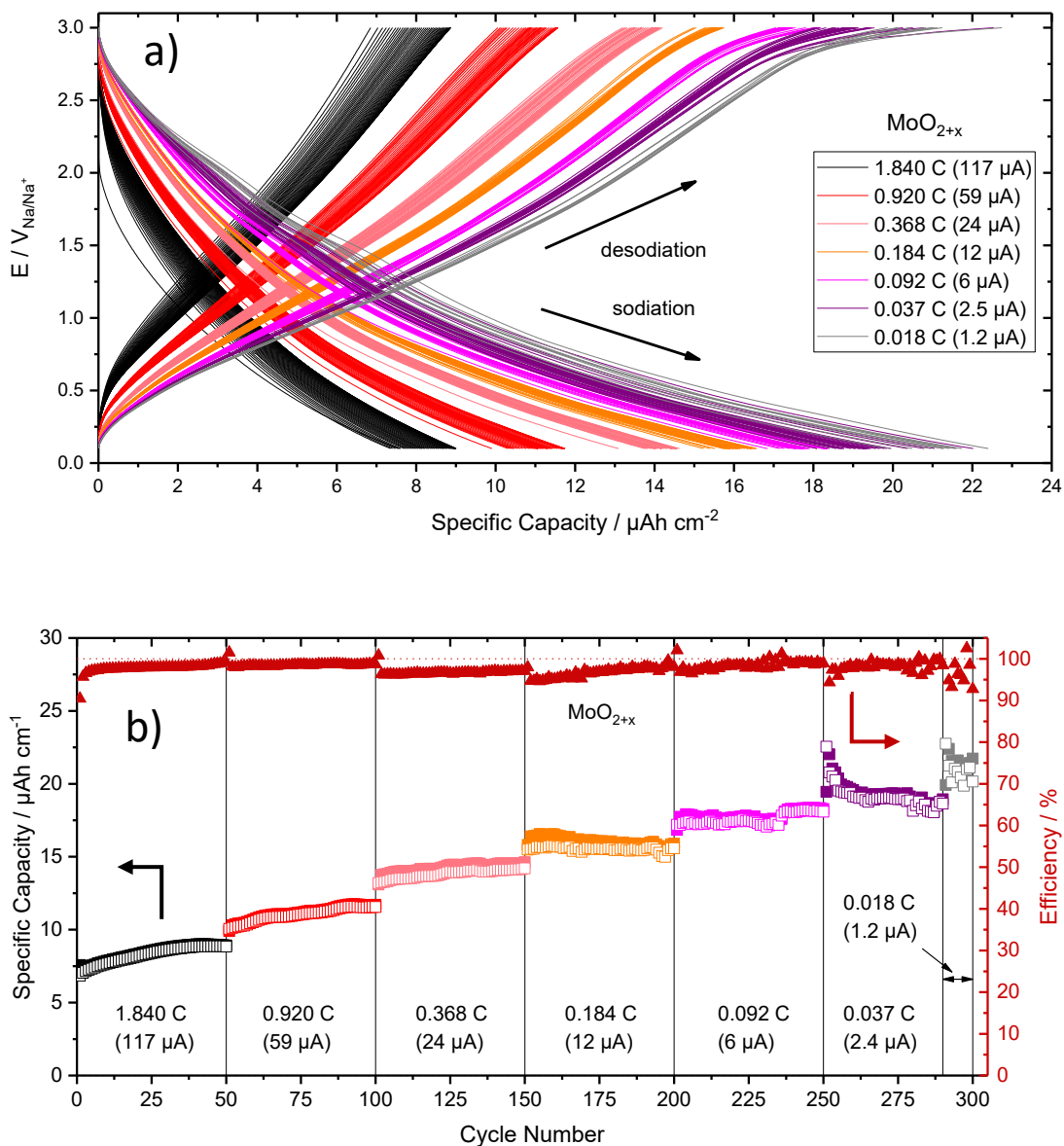
Figure 30.: GCPL curves of TiO$_2$-M normalized to the surface area a) voltage with respect to the specific capacity, and b) the specific capacity with respect to the cycle number and corresponding Coulombic efficiencies (red triangles). Closed squares relate to discharge (sodiation) and open squares to charge (desodiation) capacities.

As it can be seen for the TiO$_{2-x}$-A electrode, an increase of the specific capacity within a given C-rate can be detected (Figure 30 b)). At high currents of 117 µA (1.61 C), and 59 µA (0.81 C), the self-improvement effect is weakly pronounced, since the total increase of the specific capacity amounts to 0.08 µAh cm$^{-2}$ (2.35 mAh g$^{-1}$) over 50 cycles at 1.61 C and 0.42 µAh cm$^{-2}$ (4.30 mAh g$^{-1}$) over 50 cycles at 0.81 C. Between 0.32 C and 0.08 C, the strongest increase of the capacity takes place with

1.66 μAh cm$^{-2}$ (17.85 mAh g$^{-1}$) over 50 cycles at a current of 24 μA, 1.42 μAh cm$^{-2}$ (14.89 mAh g$^{-1}$) over 50 cycles at a current of 12 μA and 1.30 μAh cm$^{-2}$ (12.81 mAh g$^{-1}$) over 50 cycles at a current of 6 μA, respectively. At a C-rate of 0.03 C (2.4 μA), the specific capacity finally decreases by 0.2 μAh cm$^{-2}$ (2.08 mAh g$^{-1}$) over 9 cycles. It seems that the specific capacity is already decreasing at this current, indicating that the self-improvement effect is already finished. Unfortunately, the results were evaluated prematurely for reasons of time, but the test cells are still running and will be evaluated in the future. However, the distinctive self-improvement effect, as reported from Portenkirchner et al. can also be seen for the TiO$_2$-M electrodes.[8]

The Coulombic efficiency amounts to 86.72 % for the first cycle, is increasing to 97.89 % for the 15th cycle, and stays above this value until the end of the measurements with C-rates of 0.161 C. For C-rates of 0.081 C and lower, the Coulombic efficiency is between 89.81 and 98.39 %.

### 4.6.3. MoO$_{2+x}$

Figure 31 shows the different charge-discharge curves of MoO$_{2+x}$. In Figure 31 a), the respective voltage is plotted against the specific capacitance. The specific capacity is increasing with decreasing current, from 8 μAh cm$^{-2}$ (60 mAh g$^{-1}$) at a constant current of 117 μA, to about 22 μAh cm$^{-2}$ (155 mAh g$^{-1}$) at a constant current of 1.2 μA. The specific capacity is, compared to the values of the TiO$_{2-x}$-A depicted in Figure 29 a), about two times higher. Unlike the TiO$_{2-x}$-A, there is no steady slope between 1.5 V and 0.1 V, where the largest increase of the specific capacity occurs (Figure 29 a)), but the growth of the specific capacity increases slightly during the sodiation and is fairly constant during the desodiation. An indication of high reversibility is the intersection of the related sodiation/desodiation curve. Here, the average centre is located at 1.25 V at a current of 117 μA and slightly drops to a value of 1.2 V at a current of 1.2 μA.[8]

Figure 31.: GCPL curves of MoO$_{2+x}$ normalized to the surface area a), voltage with respect to the specific capacity and b) the specific capacity with respect to the cycle number and corresponding Coulombic efficiencies (red triangles). Closed squares relate to discharge (sodiation) and open squares to charge (desodiation) capacities.

As it can be seen for the TiO$_{2-x}$-A and the TiO$_2$-Melectrodes depicted in Figure 29 b) and Figure 30 b), an increase of the specific capacity is not only observed at decreasing C-rates, but also within a given C-rate (Figure 31 b)). Again, the specific capacity, especially at low C-rates below 0.184 C, improves continuously with the cycle number. At high currents of 117 µA (1.840 C), and 59 µA (0.920 C) and 24 µA (0.368 C), the self-improvement can be detected, since the increase of the specific capacity totals

2.07 µAh cm$^{-2}$ (15.25 mAh g$^{-1}$) over 50 cycles at 1.840 C, 1.65 µAh cm$^{-2}$ (12.15 mAh g$^{-1}$) over 50 cycles at 0.920 C, and 1.01 µAh cm$^{-2}$ (7.01 mAh g$^{-1}$) over 50 cycles at 0.368 C. Between 0.184 C and 0.092 C, the capacity remains approximately constant with a capacity increase of 0.1 µAh cm$^{-2}$ (0.74 mAh g$^{-1}$) over 50 cycles at a current of 12 µA, 0.89 µAh cm$^{-2}$ (6.58 mAh g$^{-1}$) over 50 cycles at a current of 12 µA, respectively. At a C-rate of 0.037 C, the specific capacity is finally decreasing, amounting 3.40 µAh cm$^{-2}$ (28.68 mAh g$^{-1}$) over 40 cycles at a current of 2.4 µA. The values at a C-rate of 0.018 C over 20 cycles at a current of 1.2 µA are very volatile and cannot be assigned to any course. The distinctive self-improvement effect, as reported from Portenkirchner et.at. can also be seen for $MoO_{2+x}$ electrodes but only for high currents.[8] The Coulombic efficiency amounts 90.44 % for the first cycle, increasing to 97.71 % for the 15$^{th}$ cycle, and stays above this value for C-rates of 1.840 C and 0.920 C. For C-rates higher 0.920 C the Coulombic efficiency is located between 92.7 and 99.7 %.

## 4.7. SPEIS

To understand the electrochemical processes within the $TiO_{2-x}$-A test cell, two types of electrochemical impedance spectroscopy were performed. On the one hand, measurements with open cell voltage (OCV) were carried out before and after the CV and the GCPL measurements to reflect the behaviour of the cell after long-term cycling, described in chapter 4.4. On the other hand, measurements with a staircase dependent voltage change from 3 V down to 0.1 V were done. This means that the voltage is set to a constant value between 3 V and 0.1 V, and the whole frequency spectrum from 10 kHz to 5 mHz as for the PEIS measurements (chapter 4.4) is run through.

### 4.7.1. $TiO_{2-x}$-A

Figure 32 shows the scheme of the $TiO_{2-x}$-A test cell with the corresponding equivalent circuit used for fitting the impedance response including components, which represents various processes within the $TiO_{2-x}$-A cell.[77]
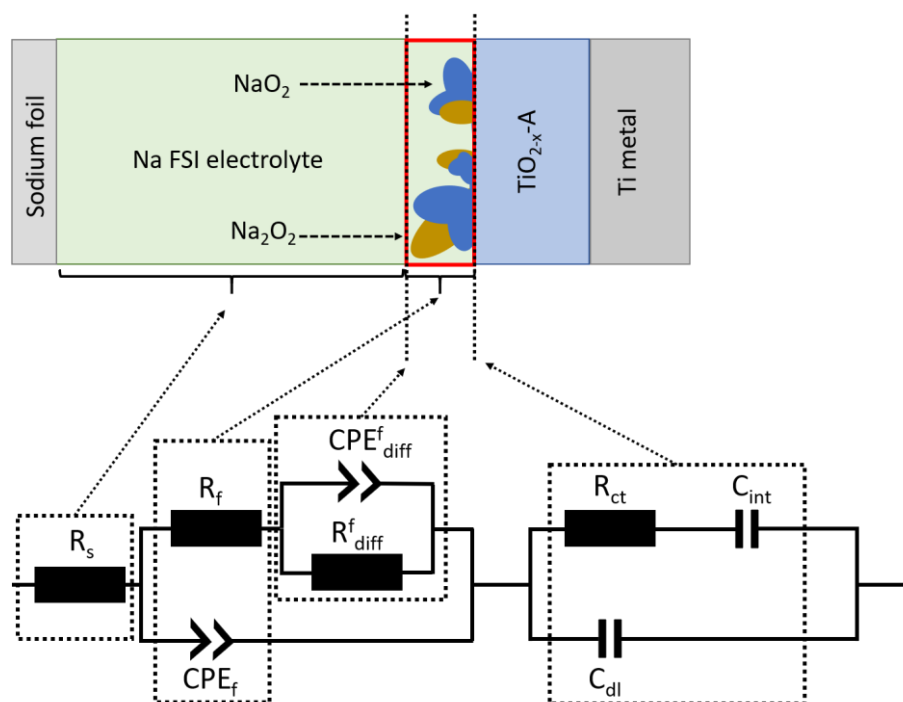


Figure 32.: Scheme of the ECC-Ref test cell with $TiO_{2-x}$-A electrode and 1 M Na FSI electrolyte during sodiation/desodiation with the corresponding equivalent circuit for SPEIS data fitting inspired from reference [78].

The resistor $R_S$, which shifts the whole spectrum by a positive real component along the x-axis, represents the ionic resistance of the electrolyte and the contact resistances of the cell.[70,79,80] The next part of the equivalent circuit is a combination of the resistor $R_f$ and a constant phase element $CPE_f$, which represents the surface film resistance and the corresponding capacitance. The parallel connection between the resistor $R^f_{diff}$ and the constant phase element $CPE^f_{diff}$ describes the diffusion resistance and the diffusion capacitance in the $TiO_{2-x}$-A surface film .[44,77]

The last elements of the circuit are the charge transfer resistance $R_{ct}$, the double layer capacitance $C_{dl}$ and the low-frequency internal chemical capacitance $C_{int}$.

The equivalent circuit does not include a Warburg element or a modified restricted diffusion element, representing a non-ideal Warburg element, where at lower frequencies a straight line with a phase angle not equal to 45° is formed, instead of a straight line with an angle of 45°. These elements would describe $Na^+$ diffusion into the $TiO_{2-x}$-A electrode, which is excluded, since it is assumed that diffusion only occurs in the surface as reported by Portenkirchner et al.[8]

The closed squares in Figure 33, Figure 34 and Figure 35 are related to the discharge process and the open squares are related to the charge process.
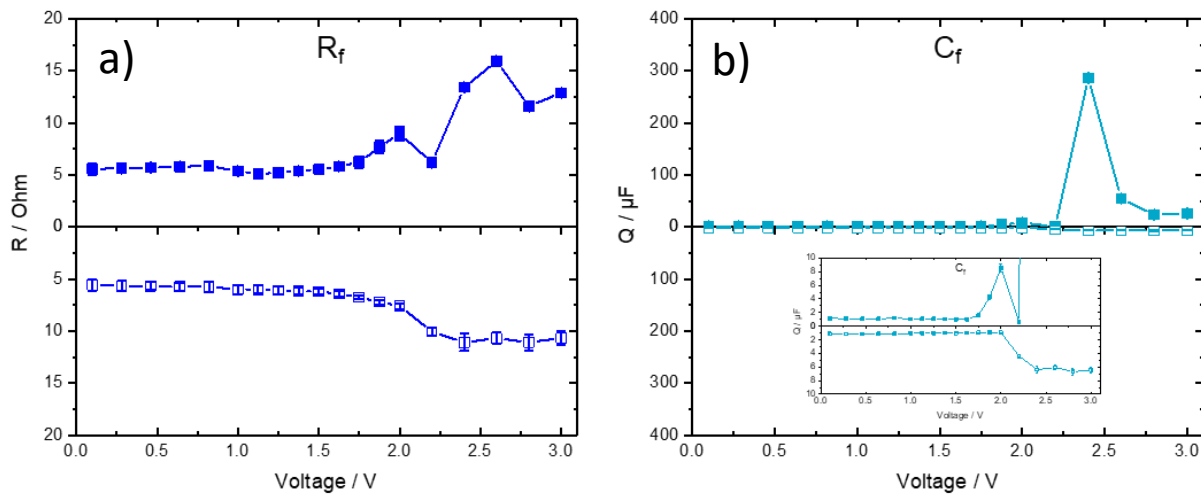


Figure 33.: a) Surface film resistance, and b) surface film capacitance of the ECC-Ref test cell with $TiO_{2-x}$-A electrode. The closed squares are related to the discharging process and the open squares are related to the following charging process.

The film resistance $R_f$ and the corresponding capacitance $C_f$ are shown in Figure 33 a) and b), respectively. Stable values between 5 Ω and 15 Ω are recorded for the film resistance depicted in Figure 33 a). The values are almost constant for potentials between 0.1 V and 2 V and higher for potentials

between 2 V and 3 V. The corresponding capacitance $C_f$ depicted in Figure 33 b) shows a similar behaviour as the film resistance. Between 0.1 V and 1.6 V, the capacitance stays nearly constant at 1.1 µF for the discharging and charging process. During the discharge process between 3 V and 2.6 V, capacitance values ranging from 25 µF to 54 µF are found and a very distinct peak at 2.4 V appears at 287 µF. This peak cannot be precisely assigned at the moment and requires further investigation. During the charging process between 2 V and 3 V the capacity values between 4 µF and 6.4 µF are recorded.

The diffusion resistance $R^f_{diff}$ and the diffusion capacitance $C^f_{diff}$ are shown in Figure 34 a) and b), respectively.
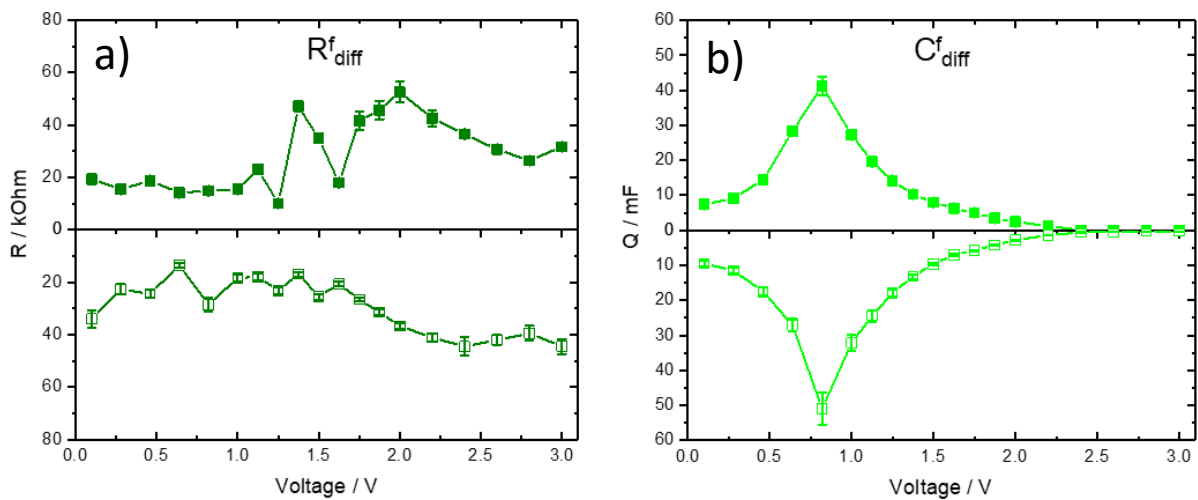


Figure 34.: a) Diffusion resistance, and b) diffusion capacitance of the ECC-Ref test cell with TiO$_{2-x}$-A electrode. The closed squares are related to the discharging process and the open squares are related to the following charging process.

The Na storage can, beside $R_f$ and $C_f$, be assigned to a major part to these two components. The values of the diffusion resistance $R^f_{diff}$ shown in Figure 34 a) amount between 26 kΩ and 52 kΩ for voltages ranging from 3 V to 2 V and then decrease to values between 10 kΩ and 33 kΩ for the remaining voltage steps for both, charging an discharging process.

The diffusion capacitance shows an inverse trend of the curve compared to the diffusion resistance. Between 3 V and 2 V, the capacitance values are ranging from 4 µF to 2.5 mF. Then the values continuously increase until a maximum at 0.82 V is reached with a capacity of 41 mF for the discharging process and 51 mF for the charging process, respectively. After the maximum, the values are decreasing again to 7.4 mF for discharging process and 9.5 mF for charging process. The distinct peaks at 0.82 V are related to the Na storage process in the surface film and correlate with the peaks in the

CV of $TiO_{2-x}$-A with a scan rate of 1 mV/s shown in Figure 23. The peaks in the CV can be located at 0.74 V for the discharging process and 0.84 V for the charging process.

The solution resistance $R_s$ and the charge transfer resistance $R_{ct}$ (Figure 35 a) and b)) show stable values between 5 Ω and values in the region of pΩ. Both spectra show a rather random and therefore not representative course of the curve, which could not provide information about the processes in the cell.
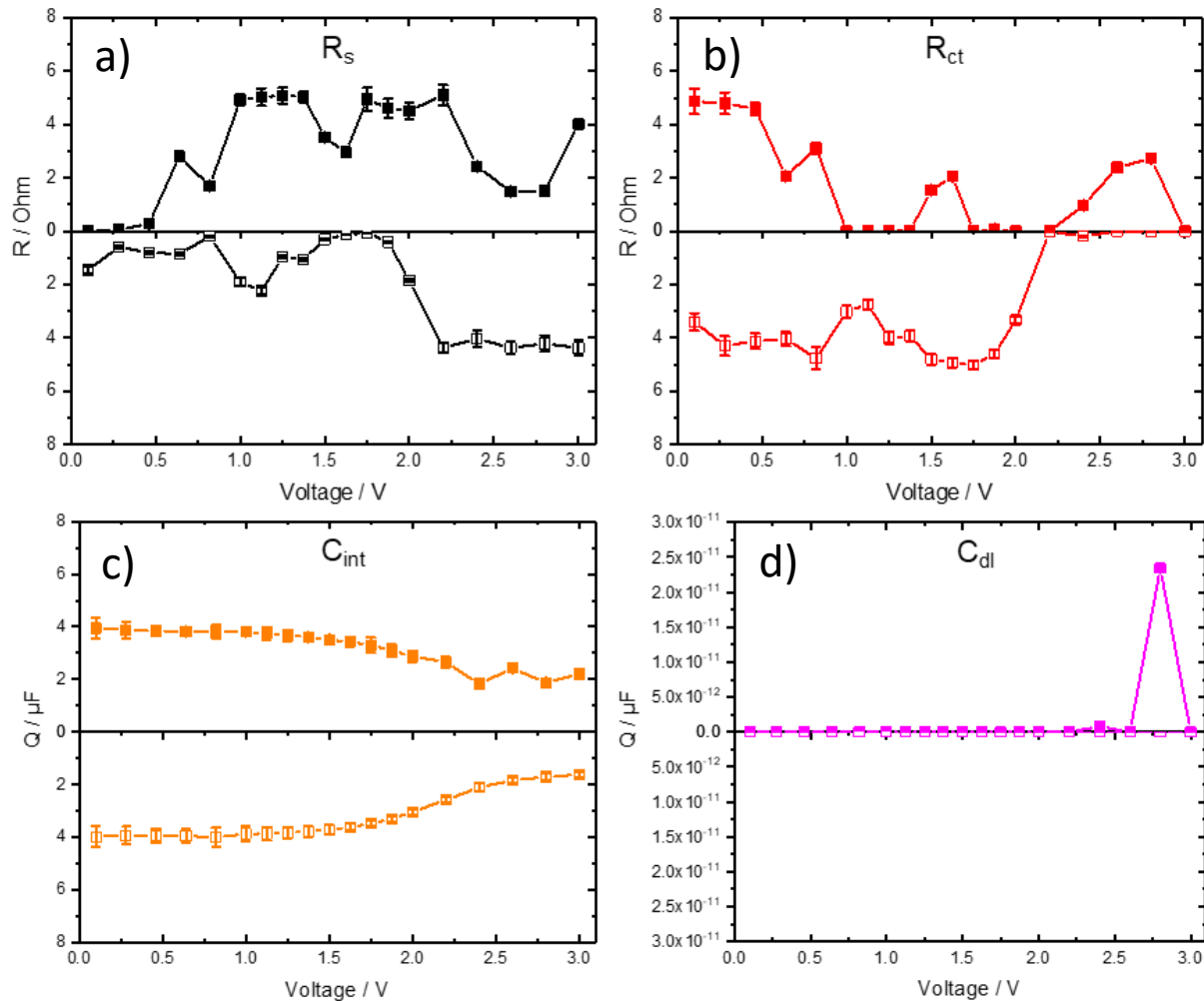


Figure 35.: a) Ionic resistance of the electrolyte and the contact resistances of the cell, b) low-frequency internal chemical capacitance, c) charge transfer resistance, and d) double layer capacitance of the ECC-Ref test cell with $TiO_{2-x}$-A electrode. The closed squares are related to the discharging process and the open squares are related to the following charging process.

Figure 35 c) depicts the low-frequency internal chemical capacitance $C_{int}$ with stable values between 4 µF and 1.8µF, where the values between 3 V and 2.4 V for the charge and discharge process are

around 1.8 µF, and for voltages under 2.4 V the capacity increases to around 4 µF. The capacitance $C_{int}$ is probably attributed to bulk diffusion of the Na in the electrode. Since the Na ions are relatively large, compared to Li ions, the diffusion probably takes place only in the uppermost atomic layers, because the following ions are blocked by ions that are already intercalated. Borghols et al. investigated the intercalation of Li in $TiO_2$ and found out that the intercalation depth possesses a maximum value of 7 nm and it seems to be independent of the total size of the $TiO_2$ particle, because the $LiTiO_2$ acts as an impenetrable barrier for further insertion of Li.[81] Thus, for this thesis, an equally minimal intercalation can be assumed.

The double layer capacitance $C_{dl}$ is shown in Figure 35 d). The small surface area (2.84 $cm^2$) of the flat electrodes, compared to $TiO_2$ anatase nanotubes investigated by Auer with surface areas of 136 $cm^2$, is most likely responsible for the very low capacitance values under $10^{-11}$ µF.[44]

## 4.7.2. MoO$_{2+x}$

The evaluation of the SPEIS data of $MoO_{2+x}$ is not part of this thesis because on the one hand the oxide layer is even more inhomogeneous than the $TiO_{2-x}$-A layer (see SEM pictures in chapter 4.9.2) and on the other hand the fitting process was no longer feasible due to time constraints.

## 4.8.    Post mortem XPS analysis

After long-term GCPL, post mortem analysis of the $TiO_{2-x}$-A and $MoO_{2+x}$ surfaces were performed to investigate the composition of the surface film, which, for the former part, consists of an XPS analysis. Therefore, specially prepared test cells, as described in chapter 3.3, were used.

In Table 6, the XPS peak kinetic energies of all components presumed at the surfaces of the WE are listed. The fits were done with the software CasaXPS, as was also the case in chapter 4.2. For the necessary calibration of the spectra, which was performed before the fitting, the Na 1s peak was set to 1071.4 eV, because the peak is sharp and its full width at half maximum (FWHM) is small compared to the FWHMs of the other components. In addition to the surface measurements, depth profiles were made to check the composition inside the surface film.

Table 6.: XPS peak kinetic energies of all surface film components of $TiO_{2-x}$-A and $MoO_{2+x}$.

| $TiO_{2-x}$-A | Peak [eV] | FWHM [eV] | Peak [eV] | FWHM [eV] | Reference |
|---|---|---|---|---|---|
| | Ti 2p$_{3/2}$ | | Ti 2p$_{1/2}$ | | |
| Ti(IV)-oxide | 458.59 ± 0.00 | 1.04 | + 5.72 | 1.98 | [66] |
| Ti(III)-oxide | 457.30 ± 0.70 | | +5.20 | | [67] |
| Ti(II)-oxide | 455.50 ± 0.60 | | +5.60 | | [67] |
| Ti(0) | 453.74 ± 0.02 | 0.69 | +6.05 | 0.83 | [66] |
| O 1s | | | | | |
| $Na_2O_2$ | 530.90± 0.00 | 1.10 | | | [82] |
| $Na_2O$ | 529.70 ±0.00 | | | | [83] |
| $Na_2CO_3$ | 531.30 ± 0.30 | 2.11 | | | [84] |
| C=O* | 531.80 ± 0.40 | | | | [85] |
| C 1s | | | | | |
| C-C, C-H | 285.00± 0.00 | 0.6-0.8 | | | [86] |
| C-O-C* | 286.50 ± 0.20 | 0.6-1.2 | | | [86] |
| $CO_3^{2-}$ | 289.30 ± 0.6 | | | | [86] |
| Na 1s | | | | | |
| Na | 1071.40 ± 0.5 | | | | [87] |
| Na Auger | 536.00 ± 1.00 | | | | [88] |
| $MoO_{2+x}$ | Peak [eV] | FWHM [eV] | Peak [eV] | FWHM [eV] | Reference |
| | Mo 3d$_{5/2}$ | | Mo 3d$_{3/2}$ | | |
| Mo(IV)-oxide | 229.70 ± 0.9 | | +3.15 | | [67] |
| Mo(VI)-oxide | 233.15 ± 0.20 | 0.86 | +3.15 | 0.9 | [67]‡ |
| Mo(V)-oxide | 231.75 ± 0.15 | | | | [68] |
| O 1s | | | | | |
| Lattice IV | 530.50 ± 0.50 | | | | [67] |
| Lattice VI | 530.60 ± 0.40 | | | | [67] |
| $H_2O$ | 534.40 ± 1.80 | | | | [69] |

*Adventitious carbon, ‡shift C1s to 284.8

## 4.8.1. TiO$_{2-x}$-A

The measurement comprises seven different spectra, beginning with a survey and continuing with high resolution measurements of S 2p, C 1s, N 1s, Ti 2p, O 1s and Na 1s. The four most informative spectra are the O 1s and the C 1s depicted in Figure 37 a) and b) and Figure 38 a) and b), because in these spectra the difference in the composition of several compounds, especially the oxides and carbonates on the surface, to those within the surface film can be compared. For better comparability, the O 1s and the Ti 2p spectra of the initial TiO$_{2-x}$-A are depicted in Figure 36 a) and b), respectively.
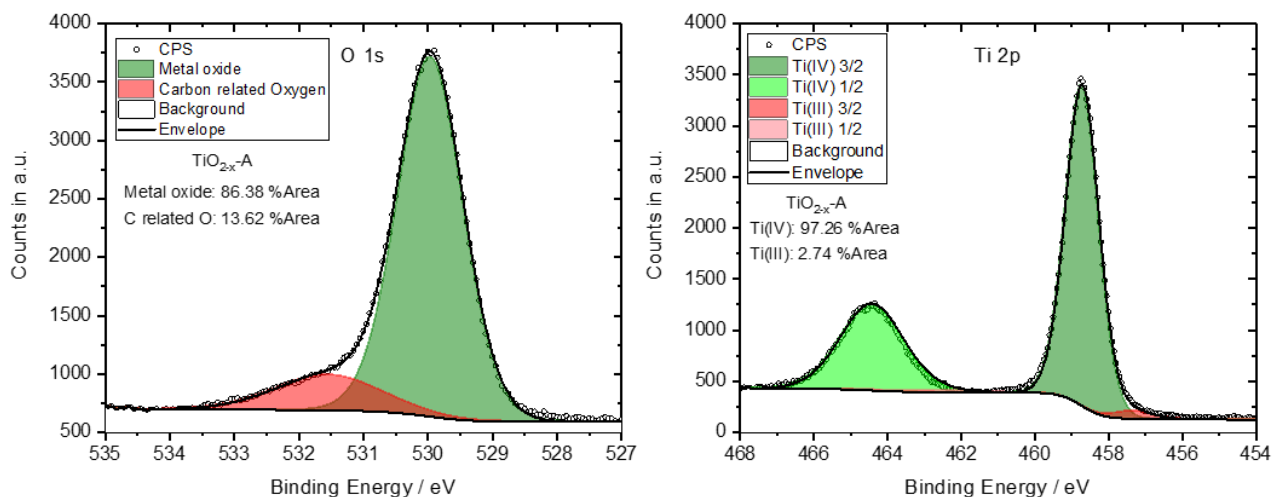
Figure 36.: a) O 1s spectra and b) Ti 2p spectra of TiO$_{2-x}$-A including relative mass distribution of the initial sample.

The O 1s spectra of the surface, and after 20 seconds of argon sputtering, can be seen Figure 37 a) and Figure 37 b), respectively. At about 529.5 eV a weak signal of Na-O (Figure 37 a) and b) dark green) is visible, which corresponds to Na$_2$O$_2$ and Na$_2$O, respectively. The area percentage of the Na-O peak decreases from 4.87% to 4.17% approximately (all following percentages are also area percentages). Whether all sodium oxides are present, the exact ratio of the oxides to each other can hardly be determined, due to the similar peak positions of 530.9 eV for the Na$_2$O$_2$ and 529.7 eV for the Na$_2$O. The peak at 531.4 eV (Figure 37 a) and b) light green) represents carbonate species, including Na$_2$CO$_3$, which is presumably a main component of the surface film. The area remains approximately stable and increases slightly from 65.47% to 65.95%. This is indicative that not only carbonates that were formed by adsorbed adventitious carbon are present, but also carbonates from decomposition of the electrolyte. This circumstance is corroborated by the fact that the adventitious carbon peak (Figure

37 a) and b) light red), measured at 533.3 eV, decreases from 11.16% to 4.53%. The Na Auger peak at 535.8 eV increases from 18.50% to 25.92%, due to Na that is incorporated in the surface film during cycling. It should be noted that O from the $TiO_{2-x}$-A bulk was not considered during fitting of the O 1s peak, because the proportion is expected to be very low and so this simplification is justifiable. The stable contents of Na-O and carbonates suggest that the surface film seems to have a continuous homogeneous composition. However, this cannot be confirmed in the SEM pictures, which is explained in the description of Figure 42 and Figure 43.
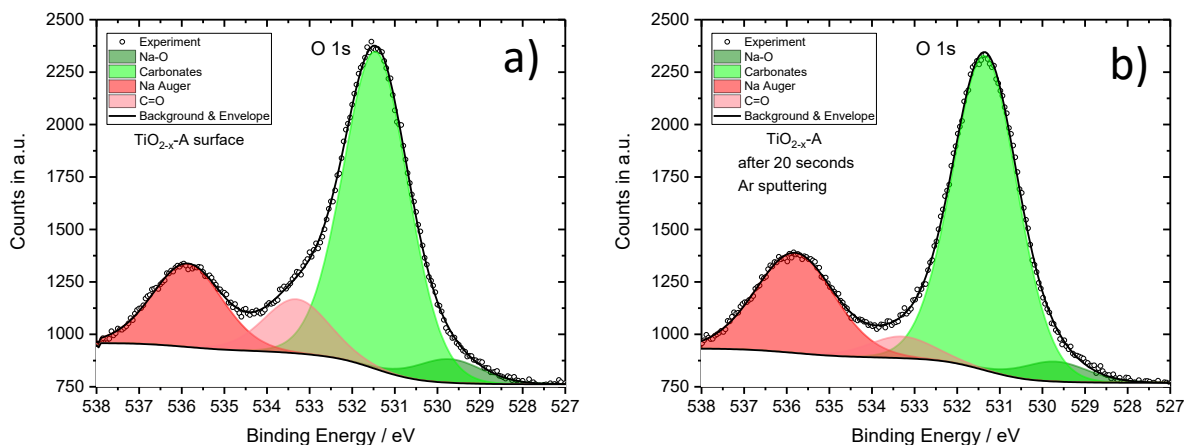


Figure 37.: Post mortem XPS spectra of $TiO_{2-x}$-A sample - a) O 1s surface and b) O 1s after 20 seconds argon sputtering.

The second high-resolution spectrum, which was evaluated in detail, is the C 1s region, depicted in Figure 38. The peak located at 284.5 eV (Figure 38 a) and b) dark green) is related to adventitious carbon. The area percentage increases from 46.59% to 51.95%. The second peak (Figure 38 a) and b) light green) at 286.3 eV can also be assigned to adventitious carbon. By comparing the surface film with the spectrum after 20 s of sputtering it is found that the area percentage scales down from 18.62% to 12.46%, as the peak at the O 1s spectrum does. The carbonate peak, located at 289 eV, remains constant, with 34.79% at the surface and 35.58% after 20 seconds argon sputtering. Here the assertions from the previous paragraph about the O1 s spectra of the $TiO_{2-x}$-A, can be largely confirmed.
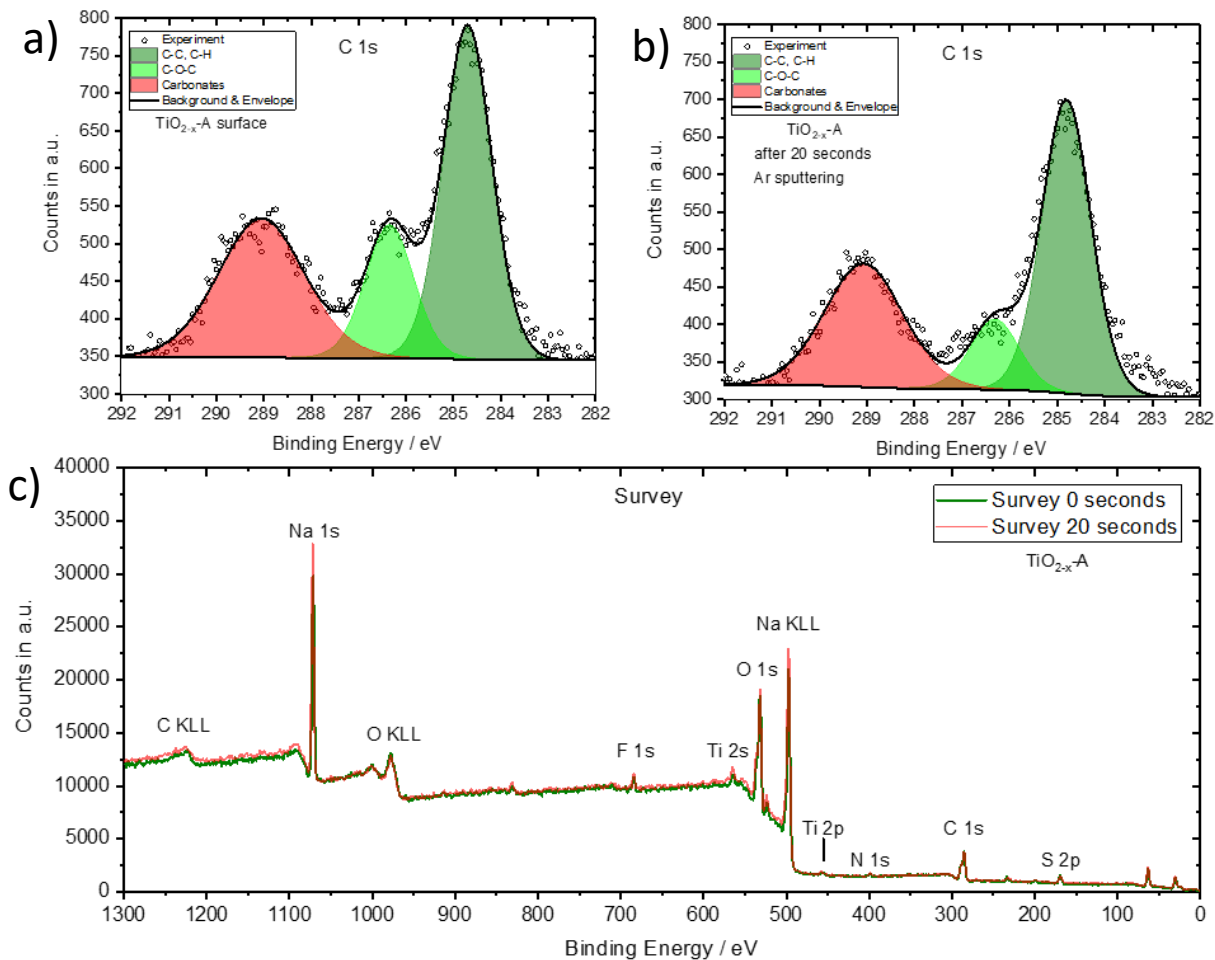
Figure 38.: Post mortem XPS spectra of TiO$_{2-x}$-A sample - a) C 1s surface, b) C 1s after 20 seconds argon sputtering and c) surveys of the surface and after 20 seconds sputtering.

Figure 38 c) shows the survey of the TiO$_{2-x}$-A sample, containing peaks of the S 2p at 169 eV, the N 1s at 399 eV and the F 1s at 638 eV, which can be assigned to the electrolyte, even if it was largely removed when the test cell was disassembled by rinsing the sample several times in dimethyl carbonate (DMC). The weak signals of the Ti 2p and Ti 2s peaks further suggest that the surface film forms a closed layer on top of the oxide. Also in this case, the SEM images in chapter 4.9.1 show that the conclusions in this chapter are not entirely valid.

## 4.8.2. MoO$_{2+x}$

The second part of the post mortem XPS analysis is the evaluation of the MoO$_{2+x}$ spectra. For comparison, the XPS spectra of the initial MoO$_{2+x}$ sample is shown in Figure 39.
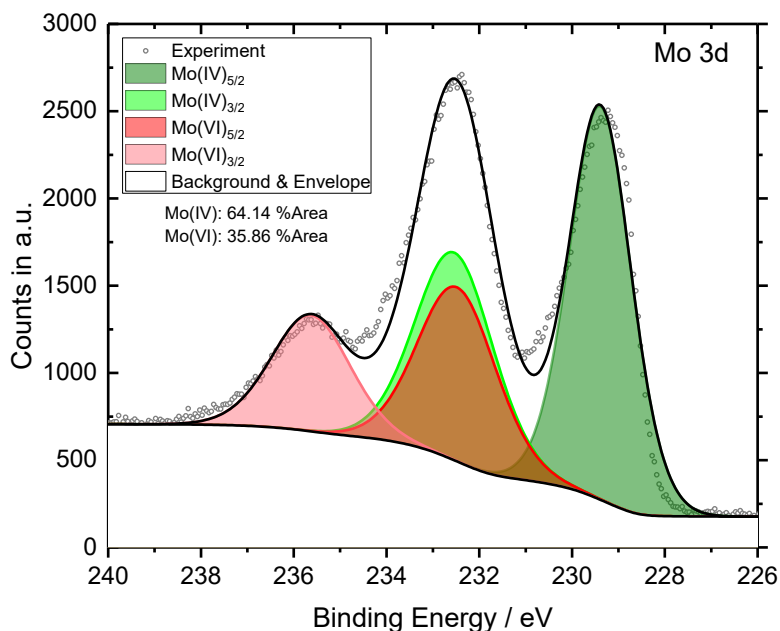


Figure 39.: Mo 3d spectra of the initial MoO$_{2+x}$ sample including relative mass distribution.

The O 1s spectra presented in Figure 40 show four peaks, starting with the Na-O peak at 530.5 eV (Figure 40 a) and b) dark green) related to Na$_2$O$_2$ and Na$_2$O. The actual ratio of the oxide species cannot be determined from this measurement (as previously for the TiO$_{2-x}$-A spectra) due to their similar peak positions (see Table 6). However, the area of the Na-O decreases from 6.14 % to 5.66 %. The carbonate peak, located at 531.6 eV (Figure 40 a) and b) light green), increases slightly from 63.14 % to 64.68 %. These two peaks show also for the MoO$_{2-x}$ electrode, that the surface film is expected to consist of a homogeneous composition.

At 533.2 eV the area of the C=O peak (Figure 40 a) and b) light red) decreases from 12.11 % to 3.32 % indicating that the amount of adventitious carbon is decreasing. Finally, the area of the Na Auger peak located at 536 eV (Figure 40 a) and b)) increases from 18.61 % to 26.35 %.
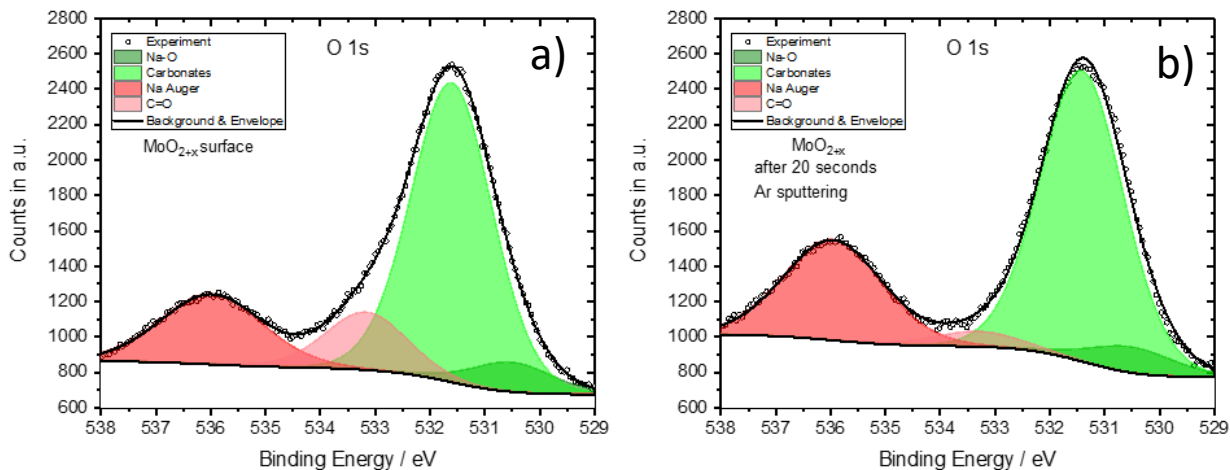
Figure 40.: Post mortem XPS spectra of $MoO_{2+x}$ sample with cut separator a) O 1s surface and b) O 1s after 10 seconds argon sputtering.

The second high-resolution spectrum, which was evaluated in detail, is the C 1s region, shown in Figure 41. The peak located at 284.6 eV (Figure 41 a) and b) dark green) is related to adventitious carbon. The area percentage remains almost unchanged and increases from 37.91% to 37.37%. The second peak (Figure 41 a) and b) light green) at 286.3 eV can also be assigned to adventitious carbon. By comparing the surface film with the spectra after 20 s of sputtering, it is found that the area percentage scales down from 21.57% to 15.74%. The carbonate peak located at 288.9 eV increases from 40.52% at the surface to 46.90% after 20 seconds argon sputtering. Here the assertions from the previous paragraph about the O1 s spectra of the $MoO_{2+x}$ can be largely confirmed.
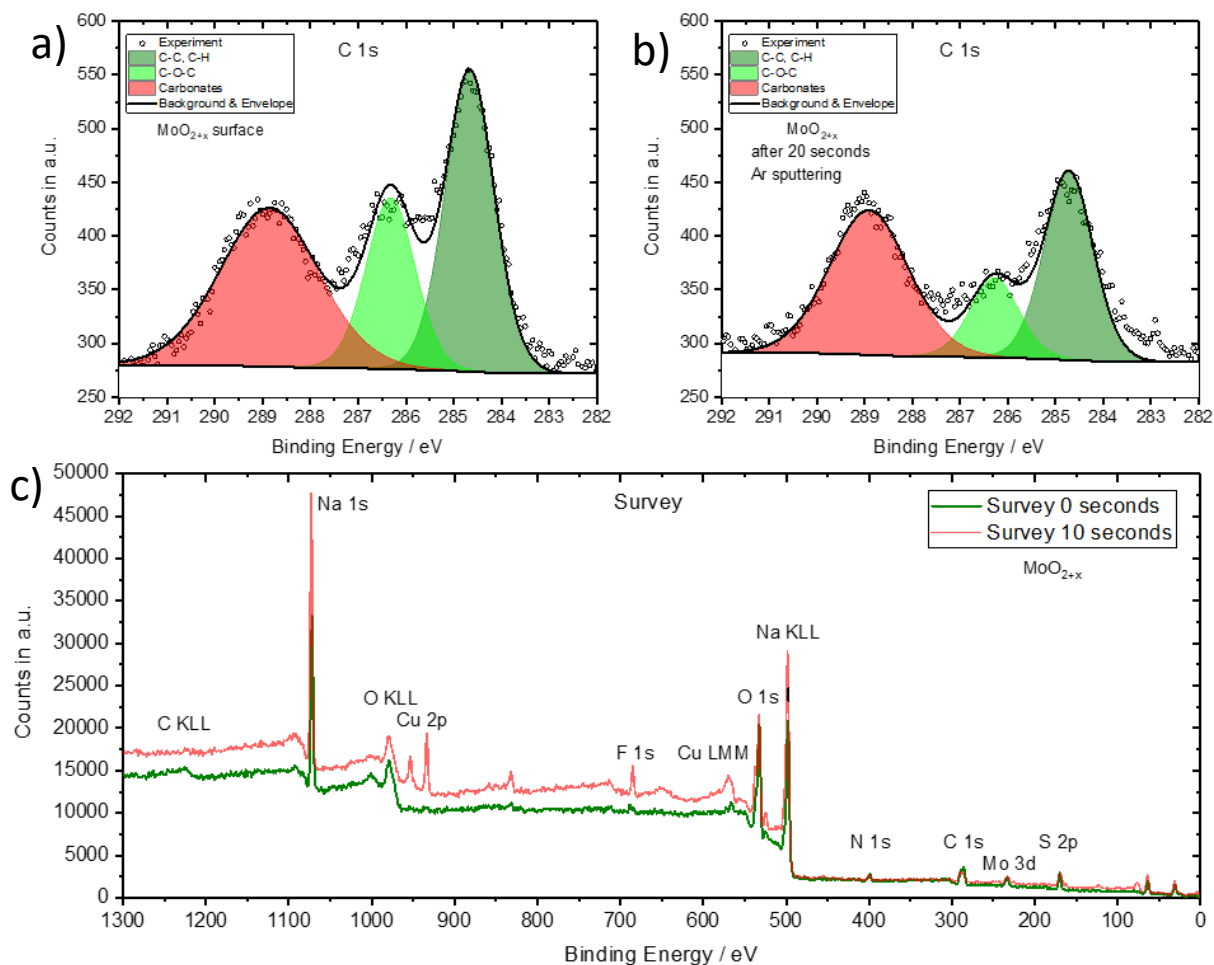
Figure 41.: Post mortem XPS spectra of $MoO_{2+x}$ sample with a cut out separator a) C 1s surface, b) C 1s after 10 seconds argon sputtering, and c) surveys of the surface and after 10 seconds sputtering.

Figure 41 c) shows the survey of the $MoO_{2+x}$ sample, containing peaks of the S 2p at 169 eV, the N 1s at 399 eV and the F 1s at 638 eV, which can be assigned to the electrolyte, even if it was largely removed when the test cell was disassembled by rinsing the sample several times in dimethyl carbonate (DMC). The distinctly visible Mo 3d signal, compared to the weak Ti 2p signal shown in Figure 38 c), at 233 eV suggests that the surface film does not form a closed layer on the oxide. This is also confirmed by the SEM analyses and the corresponding EDX measurement depicted and described in chapter 4.9.2.

## 4.9.    Post mortem SEM analysis

To investigate the composition and the properties of the surface film of the aged $TiO_{2-x}$-A and $MoO_{2+x}$ samples, post mortem SEM pictures with additional energy-dispersive X-ray spectrometry (EDX) measurements were acquired. Therefore, the aged test cells were discharged to a voltage of 0.1 V and then they were immediately disassembled. For all measurements explained in this chapter, it is possible that air impurities changed the composition of the surface film due to the high reactivity of the sodium with oxygen. The contact with air could not be prevented because of the transfer to the SEM setup.

### 4.9.1. $TiO_{2-x}$-A

Figure 42 a) and b) display the surface of the $TiO_{2-x}$-A electrode after 290 GCPL cycles at various scan rates between 117 µA and 2.5 µA. Figure 42 a) shows an overview of the surface. The survey images show protrusions, which occur in clusters on parts of the surface and are relate to sodium oxide. These clusters of sodium oxide demonstrate that the surface film is not a continuous and homogeneous oxide layer, even though sodium can also be detected on the flat areas of the surface. The detailed surface composition is described more precisely in the explanation of the EDX measurements shown in Figure 43.
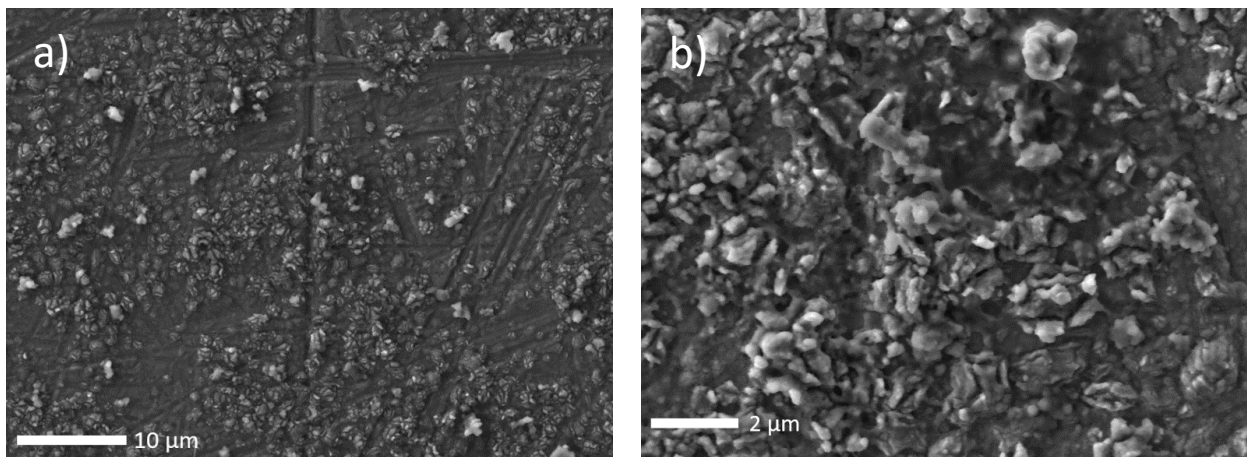


Figure 42.: Post mortem SEM images of the surface of $TiO_{2-x}$-A a) overview and b) zoom.

The detail of the surface area depicted in Figure 42 b) shows such a sodium oxide cluster. The structure of this cluster corresponds with the SEM pictures published in studies by Wu et al. [89] and Portenkirchner et al. [26].
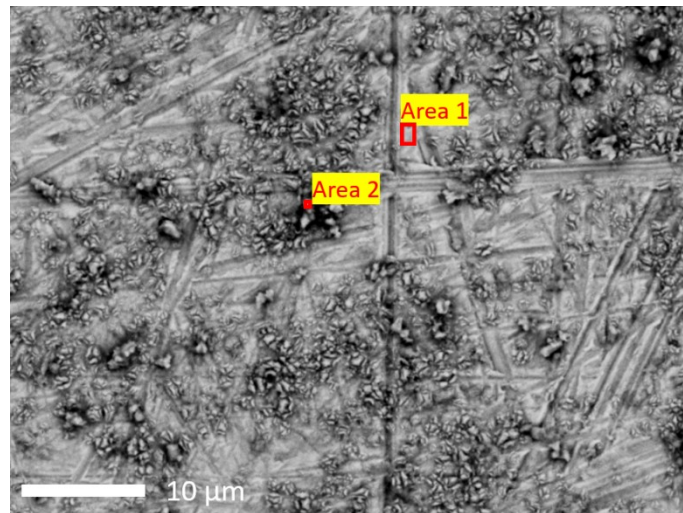


Figure 43.: Post mortem SEM image of the surface of $TiO_{2-x}$-A with two marked areas where EDX measurements were made.

The EDX analyses were performed at the areas marked in Figure 43. Area 1 is representative for the supposedly not sodiated part of the electrode and area 2 is representative for the protrusion clusters. The EDX spectra, containing the signal cps in eV in respect to the energy in keV of both areas are shown in Figure 59. The spectra of area 1 (Figure 59 a)) shows a high oxygen peak (12 eV) at 0.5 keV, a sodium peak (5 eV) at 1 keV and three titanium peaks with a signal of 8 eV at 0.4 keV, 14 eV at 4.2 keV, and 2 eV at 5 keV. A carbon peak can also be located with a signal of 2.5 eV at 0.3 keV. This indicates that the main part of this area contains $TiO_{2-x}$-A and only a small part is sodium oxide and sodium carbonate. The measurement of area 2 depicted in Figure 59 b) shows a different composition. The oxygen peak can be located at 0.5 keV with a signal of over 30 eV. The three titanium peaks at 0.4 keV, 4.2 keV and keV are smaller compared to the signals of area 1 with signal values of 5 eV, 4 eV and 1 eV. The sodium peak at an energy of 1 keV amounts 29 eV, which is also higher compared to the value at area 1. The carbon peak at 0.3 keV also increases to 7 eV. The higher sodium and oxygen values are an indicator that these clusters consist mainly of sodium oxide.

## 4.9.2. MoO$_{2+x}$

In Figure 44 a) and b) the surfaces of the MoO$_{2+x}$ electrode after 290 GCPL cycles at various scan rates between 117 µA and 2.5 µA are shown. The surveys are looking different compared to those of the TiO$_{2-x}$-A. There are again a few protrusion clusters but also larger elongate structures. Again with this sample, the clusters and larger structures demonstrate that the surface film is not a continuous and homogeneous layer.

The detailed surface composition is described more precisely in the explanation of the EDX measurements shown in Figure 45.
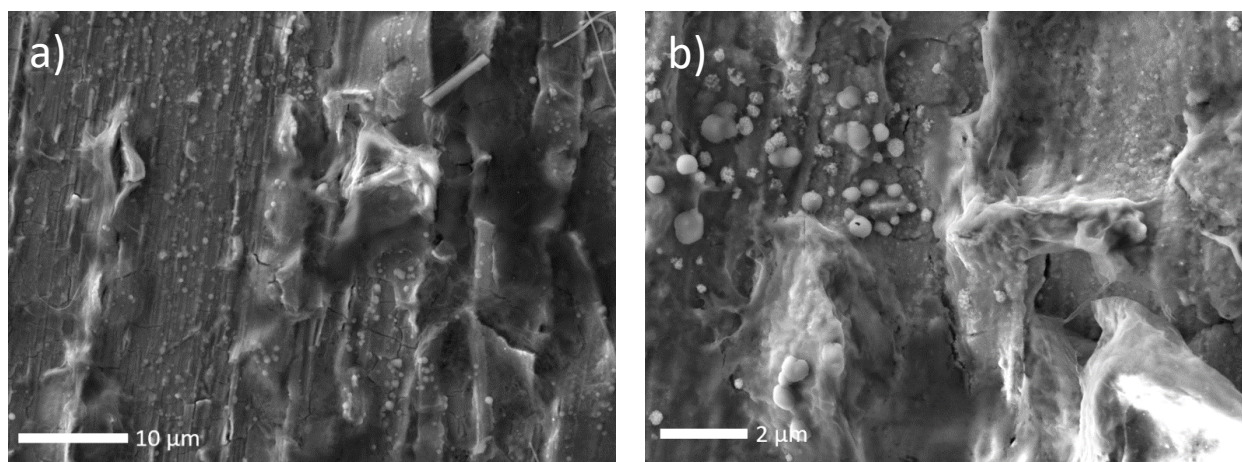


Figure 44.: Post mortem SEM images of the surface of MoO$_{2+x}$ a) overview and b) zoom.

The EDX analyses were performed at the areas marked in Figure 45. Area 1 is representative for the part with the few little protrusion clusters and area 2 is representative for big structures. The EDX spectra, containing the signal cps in eV in respect to the energy in keV of both areas are shown in Figure 60.
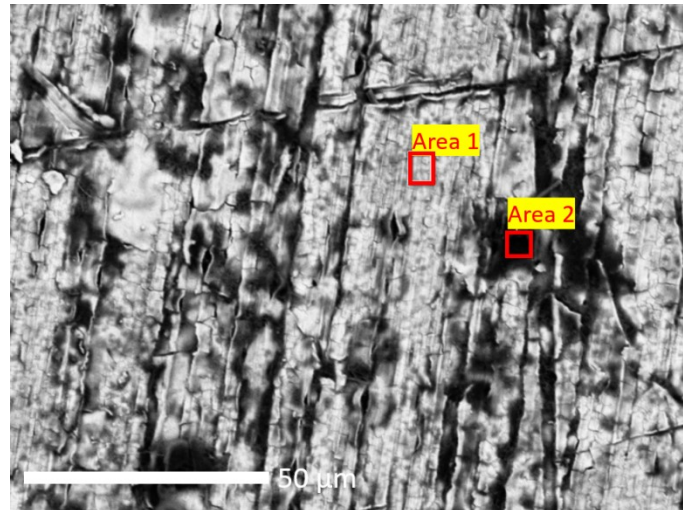
Figure 45.: Post mortem SEM image of the surface of MoO$_{2+x}$ with two marked areas where EDX measurements were made.

The spectra of area 1 depicted in Figure 60 a) shows a high oxygen peak (18 eV) at 0.5 keV, a sodium peak (17 eV) at 1 keV and one Mo peaks with a signal of 15 eV at 2.5 keV. A carbon peak can also be located with a signal of 2.5 eV at 0.3 keV. The Cu peak with a signal of 10 eV located at 0.9 keV indicates that the oxide layer is not very thick and homogenous because this peak is related to the substrate under the MoO$_{2+x}$ film. The high Mo peak is also an indicator that the surface film is not very prominent at this spot.

The measurement of area 2 depicted in Figure 60 b) shows a different composition. The oxygen peak can again be located at 0.5 keV with a signal of over 38 eV. The Mo peak at 2.5 keV is smaller compared to the signal of area 1 with a signal value of 4 eV. The sodium peak at an energy of 1 keV amounts over 42 eV, which is higher compared to the value at area 1. The carbon peak at 0.3 keV also increases to 7 eV. The Cu peak has almost disappeared. The higher values of sodium and oxygen and the lower Mo and Cu peak are indicators, that on the one hand the layer thickness is greater compared to the thickness of the layer at area 1 and on the other hand, the structure consist mainly of sodium oxide.

## 4.10. Post mortem Raman Spectroscopy

Besides the XPS evaluation for investigating the composition of the surface film, Raman spectroscopy was used as an additional characterisation method. For both, $TiO_{2-x}$-A and $MoO_{2+x}$, a point and an area scan were made in the middle of the electrodes. The samples were investigated after the SEM measurements, therefore contact to ambient air, and as a consequence a potential change in the surface components, was unavoidable. Nevertheless, the Raman measurements may confirm the conclusions of the XPS and SEM measurements.

### 4.10.1. $TiO_{2-x}$-A

The spectra of the aged $TiO_{2-x}$-A sample can be seen in Figure 46. The peaks marked with a square (at 153 cm$^{-1}$, 202 cm$^{-1}$, 400 cm$^{-1}$, 516 cm$^{-1}$ and 638 cm$^{-1}$) are the characteristic $TiO_{2-x}$-A peaks which have already been explained in the figure descriptions in chapter 4.1.[64,90]
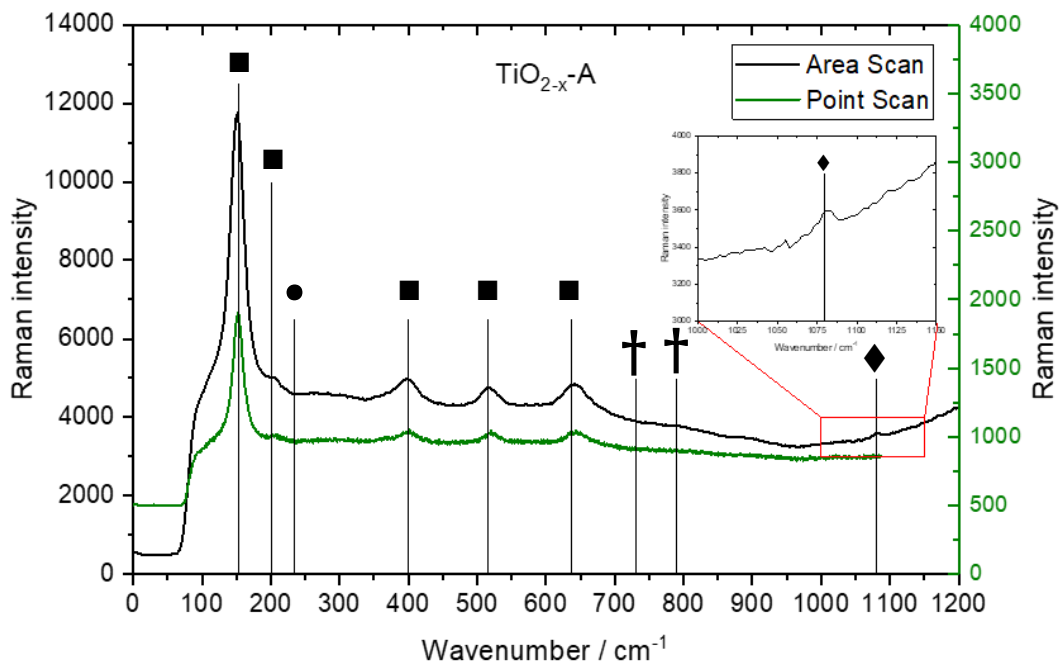


Figure 46.: Raman spectra of the aged $TiO_{2-x}$-A sample with a surface film in the energy range 0-1200 cm$^{-1}$. The $TiO_{2-x}$-A is marked with squares, the $Na_2O$ with a dot, $Na_2O_2$ with a cross and $Na_2Co_3$ with a diamond.

As already mentioned in the explanation of the SEM pictures in chapter 4.9.1, the surface film is very thin and inhomogeneous. This could be the reason why the Raman signal does not include any distinct peak of $Na_2O$, $Na_2O_2$ or $Na_2CO_3$. The $Na_2O$ peak, labelled with a dot, should be located at a wavenumber of 235 $cm^{-1}$, and the $Na_2O_2$ peaks located at 730 $cm^{-1}$ and 790 $cm^{-1}$ are labelled with a cross, respectively.[91] Only at a wavenumber of 1080 $cm^{-1}$ a weak signal can be seen in the spectra of the area scan which is related to $Na_2CO_3$, indicated by the diamond symbol.[91] Additionally, the surface film, which presumably consists of $Na_2O$, $Na_2O_2$ and $Na_2CO_3$, could have changed in its composition during exposure to air, which makes the interpretation difficult.

### 4.10.2.    MoO$_{2+x}$

Also the aged MoO$_{2+x}$ electrode was investigated with Raman spectroscopy (Figure 47). Here the interpretation of the spectra is even more challenging, because additionally to the exposure to air, the surface film is even more inhomogeneous than the TiO$_{2-x}$-A surface film as described in chapter 4.9.2.
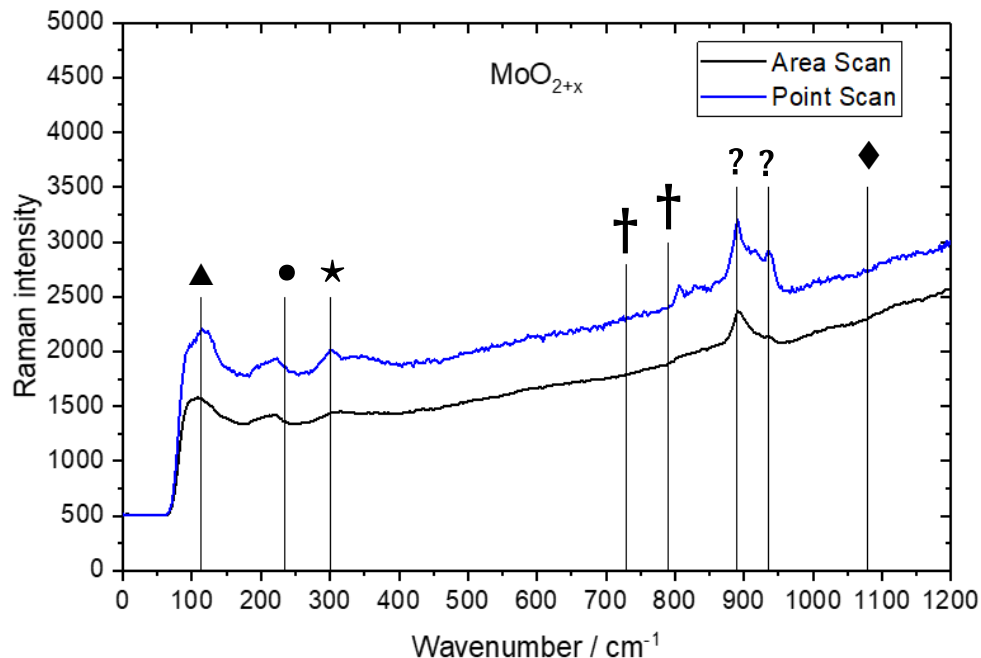


Figure 47.: Raman spectra of the aged MoO$_{2-x}$ sample with a surface film in the energy range 0-1200 $cm^{-1}$. MoO$_{3-x}$ is marked with a triangle, Cu with a star, $Na_2O$ with a dot, $Na_2O_2$ with a cross and $Na_2Co_3$ with a diamond.

The $Na_2O$ and $Na_2O_2$ peaks, marked with a dot and a cross, at wavenumbers of 235 $cm^{-1}$, 730 $cm^{-1}$ and 790 $cm^{-1}$ cannot be found in the spectra shown in Figure 47. Only a weak signal at 800 $cm^{-1}$ in the point

scan can be seen, which is shifted to slightly higher wavenumbers of 805 cm$^{-1}$. The $Na_2CO_3$ peak at 1080 cm$^{-1}$ marked with a diamond does not occur.[91]

The peak at 112 cm$^{-1}$ labelled with a triangle can probably be assigned to a phase represented by the formula $MoO_{3-x}$, with $2 < x < 3$, which has been previously investigated by M. A. Camacho-Lopez et al., and seems to be equivalent to the mixed $MoO_{2+x}$ phase investigated in this thesis.[92] The copper substrate disc could be the reason for the peak at 301 cm$^{-1}$ marked with a star.[93] The last two peaks at wavenumbers of 890 cm$^{-1}$ and 936 cm$^{-1}$ do not correspond to any of the previously mentioned compounds.[92,94]

Unfortunately, the Raman measurements of both electrodes give little indication of the surface film composition, probably due to the low and inhomogeneous thickness of the film.

# 5. Conclusion

Different electrode materials were synthesised and their suitability as electrode material in SIB were investigated via electrochemical characterisation.

Electrochemical oxidation was used for the synthesis of $TiO_{2-x}$-A, $TiO_{2-x}$-R and $TiO_2$-M with additional thermally-induced phase transition in a quartz tube furnace in Ar for $TiO_{2-x}$-A and $TiO_{2-x}$-R. Raman spectroscopy, XPS and SEM were performed to confirm the successful preparation of the electrodes and to check the morphology of the surface.

PVD was carried out for the synthesis of $MoO_{2+x}$ because the aforementioned thermal phase transition was not successful. The above-mentioned characterization methods were also applied here to investigate the composition and surface properties. It turned out that the oxide layer consists of a mixed phase of Mo(IV)-oxide and Mo(VI)-oxide throughout. This can be attributed to the immediate oxidation of Mo(IV)-oxide in air, which happens due to the unavoidable, short contact with air caused by the experimental setup.

The CVs of $TiO_{2-x}$-A show distinct reduction and oxidation peaks, which indicate the voltage at which the storage of sodium occurs. The SPEIS measurements additionally indicate that the major Na storage presumably takes place in the surface film, which builds up during long-term sodiation/desodiation, and that bulk diffusion plays a minor part in the Na storage process.

The specific capacity of the $TiO_{2-x}$-A cells increases with decreasing scan rates and within a scan rate with increasing cycle number, which suggests that the self-improvement effect postulated by Portenkirchner et al. also occurs at planar $TiO_{2-x}$-A electrodes.[8]

The exact composition of the surface film could not be determined unambiguously in the post mortem analysis including XPS, Raman and SEM.

The results of the electrochemical characterization reveal that a self-improvement effect can also be found for the $MoO_{2+x}$ electrode. However, CVs only show reduction and oxidation peaks at very slow scan rates and GCPL measurements only demonstrate a self-improvement effect at high C-rates.

Post mortem analysis additionally shows that the surface film is very inhomogeneous.

The electrochemical characterisation of $TiO_2$-M and $TiO_{2-x}$-R could not be performed due to time constraints; however, the tests will be carried out later on.

Further investigations are necessary for all electrode materials in order to determine the exact composition of the surface film and thus to be able to make more precise statements about the Na storage process.

# 6. List of references

[1]    F. Diaz Alonso, eurostat, *Erneuerbare Energien in der EU im Jahr 2018*, **2020.** 4.

[2]    Statistik Austria, *Kfz Bestand 2019*, **2020.** 14.

[3]    F. Kirchbacher, P. Biegger, M. Miltner, M. Lehner, M. Harasek *A new methanation and membrane based power-to-gas process for the direct integration of raw biogas – Feasability and comparison*, *Energy* **2018**, *146*, 34, DOI 10.1016/j.energy.2017.05.026.

[4]    P. K. Nayak, L. Yang, W. Brehm, P. Adelhelm *From Lithium-Ion to Sodium-Ion Batteries: Advantages, Challenges, and Surprises*, *Angewandte Chemie (International ed. in English)* **2018**, *57*, 102, DOI 10.1002/anie.201703772.

[5]    L. Li, J. Ge, R. Chen, F. Wu, S. Chen, X. Zhang *Environmental friendly leaching reagent for cobalt and lithium recovery from spent lithium-ion batteries*, *Waste management (New York, N.Y.)* **2010**, *30*, 2615, DOI 10.1016/j.wasman.2010.08.008.

[6]    K.-C. Möller in *Handbuch Lithium-Ionen-Batterien* (Hrsg.: R. Korthauer), Springer Berlin Heidelberg, **2013**, S. 3–9.

[7]    "https://pixabay.com/de/vectors/graphen-graphit-benzol-chemie-161773/".

[8]    E. Portenkirchner, D. Werner, S. Liebl, D. Stock, A. Auer, J. Kunze-Liebhäuser *Self-Improving Na Ion Storage in Oxygen Deficient, Carbon Coated Self-Organized TiO 2 Nanotubes*, *ACS Appl. Energy Mater.* **2018**, *1*, 6646, DOI 10.1021/acsaem.8b01712.

[9]    L. Wu, D. Bresser, D. Buchholz, G. A. Giffin, C. R. Castro, A. Ochel, S. Passerini *Unfolding the Mechanism of Sodium Insertion in Anatase TiO 2 Nanoparticles*, *Adv. Energy Mater.* **2015**, *5*, 1401142, DOI 10.1002/aenm.201401142.

[10]   M. D. Slater, D. Kim, E. Lee, C. S. Johnson *Sodium-Ion Batteries*, *Adv. Funct. Mater.* **2013**, *23*, 947, DOI 10.1002/adfm.201200691.

[11]   M. Sook Oh, B. Seob Yang, J. Ho Lee, S. Ha Oh, U. Soo Lee, Y. Jang Kim, H. Joon Kim, M. Soo Huh *Improvement of electrical and optical properties of molybdenum oxide thin films by ultralow pressure sputtering method*, *Journal of Vacuum Science & Technology A: Vacuum, Surfaces, and Films* **2012**, *30*, 31501, DOI 10.1116/1.3692753.

[12]   C. A. Ellefson, O. Marin-Flores, S. Ha, M. G. Norton *Synthesis and applications of molybdenum (IV) oxide*, *J Mater Sci* **2012**, *47*, 2057, DOI 10.1007/s10853-011-5918-5.

[13]   S. Hariharan, K. Saravanan, P. Balaya *α-MoO3: A high performance anode material for sodium-ion batteries*, *Electrochemistry Communications* **2013**, *31*, 5, DOI 10.1016/j.elecom.2013.02.020.

[14]   K. Zhu, S. Guo, J. Yi, S. Bai, Y. Wei, G. Chen, H. Zhou *A new layered sodium molybdenum oxide anode for full intercalation-type sodium-ion batteries*, *J. Mater. Chem. A* **2015**, *3*, 22012, DOI 10.1039/C5TA05444C.

[15]   J. Baltrusaitis, B. Mendoza-Sanchez, V. Fernandez, R. Veenstra, N. Dukstiene, A. Roberts, N. Fairley *Generalized molybdenum oxide surface chemical state XPS determination via informed amorphous sample model*, *Applied Surface Science* **2015**, *326*, 151, DOI 10.1016/j.apsusc.2014.11.077.

[16]   Edith Bucher, *Phase diagram created with FactSage 7.3, thermodynamic software package, (c) 1976-2019 Thermfact and GTT-Technologies*, Montanuniversitaet Leoben.

[17]  Q. He, O. Marin-Flores, S. Hu, L. Scudiero, S. Ha, M. G. Norton *Effect of titanium doping on the structure and reducibility of nanoparticle molybdenum dioxide*, *J Nanopart Res* **2014**, *16*, 1, DOI 10.1007/s11051-014-2385-3.

[18]  Shang-Di Mo and W. Y. Ching *Electronic and optical properties of three phases of titanium dioxide: Rutile, anatase, and brookite*, *Physical Review B* **1995**, 13023, 13032, DOI 10.1103/PhysRevB.51.13023.

[19]  M. Horn, C. F. Schwerdtfeger, E. P. Meagher *Refinement of the structure of anatase at several temperatures*, *Zeitschrift für Kristallographie*, *1972*, 273, DOI 10.1524/zkri.1972.136.3-4.273.

[20]  S. Yang, N. Huang, Y. M. Jin, H. Q. Zhang, Y. H. Su, H. G. Yang *Crystal shape engineering of anatase TiO 2 and its biomedical applications*, *CrystEngComm* **2015**, *17*, 6617, DOI 10.1039/C5CE00804B.

[21]  W. H. Baur, A. A. Khan *Rutile-Type Compounds. VI. Si O2, Ge O2 and a Comparison with other Rutile-Type Structures*, *Acta Crystallographica, Section B: Structural Crystallography and Crystal Chemistry*, *1971*, 2133, DOI 10.1107/S0567740871005466.

[22]  S. Sun, P. Song, J. Cui, S. Liang *Amorphous TiO 2 nanostructures: synthesis, fundamental properties and photocatalytic applications*, *Catal. Sci. Technol.* **2019**, *9*, 4198, DOI 10.1039/C9CY01020C.

[23]  Y. Ju, M. Wang, Y. Wang, S. Wang, C. Fu *Electrical Properties of Amorphous Titanium Oxide Thin Films for Bolometric Application*, *Advances in Condensed Matter Physics* **2013**, *2013*, 1, DOI 10.1155/2013/365475.

[24]  G. G. Eshetu, T. Diemant, M. Hekmatfar, S. Grugeon, R. J. Behm, S. Laruelle, M. Armand, S. Passerini *Impact of the electrolyte salt anion on the solid electrolyte interphase formation in sodium ion batteries*, *Nano Energy* **2019**, *55*, 327, DOI 10.1016/j.nanoen.2018.10.040.

[25]  W. Li, M. Fukunishi, B. J. Morgan, O. J. Borkiewicz, K. W. Chapman, V. Pralong, A. Maignan, O. I. Lebedev, J. Ma, H. Groult et al. *A Reversible Phase Transition for Sodium Insertion in Anatase TiO 2*, *Chem. Mater.* **2017**, *29*, 1836, DOI 10.1021/acs.chemmater.7b00098.

[26]  E. Portenkirchner, S. Rommel, L. Szabados, C. Griesser, D. Werner, D. Stock, J. Kunze-Liebhäuser *Surface Films Formed at Sodium Ion Battery Anodes and their Contribution on the Charge Storage Characteristics (Submitted)*, *Submitted* **2020**.

[27]  J. K. Shon, H. S. Lee, G. O. Park, J. Yoon, E. Park, G. S. Park, S. S. Kong, M. Jin, J.-M. Choi, H. Chang et al. *Discovery of abnormal lithium-storage sites in molybdenum dioxide electrodes*, *Nature communications* **2016**, *7*, 11049, DOI 10.1038/ncomms11049.

[28]  X. Zhao, Y. Zhao, Y. Yang, Z. Liu, H.-E. Wang, J. Sui, W. Cai *Fresh MoO 2 as a better electrode for pseudocapacitive sodium-ion storage*, *New J. Chem.* **2018**, *42*, 14721, DOI 10.1039/C8NJ03570A.

[29]  R. J. Nemanich, C. C. Tsai, and G. A. N. Connell *Interference-Enhanced Raman Scattering of Very Thin Titanium and Titanium Oxide Films*, *Physical review letters*, *1980*, 273, DOI 10.1103/PhysRevLett.44.273.

[30]  M. Bossle, D. Lingenhöhl, "Raman-Effekt", https://www.spektrum.de/lexikon/physik/raman-effekt/12045.

[31]  Peter J. Larkin, *Infrared and Raman Spectroscopy. Principles and spectral interpretation*. Second Edition, **2018.** 15-19.

[32]  P. Reyes-Figueroa, T. Painchaud, T. Lepetit, S. Harel, L. Arzel, J. Yi, N. Barreau, S. Velumani *Structural properties of In2Se3 precursor layers deposited by spray pyrolysis and physical vapor*

*deposition for CuInSe2 thin-film solar cell applications*, *Thin Solid Films* **2015**, *587*, 112, DOI 10.1016/j.tsf.2015.01.035.

[33] D. Abou-Ras, G. Kostorz, A. Romeo, D. Rudmann, A. N. Tiwari *Structural and chemical investigations of CBD- and PVD-CdS buffer layers and interfaces in Cu(In,Ga)Se2-based thin film solar cells*, *Thin Solid Films* **2005**, *480-481*, 118, DOI 10.1016/j.tsf.2004.11.033.

[34] M. Tanhaei, M. Mozammel *Yttria-stabilized zirconia thin film electrolyte deposited by EB-PVD on porous anode support for SOFC applications*, *Ceramics International* **2017**, *43*, 3035, DOI 10.1016/j.ceramint.2016.11.097.

[35] X. He, B. Meng, Y. Sun, B. Liu, M. Li *Electron beam physical vapor deposition of YSZ electrolyte coatings for SOFCs*, *Applied Surface Science* **2008**, *254*, 7159, DOI 10.1016/j.apsusc.2008.05.271.

[36] N. Selvakumar, H. C. Barshilia *Review of physical vapor deposited (PVD) spectrally selective coatings for mid- and high-temperature solar thermal applications*, *Solar Energy Materials and Solar Cells* **2012**, *98*, 1, DOI 10.1016/j.solmat.2011.10.028.

[37] M. M. Hassan in *Handbook of Antimicrobial Coatings*, Elsevier, **2018**, S. 343–344.

[38] T. Götsch, E.-M. Wernig, B. Klötzer, T. Schachinger, J. Kunze-Liebhäuser, S. Penner *An ultra-flexible modular high vacuum setup for thin film deposition*, *The Review of scientific instruments* **2019**, *90*, 23902, DOI 10.1063/1.5065786.

[39] Steiner Dominik, "Surface Analysis Studies during Lithiation and Delithiation of Surface Analysis Studies during Lithiation and Delithiation of Amorphous and Anatase TiO2 Nanotubes", *Master Thesis*, Universität Innsbruck. 2016.

[40] M.C. Biesinger, "X-ray Photoelectron Spectroscopy (XPS) Reference Pages. Backgrounds", http://www.xpsfitting.com/search/label/Backgrounds, **2009-2018**.

[41] N. Fairley, "Peak Fitting in XPS", www.casaxps.com, **2006**.

[42] M.C. Biesinger, "X-ray Photoelectron Spectroscopy (XPS) Reference Pages. Line-Shapes", http://www.xpsfitting.com/search/label/Line-Shapes, **2009-2018**.

[43] L. D. WHITTIG AND W. R. ALLARDICE, *X-Ray Diffraction Techniques*. *University of California Davis, California*, **1986.** 32.

[44] Auer Andrea, "Study of Crystallographically Random and Preferential Oriented TiO2 Nanotube Study of crystallographically random and preferential oriented TiO2 Nanutube Arrays as Anode Material for Lithium Ion Batteries Lithium Ion Batteries", *Master Thesis*, Universität Innsbruck, Innsbruck. 02.2016.

[45] BioLogic Science Instruments, *EC-Lab User's Manual*. *Version 10.38.* 211.

[46] R. Korthauer (Hrsg.) *Handbuch Lithium-Ionen-Batterien*, Springer Berlin Heidelberg, **2013**.

[47] N. Elgrishi, K. J. Rountree, B. D. McCarthy, E. S. Rountree, T. T. Eisenhart, J. L. Dempsey *A Practical Beginner's Guide to Cyclic Voltammetry*, *J. Chem. Educ.* **2018**, *95*, 197, DOI 10.1021/acs.jchemed.7b00361.

[48] J. Heinze *Cyclovoltammetrie — die „Spektroskopie" des Elektrochemikers*, *Angewandte Chemie (International ed. in English)* **1984**.

[49] E. Lalik, W. I. F. David, P. Barnes, J. F. C. Turner *Mechanisms of Reduction of MoO 3 to MoO 2 Reconciled?*, *J. Phys. Chem. B* **2001**, *105*, 9153, DOI 10.1021/jp011622p.

[50] W. Zhang, L. Xing, J. Chen, H. Zhou, S. Liang, W. Huang, W. Li *Improving the cyclic stability of MoO2 anode for sodium ion batteries via film-forming electrolyte additive*, *Journal of Alloys and Compounds* **2020**, *822*, 153530, DOI 10.1016/j.jallcom.2019.153530.

[51]    J. Huang, Z. Xu, L. Cao, Q. Zhang, H. Ouyang, J. Li *Tailoring MoO 2 /Graphene Oxide Nanostructures for Stable, High-Density Sodium-Ion Battery Anodes*, *Energy Technol.* **2015**, *3*, 1108, DOI 10.1002/ente.201500160.

[52]    A. Auer, N. S. W. Jonasson, D. H. Apaydin, A. I. Mardare, G. Neri, J. Lichtinger, R. Gernhäuser, J. Kunze-Liebhäuser, E. Portenkirchner *Optimized Design Principles for Silicon-Coated Nanostructured Electrode Materials and their Application in High-Capacity Lithium-Ion Batteries*, *Energy Technol.* **2017**, *5*, 2253, DOI 10.1002/ente.201700306.

[53]    L. Calvillo, D. Fittipaldi, C. Rüdiger, S. Agnoli, M. Favaro, C. Valero-Vidal, C. Di Valentin, A. Vittadini, N. Bozzolo, S. Jacomet et al. *Carbothermal Transformation of TiO 2 into TiO x C y in UHV: Tracking Intrinsic Chemical Stabilities*, *J. Phys. Chem. C* **2014**, *118*, 22601, DOI 10.1021/jp506728w.

[54]    Auer A., Steiner D., Portenkirchner E., Kunze-Liebhäuser J., *Nonequilibrium Phase Transition in Amorphous and Anatase TiO2 Nanotubes*. *Supporting Information.* 4.

[55]    D. A. H. Hanaor, C. C. Sorrell *Review of the anatase to rutile phase transformation*, *J Mater Sci* **2011**, *46*, 855, DOI 10.1007/s10853-010-5113-0.

[56]    M. Hahn, *Electrochemical Test Cell ECC-Ref.* 22-01-2014. 17.

[57]    Solvonic, *Catalogue-Electrolytes-Materials*, **2017-2018.** 20.

[58]    J. Xing, Z. Xia, J. Hu, Y. Zhang, L. Zhong *Time dependence of growth and crystallization of anodic titanium oxide films in potentiostatic mode*, *Corrosion Science* **2013**, *75*, 212, DOI 10.1016/j.corsci.2013.06.004.

[59]    Z. Xia, H. Nanjo, T. Aizawa, M. Kanakubo, M. Fujimura, J. Onagawa *Growth process of atomically flat anodic films on titanium under potentiostatical electrochemical treatment in H2SO4 solution*, *Surface Science* **2007**, *601*, 5133, DOI 10.1016/j.susc.2007.04.211.

[60]    N. K. Kuromoto, R. A. Simão, G. A. Soares *Titanium oxide films produced on commercially pure titanium by anodic oxidation with different voltages*, *Materials Characterization* **2007**, *58*, 114, DOI 10.1016/j.matchar.2006.03.020.

[61]    A. Auer, E. Portenkirchner, T. Götsch, C. Valero-Vidal, S. Penner, J. Kunze-Liebhäuser *Preferentially Oriented TiO2 Nanotubes as Anode Material for Li-Ion Batteries: Insight into Li-Ion Storage and Lithiation Kinetics*, *ACS applied materials & interfaces* **2017**, *9*, 36828, DOI 10.1021/acsami.7b11388.

[62]    O. Anderson, C. R. Ottermann, R. Kuschnereit, P. Hess, K. Bange *Density and Young's modulus of thin TiO 2 films*, *Fresenius J Anal Chem* **1997**, *358*, 315, DOI 10.1007/s002160050416.

[63]    *The Mo-O system (Molybdenum-Oxygen)*, *Bulletin of Alloy Phase Diagrams*, *1980*, 85.

[64]    O. Frank, M. Zukalova, B. Laskova, J. Kürti, J. Koltai, L. Kavan *Raman spectra of titanium dioxide (anatase, rutile) with identified oxygen isotopes (16, 17, 18)*, *Physical chemistry chemical physics : PCCP* **2012**, *14*, 14567, DOI 10.1039/c2cp42763j.

[65]    M.C. Biesinger, "X-ray Photoelectron Spectroscopy (XPS) Reference Pages. Charge Correcting to C 1s in CasaXPS", http://www.xpsfitting.com/search/label/XPS%20Description, **2009-2018**.

[66]    M. C. Biesinger, L. W.M. Lau, A. R. Gerson, R. S.C. Smart *Resolving surface chemical states in XPS analysis of first row transition metals, oxides and hydroxides: Sc, Ti, V, Cu and Zn*, *Applied Surface Science* **2010**, *257*, 887, DOI 10.1016/j.apsusc.2010.07.086.

[67]    C.D. Wagner, A.V. Naumkin, A. Kraut-Vass, J.W. Allison, C.J. Powell, J.R.Jr. Rumble, "NIST Standard Reference Database 20, Version 3.4 (web version)", https://srdata.nist.gov/xps/, **2003**.

[68]   C. R. Clayton, Y. C. Lu *Electrochemical and XPS evidence of the aqueous formation of Mo2O5*, *Surface and Interface Analysis* **1989**, 66.

[69]   D. B. G. Beamson, "High Resolution XPS of Organic Polymers - The Scienta ESCA300 Database Wiley Interscience".

[70]   Q. Zhu, M. Wang, B. Nan, H. Shi, X. Zhang, Y. Deng, L. Wang, Q. Chen, Z. Lu *Core/shell nanostructured Na 3 V 2 (PO 4 ) 3 /C/TiO 2 composite nanofibers as a stable anode for sodium-ion batteries*, *Journal of Power Sources* **2017**, *362*, 147, DOI 10.1016/j.jpowsour.2017.07.004.

[71]   L.-F. Que, F.-D. Yu, Z.-B. Wang, D.-M. Gu *Pseudocapacitance of TiO2-x /CNT Anodes for High-Performance Quasi-Solid-State Li-Ion and Na-Ion Capacitors*, *Small (Weinheim an der Bergstrasse, Germany)* **2018**, *14*, e1704508, DOI 10.1002/smll.201704508.

[72]   Y.-E. Zhu, L. Yang, J. Sheng, Y. Chen, H. Gu, J. Wei, Z. Zhou *Fast Sodium Storage in TiO 2 @CNT@C Nanorods for High-Performance Na-Ion Capacitors*, *Adv. Energy Mater.* **2017**, *7*, 1701222, DOI 10.1002/aenm.201701222.

[73]   S. Rommel, "Intercalation Characteristics of Sodium Ions in Amorphous and Anatase TiO2 Nanotubes", *Master Thesis*, Innsbruck. 2019.

[74]   L. Wu, D. Buchholz, D. Bresser, L. Gomes Chagas, S. Passerini *Anatase TiO2 nanoparticles for high power sodium-ion anodes*, *Journal of Power Sources* **2014**, *251*, 379, DOI 10.1016/j.jpowsour.2013.11.083.

[75]   Z. Le, F. Liu, P. Nie, X. Li, X. Liu, Z. Bian, G. Chen, H. B. Wu, Y. Lu *Pseudocapacitive Sodium Storage in Mesoporous Single-Crystal-like TiO2-Graphene Nanocomposite Enables High-Performance Sodium-Ion Capacitors*, *ACS Nano* **2017**, *11*, 2952, DOI 10.1021/acsnano.6b08332.

[76]   J. Jiang, W. Yang, H. Wang, Y. Zhao, J. Guo, J. Zhao, M. Beidaghi, L. Gao *Electrochemical Performances of MoO2/C Nanocomposite for Sodium Ion Storage: An Insight into Rate Dependent Charge/Discharge Mechanism*, *Electrochimica Acta* **2017**, *240*, 379, DOI 10.1016/j.electacta.2017.04.103.

[77]   D. Steiner, A. Auer, E. Portenkirchner, J. Kunze-Liebhäuser *The role of surface films during lithiation of amorphous and anatase TiO2 nanotubes*, *Journal of Electroanalytical Chemistry* **2018**, *812*, 166, DOI 10.1016/j.jelechem.2017.11.035.

[78]   A. Auer, J. Kunze-Liebhäuser *Recent Progress in Understanding Ion Storage in Self-Organized Anodic TiO 2 Nanotubes*, *Small Methods* **2018**, *3*, 1800385, DOI 10.1002/smtd.201800385.

[79]   L. Gao, L. Wang, S. Dai, M. Cao, Z. Zhong, Y. Shen, M. Wang *Li4Ti5O12-TiO2 nanowire arrays constructed with stacked nanocrystals for high-rate lithium and sodium ion batteries*, *Journal of Power Sources* **2017**, *344*, 223, DOI 10.1016/j.jpowsour.2017.01.033.

[80]   Z. Yan, L. Liu, J. Tan, Q. Zhou, Z. Huang, D. Xia, H. Shu, X. Yang, X. Wang *One-pot synthesis of bicrystalline titanium dioxide spheres with a core–shell structure as anode materials for lithium and sodium ion batteries*, *Journal of Power Sources* **2014**, *269*, 37, DOI 10.1016/j.jpowsour.2014.06.150.

[81]   W. J. H. Borghols, D. Lützenkirchen-Hecht, U. Haake, E. R. H. van Eck, F. M. Mulder, M. Wagemaker *The electronic structure and ionic diffusion of nanoscale LiTiO2 anatase*, *Phys. Chem. Chem. Phys.* **2009**, *11*, 5742, DOI 10.1039/B823142G.

[82]   H. Yadegari, Y. Li, M. N. Banis, X. Li, B. Wang, Q. Sun, R. Li, T.-K. Sham, X. Cui, X. Sun *On rechargeability and reaction kinetics of sodium–air batteries*, *Energy Environ. Sci.* **2014**, *7*, 3747, DOI 10.1039/C4EE01654H.

[83]    J. F. Moulder, W.F. Stickle, P.E. Sobol, K.D. Bomben, *Handbook of X-ray Photoelectron Spectroscopy. A Reference Book of Standard Spectra for Identification and Interpretation of XPS Data.* 260.

[84]    M.C. Biesinger, "X-ray Photoelectron Spectroscopy (XPS) Reference Pages. Oxygen", http://www.xpsfitting.com/search/label/Oxygen.

[85]    Thermo Fisher Scientific Inc., "Thermo scientific XPS. oxygen", https://xpssimplified.com/elements/oxygen.php.

[86]    M.C. Biesinger, "X-ray Photoelectron Spectroscopy (XPS) Reference Pages. carbon", http://www.xpsfitting.com/search/label/carbon.

[87]    M.C. Biesinger, "X-ray Photoelectron Spectroscopy (XPS) Reference Pages. sodium", http://www.xpsfitting.com/search/label/Sodium.

[88]    Thermo Fisher Scientific Inc., "Thermo scientific XPS. sodium", https://xpssimplified.com/elements/sodium.php, **2013-2020**.

[89]    L. Wu, D. Bresser, D. Buchholz, G. A. Giffin, C. R. Castro, A. Ochel, S. Passerini *Unfolding the Mechanism of Sodium Insertion in Anatase TiO 2 Nanoparticles*, *Adv. Energy Mater.* **2015**, *5*, 1, DOI 10.1002/aenm.201401142.

[90]    L. M. F. Arias, A. A. Duran, D. Cardona, E. Camps, M. E. Gómez, G. Zambrano *Effect of annealing treatment on the photocatalytic activity of TiO 2 thin films deposited by dc reactive magnetron sputtering*, *J. Phys.: Conf. Ser.* **2015**, *614*, 12008, DOI 10.1088/1742-6596/614/1/012008.

[91]    L.-Y. Kuo, A. Moradabadi, H.-F. Huang, B.-J. Hwang, P. Kaghazchi *Structure and ionic conductivity of the solid electrolyte interphase layer on tin anodes in Na-ion batteries*, *Journal of Power Sources* **2017**, *341*, 107, DOI 10.1016/j.jpowsour.2016.11.077.

[92]    M. A. Camacho-López, L. Escobar-Alarcón, M. Picquart, R. Arroyo, G. Córdoba, E. Haro-Poniatowski *Micro-Raman study of the m-MoO2 to α-MoO3 transformation induced by cw-laser irradiation*, *Optical Materials* **2011**, *33*, 480, DOI 10.1016/j.optmat.2010.10.028.

[93]    S. Chen, L. Brown, M. Levendorf, W. Cai, S.-Y. Ju, J. Edgeworth, X. Li, C. W. Magnuson, A. Velamakanni, R. D. Piner et al. *Oxidation resistance of graphene-coated Cu and Cu/Ni alloy*, *ACS Nano* **2011**, *5*, 1321, DOI 10.1021/nn103028d.

[94]    L. Kumari, Y.-R. Ma, C.-C. Tsai, Y.-W. Lin, S. Y. Wu, K.-W. Cheng, Y. Liou *X-ray diffraction and Raman scattering studies on large-area array and nanobranched structure of 1D MoO 2 nanorods*, *Nanotechnology* **2007**, *18*, 115717, DOI 10.1088/0957-4484/18/11/115717.

[95]    O. Frank, M. Zukalova, B. Laskova, J. Kürti, J. Koltai, L. Kavan *Raman spectra of titanium dioxide (anatase, rutile) with identified oxygen isotopes (16, 17, 18)*, *Physical chemistry chemical physics : PCCP* **2012**, *14*, 14567, DOI 10.1039/c2cp42763j.

[96]    M. D. Wiggins, M. C. Nelson, C. R. Aita *Phase development in sputter deposited titanium dioxide*, *Journal of Vacuum Science & Technology A: Vacuum, Surfaces, and Films* **1996**, *14*, 772, DOI 10.1116/1.580387.

[97]    J. Shi, X. Wang *Growth of Rutile Titanium Dioxide Nanowires by Pulsed Chemical Vapor Deposition*, *Crystal Growth & Design* **2011**, *11*, 949, DOI 10.1021/cg200140k.

[98]    E. Gamelli, N.H.A. Camargo *Oxidation kinetics of commercially pure titanium*, *revista Materia*, *2007*, 525.

[99]    M. Sabeena, S. Murugesan, P. Anees, E. Mohandas, M. Vijayalakshmi *Crystal structure and bonding characteristics of transformation products of bcc beta in Ti-Mo alloys*, *Journal of Alloys and Compounds* **2017,** DOI 10.1016/j.jallcom.2016.12.155.

# 7. List of figures

# 8. List of tables

# 9. List of abbreviations

| | |
|---|---|
| C | Capacitor |
| CE | Counter electrode |
| CPE | Constant phase element |
| CV | Cyclic voltammetry |
| DMC | Dimethyl carbonate |
| EDX | Energy-dispersive X-ray spectrometry |
| EEC | Equivalent electrical circuit |
| L | Inductor |
| LIB | Lithium-ion battery |
| $MoO_{2+x}$ | Molybdenum(IV)-oxide |
| NT | Nanotube |
| OCV | Open circuit voltage |
| PEIS | Potential dependant electrochemical impedance spectroscopy |
| PVD | Physical vapour deposition |
| Q | Constant phase element |
| R | Resistor |
| RE | Reference electrode |
| SEM | Scanning electron microscope |
| SIB | Sodium ion battery |
| SPEIS | Staircase potential dependent electrochemical impedance spectroscopy |
| $TiO_{2-x}$-A | Titanium(IV)-oxide anatase |
| $TiO_{2-x}$-R | Titanium(IV)-oxide rutile |
| $TiO_2$-M | Titanium(IV)-oxide amorphous |
| W | Warburg element |
| WE | Working electrode |
| XPS | X-ray photoelectron spectroscopy |
| XRD | X-ray diffraction |
| Z | Impedance |

# 10. Appendix

## 10.1. Annealing parameters of TiO$_{2-x}$-A

Table 7.: Annealing parameters of TiO$_{2-x}$-A samples

| Ti_05_A_EC and Ti_07_A_EC | | | | | | | |
|---|---|---|---|---|---|---|---|
| Time [min] | 90 | 20 | 20 | 33 | 300 | 60 | 460 |
| Gas flow Ar [sccm/min] | 600 | 200 | 200 | 200 | 200 | 200 | 200 |
| Temperature [°C] | 23 | 23-200 | 200-300 | 300-400 | 400 | 400-23 | 23 |
| Ti_08_A_EC and Ti_09_A_EC | | | | | | | |
| Time [min] | 90 | 20 | 20 | 33 | 300 | 60 | 460 |
| Gas flow Ar [sccm/min] | 600 | 200 | 200 | 200 | 200 | 200 | 200 |
| Temperature [°C] | 23 | 23-200 | 200-300 | 300-400 | 400 | 400-23 | 23 |

## 10.2. PVD parameters of MoO$_{2+x}$

Table 8.: PVD parameters for MoO$_{2+x}$ synthesis attempts

| Sample name | Ambient pressure $p_0$ | Oxygen pressure $p_{02}$ | Argon pressure $p_{Ar}$ | Temp. sample holder | Current Transformer | Power Magnetron | Sputtering time |
|---|---|---|---|---|---|---|---|
| | [mbar] | [mbar] | [mbar] | [°C] | [A] | [W] | [min] |
| Mo_04_05 | $3.6 \cdot 10^{-6}$ | $2.1 \cdot 10^{-3}$ | $1.19 \cdot 10^{-2}$ | 453 | 80 | 40 | 60 |
| Mo_06-08 | $2.37 \cdot 10^{-6}$ | $2.1 \cdot 10^{-3}$ | $1.23 \cdot 10^{-2}$ | 461 | 80 | 40 | 60 |
| Mo_09_10 | $7.05 \cdot 10^{-6}$ | $2.50 \cdot 10^{-3}$ | $1.50 \cdot 10^{-2}$ | 556 | 80 | 40 | 60 |
| Mo_11_12 | $2.10 \cdot 10^{-6}$ | $2.50 \cdot 10^{-3}$ | $1.57 \cdot 10^{-2}$ | 507 | 72 | 40 | 60 |
| Mo_13_14 | $2.56 \cdot 10^{-6}$ | $2.50 \cdot 10^{-3}$ | $1.55 \cdot 10^{-2}$ | 504 | 75 | 40 | 60 |

| | | | | | | | |
|---|---|---|---|---|---|---|---|
| Mo_15_16 | $3.26 \cdot 10^{-6}$ | $2.50 \cdot 10^{-3}$ | $1.50 \cdot 10^{-2}$ | 505 | 72 | 55 | 60 |
| Mo_17_18 | $3.56 \cdot 10^{-6}$ | $2.10 \cdot 10^{-3}$ | $1.05 \cdot 10^{-2}$ | 500 | 72 | 55 | 60 |
| Mo_19_20 | $2.69 \cdot 10^{-6}$ | $2.10 \cdot 10^{-3}$ | $1.57 \cdot 10^{-2}$ | 488 | 72 | 40 | 60 |
| Mo_21_22 | $1.9 \cdot 10^{-6}$ | $7.00 \cdot 10^{-4}$ | $0.63 \cdot 10^{-2}$ | 472 | 72 | 55 | 60 |
| Mo_23_24 | $2.8 \cdot 10^{-6}$ | $1.00 \cdot 10^{-4}$ | $1.02 \cdot 10^{-2}$ | 40 | ~10 | 40 | 60 |
| Mo_25_26 | $3.75 \cdot 10^{-6}$ | $1.00 \cdot 10^{-4}$ | $0.99 \cdot 10^{-2}$ | 38 | ~10 | 40 | 60 |
| Mo_27_28 | $2.6 \cdot 10^{-6}$ | $1.03 \cdot 10^{-4}$ | $1.04 \cdot 10^{-2}$ | 39 | ~10 | 40 | 60 |
| Mo_29_30 | $3.4 \cdot 10^{-6}$ | $1.01 \cdot 10^{-4}$ | $1.05 \cdot 10^{-2}$ | 35 | ~10 | 40 | 60 |

The first synthesis attempt was immediately successful. The XPS spectrum shows a mass fraction of about 72% (see Figure 53). Due to unknown reasons, the following synthesis attempts were not successful. Since the first attempt could not be reproduced, the temperature was increased from about 450 °C to about 550 °C, which made the sample looking burnt as seen in Figure 48 b). The temperature was decreased again and various $O_2$/Ar ratios from 1:5 to 1:7 were tested. Additionally, the Ar pressure was reduced from $1.57 \cdot 10^{-2}$ down to $1.05 \cdot 10^{-2}$. The result was always a slightly shining sample without a homogenous layer of $MoO_2$ as seen in Figure 48 c)-e). After an additional research in the literature the temperature finally was decreased to RT.[11] In addition to that, the $O_2$/Ar ratio was set to 1:100. Finally the samples had a flat, shiny, homogeneous surface (see Figure 48 f)) and the XPS data show that the following samples, which were prepared for the electrochemical characterisation, at least contain a mixture of $MoO_2$ and $MoO_3$ (Figure 53 b)-d)).
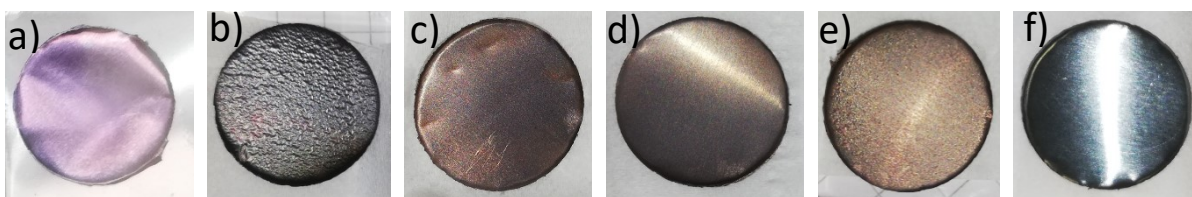


Figure 48.: Samples after PVD synthesis: a) Mo_05_PVD, b) Mo_10_PVD, c) Mo_11_PVD, d) Mo_13_PVD, e) Mo_21_PVD, f) Mo_29_PVD

## 10.3. Synthesis of TiO$_{2-x}$-R

The synthesis of TiO$_{2-x}$-R was successful after a certain number of attempts, which took some time. Thus, no test cells for the electrochemical characterisation were built with TiO$_{2-x}$-R electrodes for reasons of time. However, the synthesis was finally successful, and therefore the optimized parameters and the procedure are described in this chapter.

To check if the synthesis was successful, Raman spectroscopy was performed after every attempt, which can be seen in chapter 10.4. The first few samples were annealed with the "TiO$_{2-x}$-R first try" parameters given in Table 9.

Table 9.: Annealing parameters of several TiO$_{2-x}$-R attempts

| TiO$_{2-x}$-R first try | | | | | | | |
|---|---|---|---|---|---|---|---|
| Time [min] | 90 | 20 | 20 | 133 | 300 | 60 | 460 |
| Gasflow Ar [sccm/min] | 600 | 200 | 200 | 200 | 200 | 200 | 200 |
| Temperature [°C] | 23 | 23-200 | 200-300 | 300-700 | 700 | 700-23 | 23 |
| TiO$_{2-x}$-R second last try | | | | | | | |
| Time [min] | 90 | - | 251 | - | 500 | 90 | 400 |
| Gasflow Ar [sccm/min] | 600 | - | 200 | - | 200 | 200 | 200 |
| Temperature [°C] | 23 | - | 23-650 | - | 650 | 650-23 | 23 |
| TiO$_{2-x}$-R last try | | | | | | | |
| Time [min] | 90 | - | 251 | - | 1440 | 90 | 400 |
| Gasflow Ar [sccm/min] | 600 | - | 200 | - | 200 | 200 | 200 |
| Temperature [°C] | 23 | - | 23-650 | - | 650 | 650-23 | 23 |

The main problem of the first few attempts was the occurring unknown phase shown in Figure 50 a). After rethinking the problem, two improvements to get a pure rutile phase sample were carried out. On the one hand, the temperature was decreased from 700 °C to 650 °C, and on the other hand, holding time was increased from 300 minutes to 500 minutes as given in Table 9 ("TiO$_{2-x}$-R second last try"). The result was a phase mixture of TiO$_{2-x}$-A and TiO$_{2-x}$-R, which can be detected by a sickle-shaped discoloration at the edge in Figure 49. Also, the Raman spectra shown in Figure 50 b) indicate a phase mixture.

The last improvement, which finally led to success, was the increase of the holding time from 50 minutes to 1440 minutes ("TiO$_{2-x}$-R last try" in Table 9). The picture of the sample and the Raman spectra depicted in Figure 51 a) and b) show that the phase transition was finally successful.

## 10.4. Raman Spectroscopy of TiO$_{2-x}$-R

Table 10.: Raman shifts of the Ti$^{18}$O$_2$, Ti$^{17}$O$_2$ and Ti$^{16}$O$_2$ rutile at 295 K.

| Mode/cm$^{-1}$ | Ti$^{16}$O$_2$ | Ti$^{17}$O$_2$ | Ti$^{18}$O$_2$ | Reference |
|---|---|---|---|---|
| B$_{1g}$ | 145 | 139 | 138 | [64] |
| E$_g$ | 448 | 434 | 426 | [64] |
| A$_{1g}$ | 613 | 592 | 579 | [64] |
| B$_{2g}$ | 826 | 804 | 788 | [64] |



Figure 49.: Measurement points of TiO$_{2-x}$-R

The correct Raman peak positions of the TiO$_{2-x}$-R are given in Table 10.

Figure 50 a) shows the Raman spectra of the first attempt. The intensities of the two spectra of about 600 and 700 is low compared to the intensities of the last try with values between 2500 and 15000. Also, the B$_{1g}$ peak at 152 cm$^{-1}$, the E$_g$ peak at 432 cm$^{-1}$ and the A$_{1g}$ peak at 613 cm$^{-1}$ cannot be located in the spectra. That suggests that no TiO$_{2-x}$-R is present.
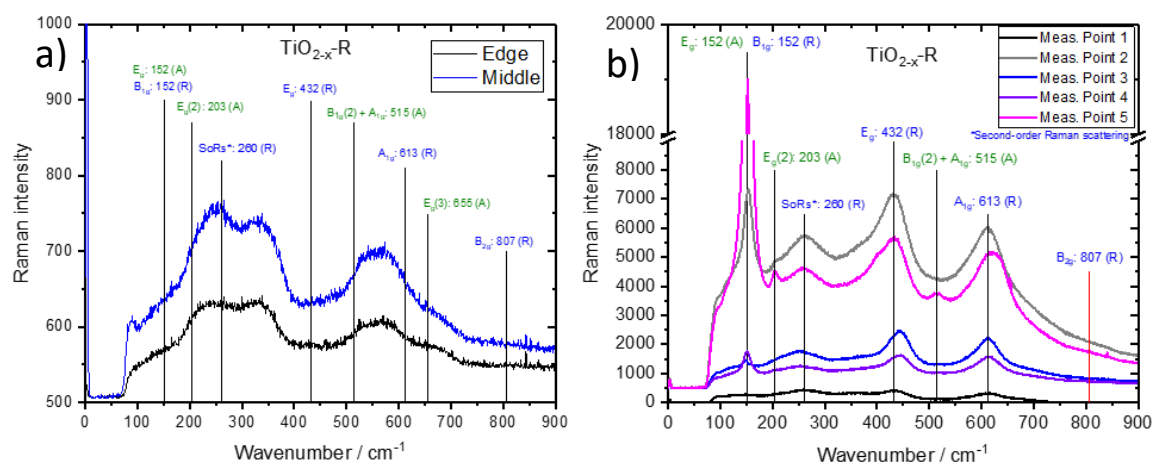


Figure 50.: Raman spectra of annealed TiO$_{2-x}$-R a) an early try with an unknown phase composition and b) with a mixture of TiO$_{2-x}$-A and TiO$_{2-x}$-R

The Raman spectra of the second last try (Figure 50 b)) show distinct peaks at the correct peak positions for the rutile phase except of the $B_{2g}$ at 807 cm$^{-1}$. Additionally, the measurement point 5 shows anatase peaks at 203 cm$^{-1}$ and 515 cm$^{-1}$, which indicates the presence of TiO$_{2-x}$-A. Also the peak at 152 cm$^{-1}$ indicated a phase mixture because it should be more a broad, short peak and not a sharp, high one. [90,95]
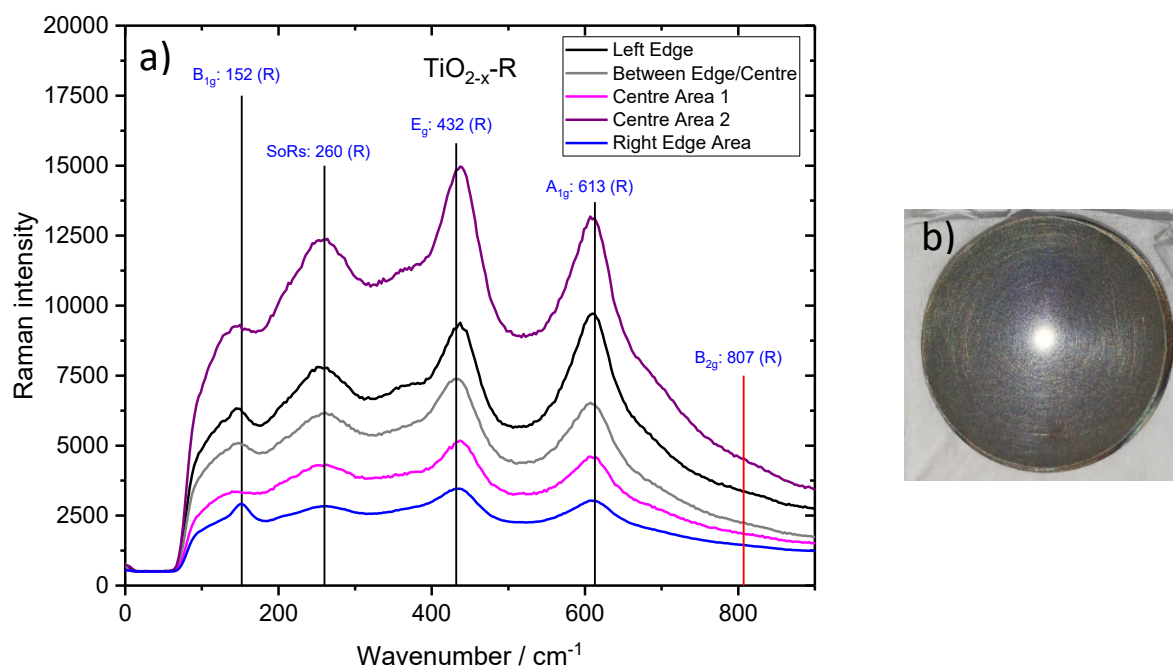


Figure 51.: a) Raman spectra of the successful annealed TiO$_{2-x}$-R and b) picture of the successful annealed TiO$_{2-x}$-R disc

The Raman spectra of the last try (Figure 51 a)) finally show distinct peaks only at the correct peak positions for the rutile phase.

## 10.5.  XRD

As mentioned in chapter 10.4, several rutile annealing attempts were made. To check whether the synthesis really does not work, additional XRD measurements were performed.

Table 11 shows all theoretical reflections of $TiO_{2-x}$-A, $TiO_{2-x}$-R and pure titanium, respectively.

Table 11.: XRD reflections of $TiO_{2-x}$-A, $TiO_{2-x}$-R and pure titanium metal

| $TiO_{2-x}$-A | | | $TiO_{2-x}$-R | | | Ti |
|---|---|---|---|---|---|---|
| Ref[96] | Ref[97] | Ref[98] | Ref[96] | Ref[97] | Ref[98] | Ref[98] |
| $2\theta$ / ° | $2\theta$ / ° | $2\theta$ / ° | $2\theta$ / ° | $2\theta$ / ° | $2\theta$ / ° | $2\theta$ / ° |
| 25.5 | 26 | - | 27.5 | 27.5 | 27.5 | 35.25 |
| 37.5 | 37.5 | - | 36.5 | 35.5 | 36.25 | 38.75 |
| 38 | - | 38 | 39 | 39 | 39.25 | 40.5 |
| 38.5 | 38.5 | - | 42 | 41 | 41.25 | 53.25 |
| 48 | 47.5 | - | 44 | 43.5 | 44 | 63.25 |
| 54 | 52, 54 | 52.5 | 54.5 | 54 | 54.5 | 71 |
| 56 | 61 | - | - | 57, 63, 64 | 56.5, 62.5, 64 | 76.5 |

In Figure 52, the XRD spectra of three presumed rutile samples are shown. The lower green, red and olive reflections represent the correct positions for the anatase [19], rutile [21] and the titanium phase [99], respectively.
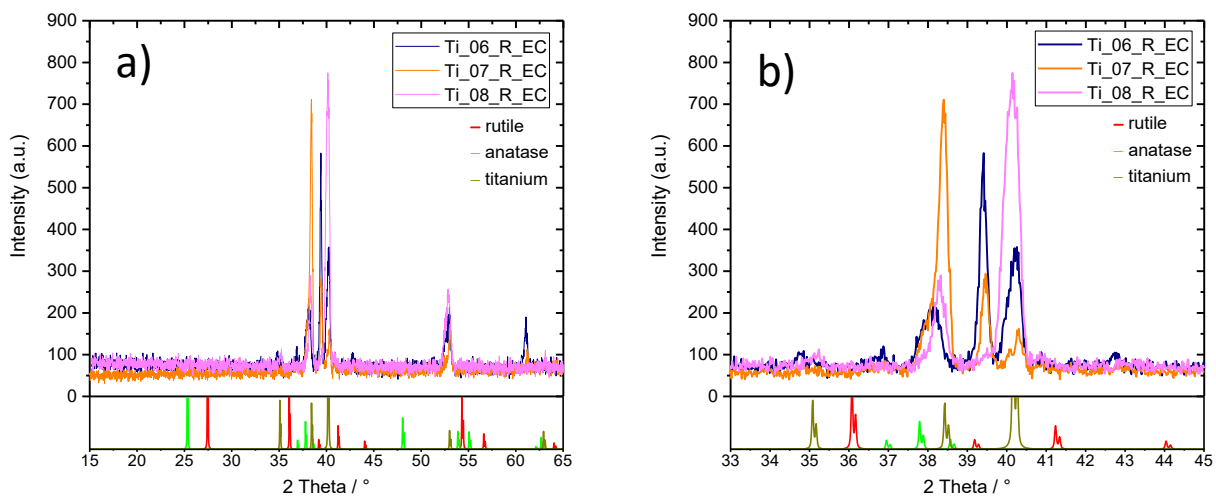


Figure 52.: XRD spectra of a) rutile samples and b) detail of the spectra from a),[19],[21], [99]

First of all, the missing peak between 25 and 30 degree for both phases, anatase and rutile, suggests that the phase transition did not occur to full extent. Also, the peak between 50 and 55 degree should be a degree or two higher to belong to the rutile spectra. The zoomed image b) additionally shows that the peaks at 35, 38.5 and 40 degree fits the titanium spectra and not the rutile one. The peaks at 39 degrees could belong to a carbon compound, but it is difficult to assign them.

## 10.6. Active Surface Area/Mass

$$I(t) = C \cdot \frac{dV(t)}{dt} \tag{9.1.1}$$

$$C = \frac{xxx \times 10^{-5} \, [A]}{xxx \times 10^{-5} \, [V \, s^{-1}]} = xx \, \frac{[As]}{[V]} \; or \; xx[F] \tag{9.1.2}$$

$$A = \frac{0.21[F]}{15 \times 10^{-6}[F \, cm^{-2}]} = 14000 \; cm^2 \tag{9.1.3}$$

## 10.7. XPS

Table 12.: XPS values for $TiO_{2-x}$-R

| TiO₂ Rutile | Ti 2p₃/₂ | FWHM | Ti 2p₁/₂ | FWHM | Reference |
|---|---|---|---|---|---|
| | [eV] | [eV] | [eV] | [eV] | |
| Ti(IV)-oxide | 458.46 ± 0.09 | 1.04 | + 5.77 | 2.01 | [66] |
| Ti(III)-oxide | 457.30 ± 0.70 | | +5.20 | | [67] |
| Ti(II)-oxide | 455.50 ± 0.60 | | +5.60 | | [67] |
| Ti(0) | 453.74 ± 0.02 | 0.69 | +6.05 | 0.83 | [66] |
| O1s Lattice | 529.70 ± 0.10 | 1.03 | | | [66] |
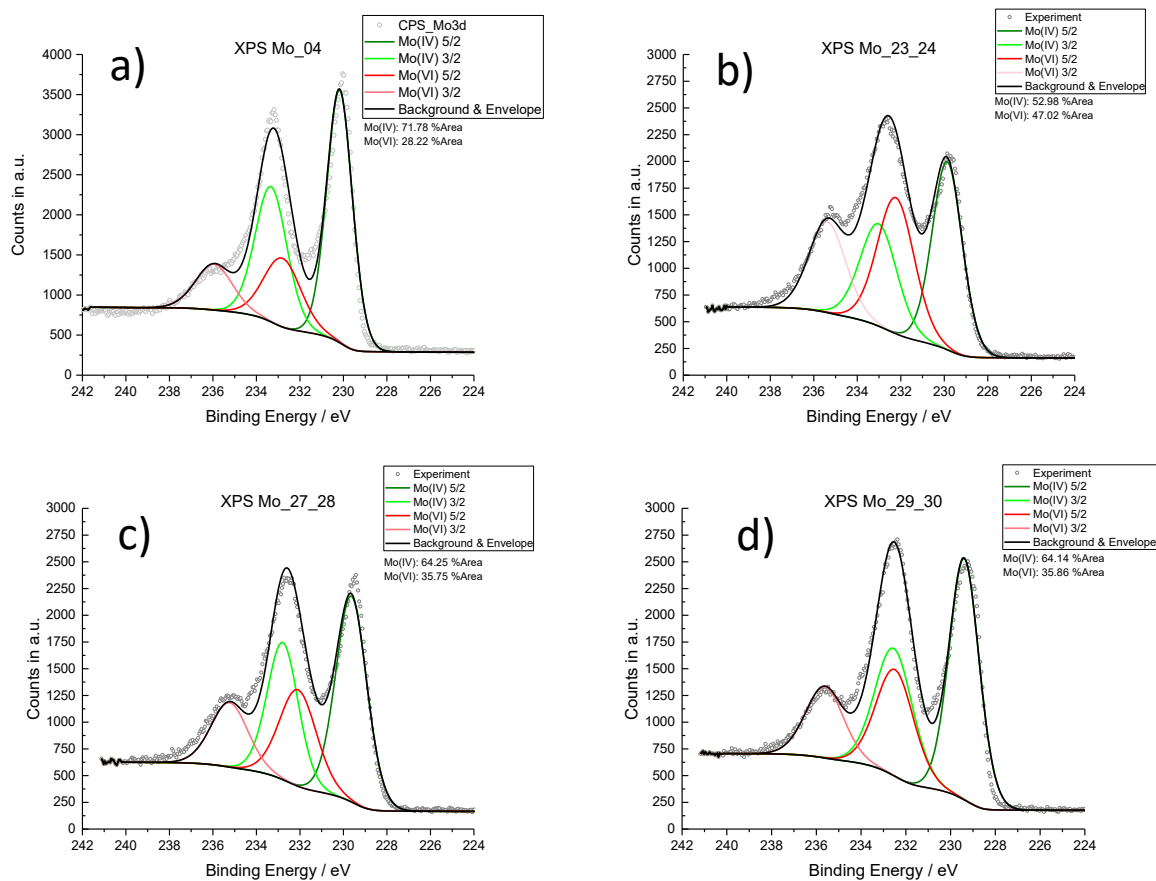


Figure 53.: XPS spectra of all successfully prepared $MoO_{2+x}$ samples
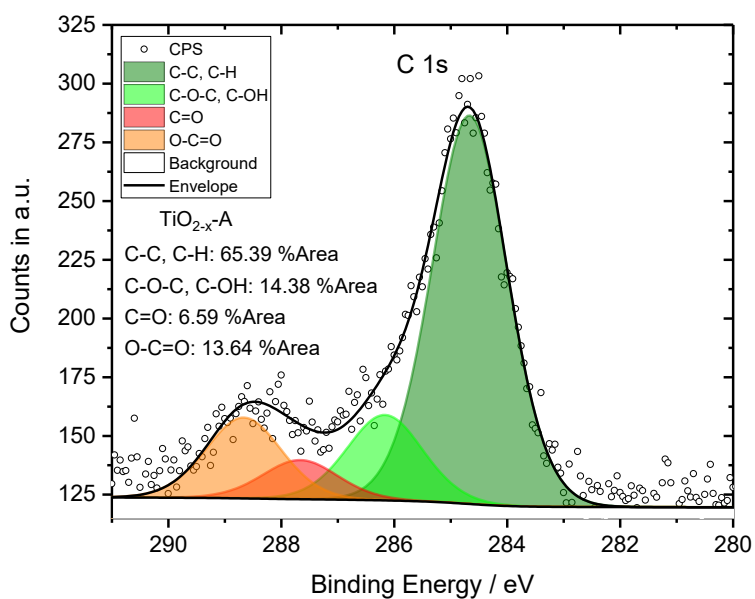
Figure 54.: C 1s spectra of TiO$_{2-x}$-A before electrochemical characterisation including relative mass distribution.
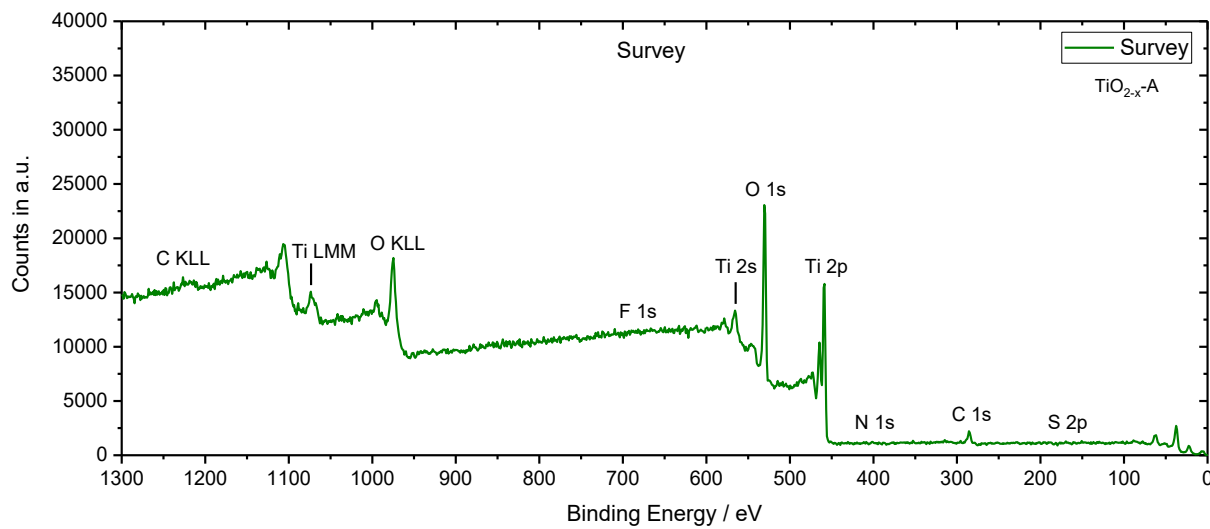


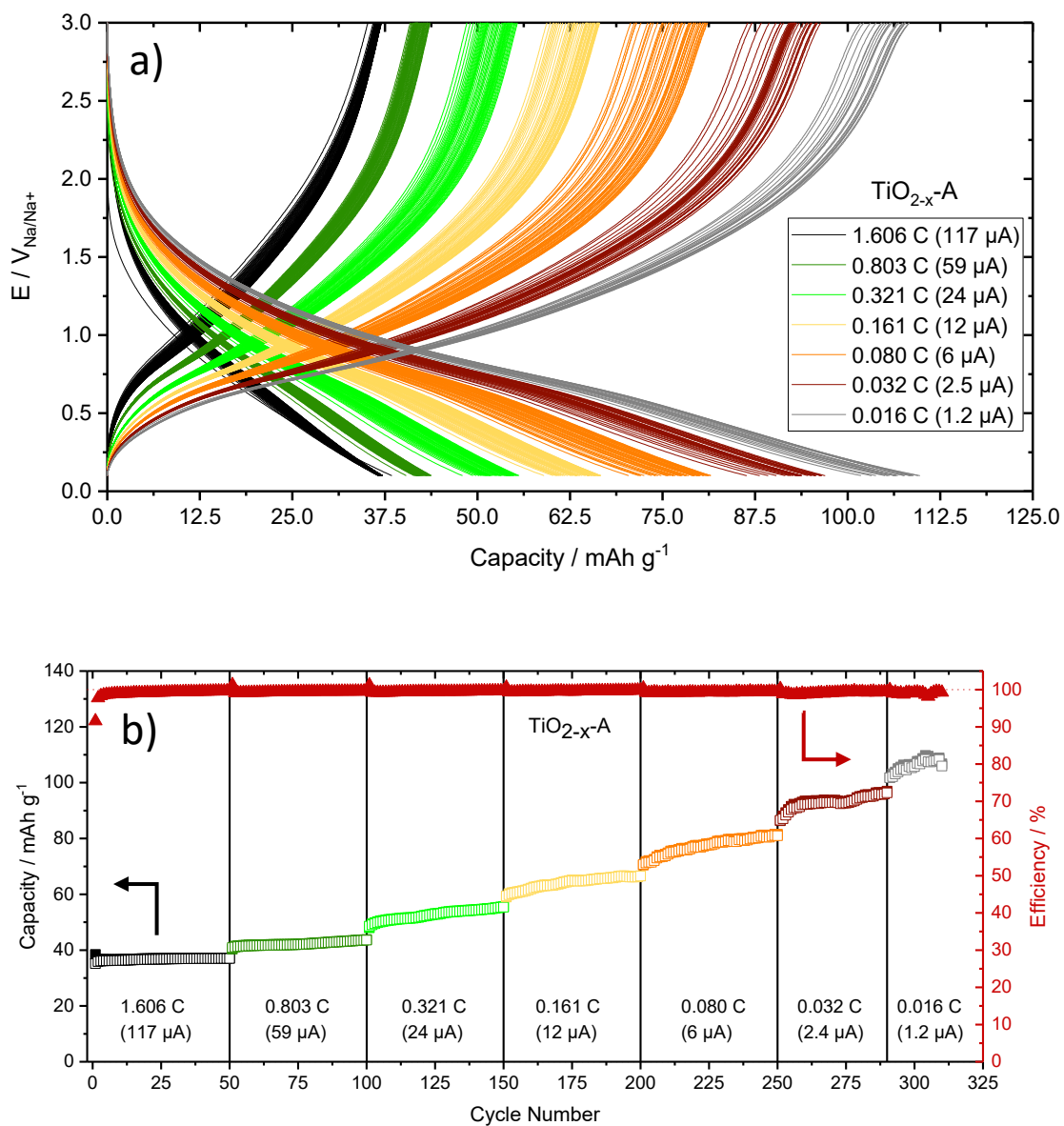Figure 55.: Survey spectra of TiO$_{2-x}$-A sample before electrochemical characterisation.

## 10.8.  GCPL of TiO$_{2-x}$-A and MoO$_{2+x}$



Figure 56.: a) The voltage with respect to the specific capacity of TiO$_{2-x}$-A normalized to the mass, and b) the specific capacity with respect to the cycle number and corresponding Coulombic efficiencies (red triangles) of TiO$_{2-x}$-A normalized to the mass. Closed squares relate to discharge (sodiation) and open squares to charge (desodiation) capacities.
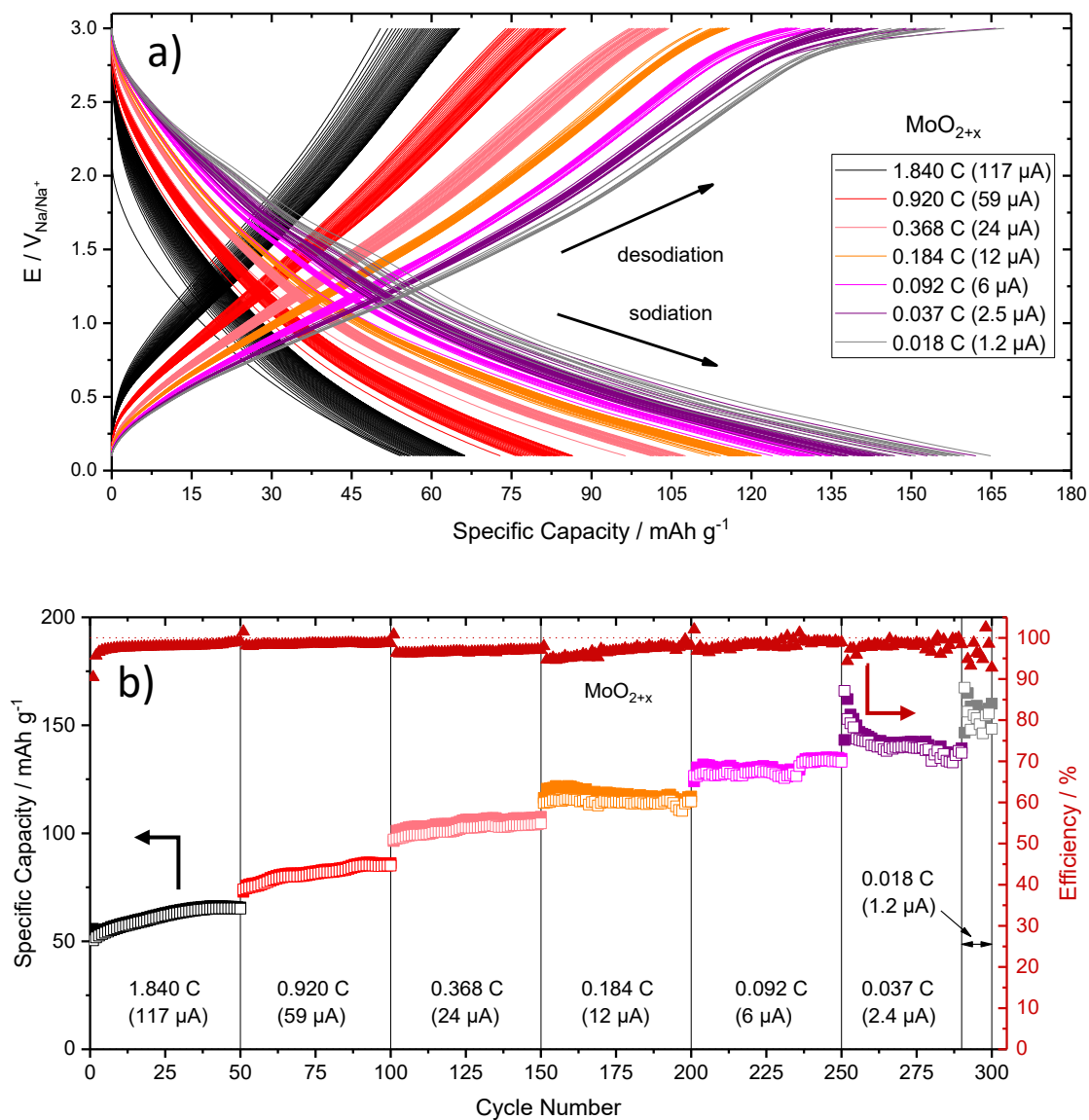
Figure 57.: a) The voltage with respect to the specific capacity of $MoO_{2+x}$ normalized to the mass, and b) the specific capacity with respect to the cycle number and corresponding Coulombic efficiencies (red triangles) of $MoO_{2+x}$ normalized to the mass. Closed squares relate to discharge (sodiation) and open squares to charge (desodiation) capacities.
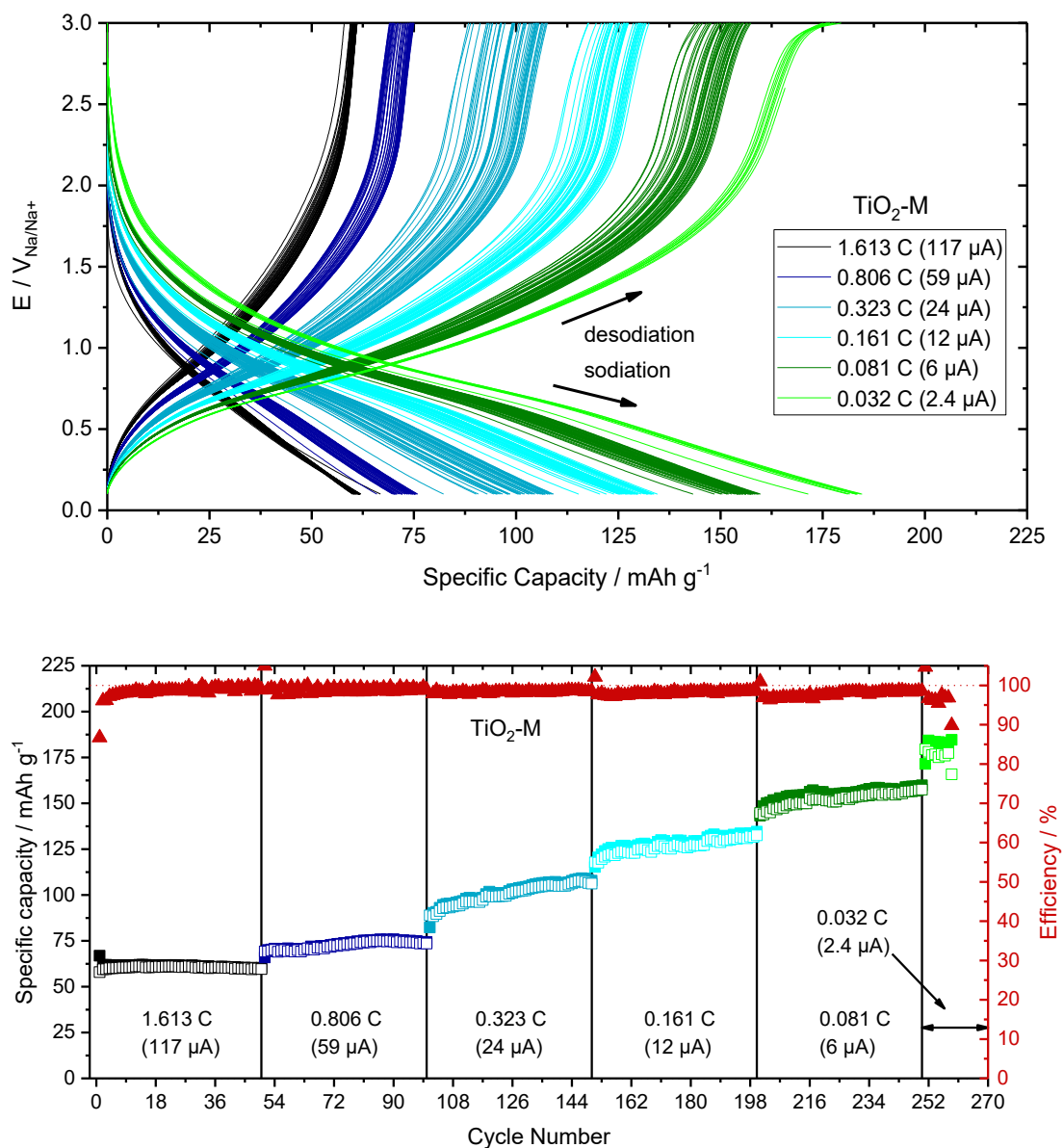
Figure 58.: a) The voltage with respect to the specific capacity of TiO2-M normalized to the mass, and b) the specific capacity with respect to the cycle number and corresponding Coulombic efficiencies (red triangles) of MoO2+x normalized to the mass. Closed squares relate to discharge (sodiation) and open squares to charge (desodiation) capacities.
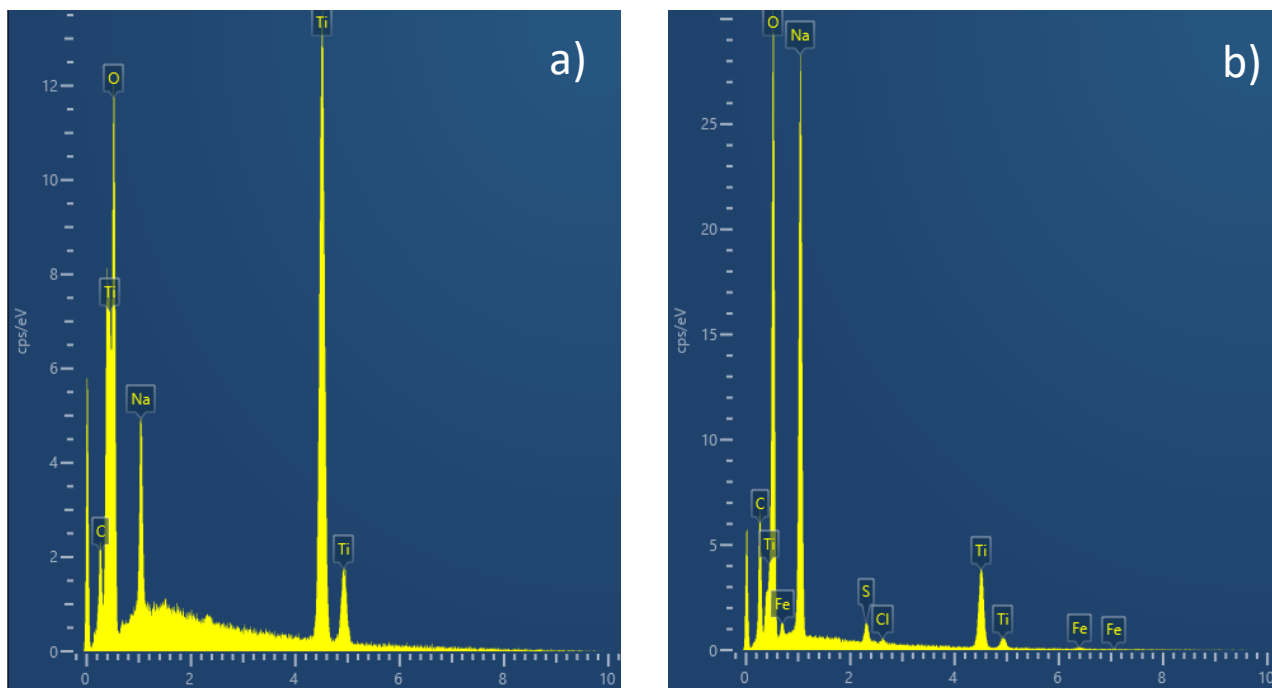
## 10.9. Post mortem EDX of TiO$_{2-x}$-A and MoO$_{2+x}$
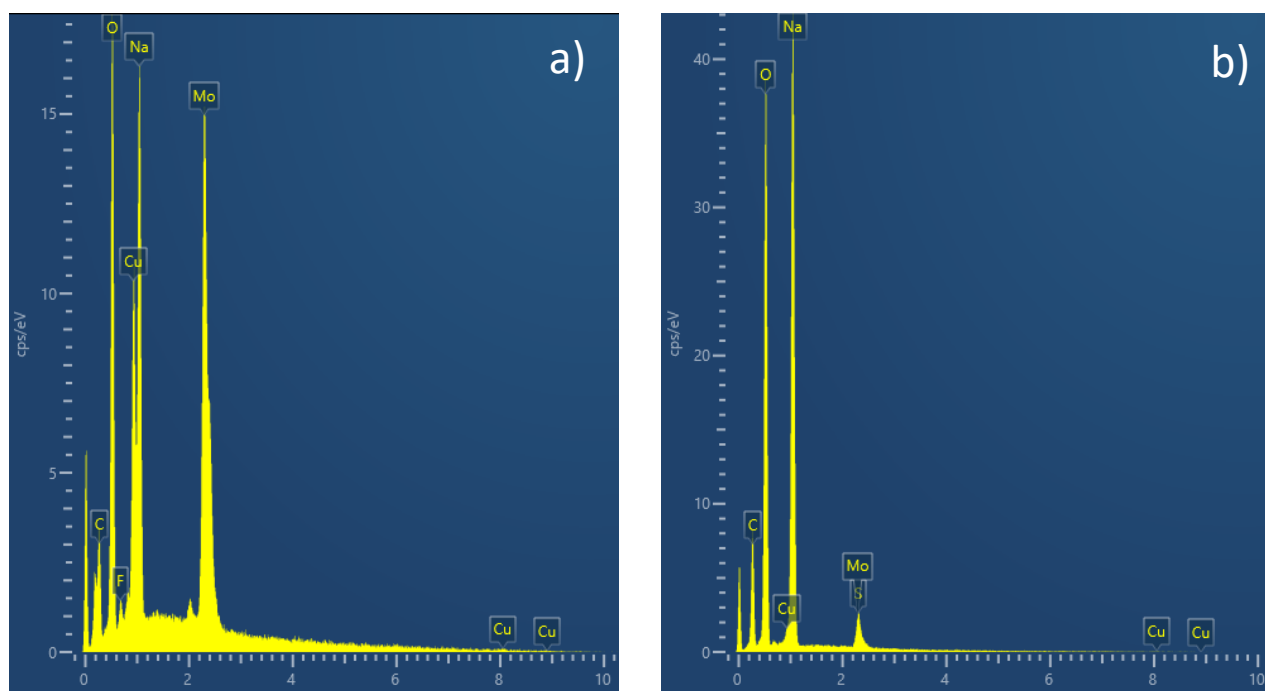


Figure 59.: EDX spectra of TiO$_{2-x}$-A



Figure 60.: EDX spectra of MoO$_{2+x}$